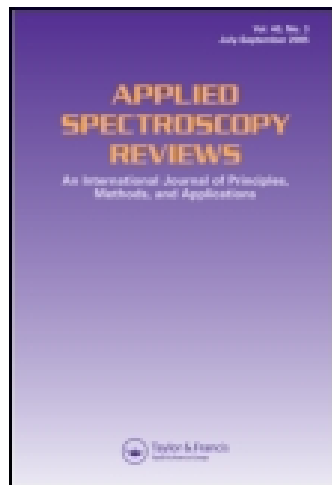


This article was downloaded by: [Purdue University]

On: 24 February 2015, At: 06:44

Publisher: Taylor & Francis

Informa Ltd Registered in England and Wales Registered Number: 1072954 Registered office: Mortimer House, 37-41 Mortimer Street, London W1T 3JH, UK



## Applied Spectroscopy Reviews

Publication details, including instructions for authors and subscription information:

<http://www.tandfonline.com/loi/laps20>

## Raman Spectroscopy of Biological Tissues

Abdullah Chandra Sekhar Talari<sup>a</sup>, Zanyar Movasaghi<sup>b</sup>, Shazza Rehman<sup>c</sup> & Ihtesham ur Rehman<sup>a</sup>

<sup>a</sup> Department of Materials Sciences and Engineering, The Kroto Research Institute, University of Sheffield, Sheffield, UK

<sup>b</sup> Barts Health NHS Trust, Community Health Services Division, St. Leonard's Hospital, London, UK

<sup>c</sup> Department of Medical Oncology, Airedale NHS Foundation Trust, Airedale General Hospital, West Yorkshire, UK

Accepted author version posted online: 29 May 2014. Published online: 14 Aug 2014.



[Click for updates](#)

To cite this article: Abdullah Chandra Sekhar Talari, Zanyar Movasaghi, Shazza Rehman & Ihtesham ur Rehman (2015) Raman Spectroscopy of Biological Tissues, Applied Spectroscopy Reviews, 50:1, 46-111, DOI: [10.1080/05704928.2014.923902](https://doi.org/10.1080/05704928.2014.923902)

To link to this article: <http://dx.doi.org/10.1080/05704928.2014.923902>

PLEASE SCROLL DOWN FOR ARTICLE

Taylor & Francis makes every effort to ensure the accuracy of all the information (the "Content") contained in the publications on our platform. However, Taylor & Francis, our agents, and our licensors make no representations or warranties whatsoever as to the accuracy, completeness, or suitability for any purpose of the Content. Any opinions and views expressed in this publication are the opinions and views of the authors, and are not the views of or endorsed by Taylor & Francis. The accuracy of the Content should not be relied upon and should be independently verified with primary sources of information. Taylor and Francis shall not be liable for any losses, actions, claims, proceedings, demands, costs, expenses, damages, and other liabilities whatsoever or howsoever caused arising directly or indirectly in connection with, in relation to or arising out of the use of the Content.

This article may be used for research, teaching, and private study purposes. Any substantial or systematic reproduction, redistribution, reselling, loan, sub-licensing, systematic supply, or distribution in any form to anyone is expressly forbidden. Terms &

Conditions of access and use can be found at <http://www.tandfonline.com/page/terms-and-conditions>

# Raman Spectroscopy of Biological Tissues

ABDULLAH CHANDRA SEKHAR TALARI,<sup>1</sup> ZANYAR  
MOVASAGHI,<sup>2</sup> SHAZZA REHMAN,<sup>3</sup>  
AND IHTESHAM UR REHMAN<sup>1</sup>

<sup>1</sup>Department of Materials Sciences and Engineering, The Kroto Research  
Institute, University of Sheffield, Sheffield, UK

<sup>2</sup>Barts Health NHS Trust, Community Health Services Division, St. Leonard's  
Hospital, London, UK

<sup>3</sup>Department of Medical Oncology, Airedale NHS Foundation Trust, Airedale  
General Hospital, West Yorkshire, UK

**Abstract:** *We previously published a comprehensive review paper reviewing the Raman spectroscopy of biological molecules. This research area has expanded rapidly, which warranted an update to the existing review paper by adding the recently reported studies in literature. This article reviews some of the recent advances of Raman spectroscopy in relation to biomedical applications starting from natural tissues to cancer biology. Raman spectroscopy, an optical molecular detective, is a vibrational spectroscopic technique that has potential not only in cancer diagnosis but also in understanding progression of the disease. This article summarizes some of the most widely observed peak frequencies and their assignments. The aim of this review is to develop a database of molecular fingerprints, which will facilitate researchers in identifying the chemical structure of the biological tissues including most of the significant peaks reported both in the normal and cancerous tissues. It has covered a variety of Raman approaches and its quantitative and qualitative biochemical information. In addition, it covers the use of Raman spectroscopy to analyse a variety of different malignancies including breast, brain, cervical, gastrointestinal, lung, oral, and skin cancer. Multivariate analysis approaches used in these studies have also been covered.*

**Keywords:** Raman spectroscopy, biological tissues, analysis of cancer tissues, characteristic peak assignments

## Aims

For the purpose of noninvasive diagnostic applications, vibrational spectroscopic techniques are becoming potential tools. Applications of spectroscopic techniques in biological studies have increased significantly in recent years; in particular, clinical investigations regarding detection of cancer and malignancy have gained attention from both clinical and nonclinical researchers. Numerous papers have been published on the diagnostic significance of different spectroscopic and imaging techniques in the field of cancer detection (1–12). However,

Address correspondence to Ihtesham ur Rehman, Department of Materials Sciences and Engineering, The Kroto Research Institute, University of Sheffield, North Campus, Broad Lane, Sheffield S3 7HQ, UK. E-mail: i.u.rehman@sheffield.ac.uk

there has been a gap in the details of the characteristic peak frequencies and their definitions. This can be attributed to the fact that specific functional groups present in the biological tissues have not yet been fully investigated. In addition, there is no comprehensive review in the literature that addresses the Raman spectroscopic investigations of all biological tissues together, as researchers have to rely on a number of previously published research papers and most of the time the interpretation of the spectral data differs considerably. In this article, a considerable number of spectroscopic investigations published on biological tissues are reviewed and it shows that there are striking similarities in defining different peak frequencies (13). Furthermore, by compiling a unique database involving a detailed study on the works, different chemical bands and their assignments of spectral bands could provide significant assistance to research groups focusing on spectroscopy, which in turn can lead to significant improvements in the quality and quantity of research done. This article has updated recent Raman spectroscopic investigations of biological tissues; most of them explored multivariate approaches, especially in distinguishing cancerous tissues from normal tissues (14, 15).

This article endeavors to present a broad and detailed collection of interpretation of Raman spectral frequencies. It is predicted that this article will be of considerable assistance to research groups working on Raman spectroscopy of biological tissues. Moreover, it presents current researchers with an overall view of Raman spectroscopic findings in cancer biology, especially in detection and understanding of the disease at the molecular level.

## Introduction

Spectroscopy has emerged lately as one of the main tools for biomedical applications and has made considerable progress in the field of clinical assessment. Research has been performed on a wide variety of natural tissues using spectroscopic techniques, including Raman spectroscopy. These vibrational spectroscopic techniques are comparatively straightforward, reproducible, and noninvasive to the tissue and only small amounts of material (micrograms to nanograms) with minimum sample preparation are required. In addition, these techniques provide molecular-level information allowing investigation of functional groups, bonding types, and molecular conformations. In vibrational spectra, the spectral bands are molecule specific and provide unique information about the biochemical composition. These bands are fairly narrow, easy to resolve, and sensitive to molecular structure, conformation, and environment.

In studies related to spectroscopic techniques it is strongly believed that both the reliable experimental procedure and characterization of spectral peak positions and their assignment along with accurate peak detection and definition are of crucial importance. Although a number of scientists have used different techniques, it seems that there is a noticeable similarity in their spectral interpretations of comparable areas in their collected spectra.

In Table 1, the spectral interpretation studies that have been published so far are tabulated. This table provides a comprehensive account of spectral frequencies of the biological tissues.

## Raman Spectroscopy

Raman spectroscopy, a molecular and chemical detective, can be used to optically probe the molecular changes associated with diseased tissues (16, 17). Theoretically, when the energy of an incident photon is unaltered after collision with a molecule, the scattered

**Table 1**  
Spectral interpretations

Peak (cm <sup>-1</sup> )	Assignment	Reference
415	Phosphatidylinositol	71
418	Cholesterol	71
428	Symmetric stretching vibration of $\nu_2$ PO <sub>4</sub> <sup>3-</sup> (phosphate of HA)	50
429	Cholesterol, cholesterol ester	71
445	N-C-S stretch (one of three thiocyanate peaks, with 2095 and 735 cm <sup>-1</sup> )	104
447, 454	Ring torsion of phenyl (2)	121
477	Polysaccharides (amylase, amylopectin)	64
481	DNA	110
484–490	Glycogen	31
490	Glycogen	30
505, 508	C–OH <sub>3</sub> torsion of methoxy group(1)	121
509	S-S disulfide stretching band of collagen	50
	$\nu$ (S-S) <i>gauche-gauche-gauche</i> (amino acid cysteine)	64
519	Phosphatidylinositol	70
524	S-S disulfide stretching in proteins	30, 31
	Phosphatidylserine	71
535	Cholesterol ester	28
	$\nu$ (S-S) <i>gauche-gauche-trans</i> (amino acid cysteine)	64
538	Cholesterol ester	71
540	$\nu$ (S-S) <i>trans-gauche-trans</i> (amino acid cysteine)	64
548	Cholesterol	71
540	Glucose-saccharide band (overlaps with acyl band)	71
573	Tryptophan/cytosine, guanine	31
576	Phosphatidylinositol	71
583, 586	OH out-of-plane bending (free)	121
589	Symmetric stretching vibration of $\nu_4$ PO <sub>4</sub> <sup>3-</sup> (phosphate of HA)	50
	Glycerol	71
596	Phosphatidylinositol	71
600–800	Nucleotide conformation	103
607	Glycerol	71
608	Cholesterol	71
614	Cholesterol ester	71
618	C–C twisting (protein)	103
620	C–C twist aromatic ring (one of C–C vibrations to be expected in aromatic structure of xylene)	111
621	C–C twisting mode of phenylalanine (proteins)	30, 31, 122
630	Glycerol	71
630–670	$\nu$ (C-S) <i>gauche</i> (amino acid methionine)	64
639	Tyrosine ring breathing	39
640	C-S stretching and C–C twisting of proteins; tyrosine	103
643	C–C twisting mode of tyrosine	31, 50

(Continued on next page)

**Table 1**  
Spectral interpretations (*Continued*)

Peak (cm <sup>-1</sup> )	Assignment	Reference
645	C—C twisting mode of phenylalanine (proteins)	122
646	C—C twisting mode of tyrosine	50
662	C-S stretching mode of cystine (collagen type I)	30, 50
666	G, T (ring breathing modes in the DNA bases); tyrosine-G backbone in RNA	103
667–669	C-S stretching mode of cystine (collagen type I) T, G (DNA/RNA)	30, 50 122
669	C-S stretching mode of cytosine	31
669	$\nu_7(\delta)$ : porphyrin deformation), observed in the spectra of single human RBC	98
671	Ring breathing of tryptophan	39
678	Ring breathing modes in the DNA bases G (ring breathing modes in the DNA bases)/C-2'-endo-anti	103
700–745	$\nu(\text{C-S})$ <i>trans</i> (amino acid methionine)	64
702	Cholesterol, cholesterol ester	71
717–719	C—N (membrane phospholipids head)/adenine CN <sup>+</sup> (CH <sub>3</sub> ) <sub>3</sub> (lipids)	31 122
718	Choline group	71
719	C—N (membrane phospholipid head)/nucleotide peak Symmetric stretch vibration of choline group N <sup>+</sup> (CH <sub>3</sub> ) <sub>3</sub> , characteristic for phospholipids Phosphatidylcholine, sphingomyelin C—C—N+ symmetric stretching in phosphatidylcholine (lipid assignment)	30 71 122
720–722	DNA	110
724	Nucleic acids	59
725	A (ring breathing mode of DNA/RNA bases)	103
726	C-S (protein), CH <sub>2</sub> rocking, adenine	31
727–728	C—C stretching, proline (collagen assignment) Lipid	123 141
728	Ring breathing of tryptophan	39
729	A	122
733	Phosphatidylserine	71
735	C-S stretch (one of three thiocyanate peaks, with 2095 and 445 cm <sup>-1</sup> )	104
742	DNA, tryptophan	38
746	T (ring breathing mode of DNA/RNA bases)	103
748	DNA	110
749	Symmetric breathing of tryptophan (protein assignment)	20, 30, 50
750	CH <sub>2,6</sub> out-of-plane bending, observed in the spectra of single human RBC Lactic acid	121 110

(Continued on next page)

**Table 1**  
Spectral interpretations (*Continued*)

Peak (cm <sup>-1</sup> )	Assignment	Reference
752	$\nu_{15}$ (porphyrin breathing mode), (the most informative about the status of RBC and a direct measure of the heme groups of the hemoglobins)	98
	DNA	110
752–755	Symmetric breathing of tryptophan (protein assignment)	20, 30, 50
755–756	Symmetric breathing of tryptophan	31, 67
759	Tryptophan	31
	Ethanolamine group	71
	Phosphatidylethanolamine	71
760	Tryptophan, $\delta$ (ring)	64
	Ring breathing tryptophan (proteins)	122
766	Pyrimidine ring breathing mode	69
776	Phosphatidylinositol	71
780	Uracil-based ring breathing mode	69
781	Cytosine/uracil ring breathing (nucleotide)	31, 30
782	DNA	110, 122
	Thymine, cytosine, uracil	122
	RNA	122
	U, T, C (ring breathing modes in the DNA/RNA bases)	122
784–745	Phosphodiester; cytosine	106
785	U, T, C (ring breathing modes in the DNA/RNA bases)	103
	Backbone O–P–O	
786	DNA: O–P–O, cytosine, uracil, thymine	31
	Pyrimidine ring breathing mode	69
787	Can be taken as a measure for the relative quantity of nucleic acids present	102
	Phosphatidylserine	71
788	C <sub>5</sub> '–O–P–O–C <sub>3</sub> ' phosphodiester bands in DNA	122
	DNA	122
	O–P–O stretching DNA	37
791	Pyrimidine	37
800–1200	Backbone geometry and phosphate ion interactions	103
802	Uracil-based ring breathing mode	69
810	Phosphodiester (Z-marker)	106
811	O–P–O stretching RNA	122
812	Phosphodiester (Z-marker)	106
813	One of the two most distinct peaks for RNA (with 1240 cm <sup>-1</sup> )	103
813	C–C stretching (collagen assignment)	123
	C <sub>5</sub> '–O–P–O–C <sub>3</sub> ' phosphodiester bands in RNA	122
	RNA	122
815	Proline, hydroxyproline, tyrosine, $\nu_2$ PO <sub>2</sub> <sup>-</sup> stretch of nucleic acids	50
816	d (CCH) aliphatic of collagen	28

(Continued on next page)

**Table 1**  
Spectral interpretations (*Continued*)

Peak (cm <sup>-1</sup> )	Assignment	Reference
817	C—C stretching (collagen assignment)	123
820	Protein band	2, 3
	Structural protein modes of tumors	27
820	Proteins, including collagen I	110
820–930	C—C stretch of proline and hydroxyproline	42
822	Phosphodiester	106
823	Out-of-plane ring breathing, tyrosine (protein assignment)	20
823–826	Phosphodiester	106
826	O—P—O stretch DNA	31
827	Proline, hydroxyproline, tyrosine, $\nu_2$ PO <sub>2</sub> <sup>-</sup> stretch of nucleic acids	50
828	Out-of-plane ring breathing, tyrosine/O—P—O stretch DNA	30, 31
	Phosphodiester	106
	O—P—O stretching DNA/RNA	122
	Ring breathing tyrosine	122
830	Proline, hydroxyproline, tyrosine, $\nu_2$ PO <sub>2</sub> <sup>-</sup> stretch of nucleic acids	50
	C—H out-of-plane bending in benzoid ring	124
830	Tyrosine (Fermi resonance of ring fundamental and overtone)	64
831	Asymmetric O—P—O stretching, tyrosine	103
838	Deformative vibrations of amine groups	124
840	$\alpha$ -Anomers	71
	Glucose–saccharide band (overlaps with acyl band)	71
	Saccharide ( $\alpha$ )	71
840–860	Polysaccharide structure	53
842	Glucose	31
847	Monosaccharides ( $\alpha$ -glucose), (C—O—C) skeletal mode	64
	Disaccharide (maltose), (C—O—C) skeletal mode	64
850	Most probably due to single-bond stretching vibrations for the amino acids and valine and polysaccharides	53
	Tyrosine (Fermi resonance of ring fundamental and overtone)	64
850–950	Signal-free area of amphetamine	125
852	Proline, hydroxyproline, tyrosine	50
	Tyrosine ring breathing	103
	Glycogen	110
853	Ring breathing mode of tyrosine and C—C stretch of proline ring	30, 31
	Glycogen	110
854	(C—O—C) skeletal mode of $\alpha$ -anomers (polysaccharides, pectin)	64
	Ring breathing tyrosine (proteins)	122

(Continued on next page)

**Table 1**  
Spectral interpretations (*Continued*)

Peak (cm <sup>-1</sup> )	Assignment	Reference
855	Proline, tyrosine	20
	$\nu(\text{C}-\text{C})$ , proline + $\delta(\text{CCH})$ ring breathing, tyrosine (protein assignment and polysaccharide)	20
	$\delta(\text{CCH})$ phevalalanine, olefinic (protein assignment and polysaccharide)	126
	Collagen	59
855–856	Proline, hydroxyproline, tyrosine	50
	C–C stretching, proline (collagen assignment)	123
856	Amino acid side chain vibrations of proline and hydroxyproline, as well as a (C–C) vibration of the collagen backbone hydroxyproline (collagen type I)	50
859	Tyrosine, collagen	31
860	Phosphate group	71
	Phosphatidic acid	71
867	Ribose vibration, one of the distinct RNA modes (with 915 and 974 cm <sup>-1</sup> )	103
868, 870, 872	Lipid	141
868	C–C stretching, hypro (collagen assignment)	123
	Monosaccharides ( $\beta$ -fructose), (C–O–C) skeletal mode	64
	Disaccharide (sucrose), (C–O–C) skeletal mode	64
	Polysaccharides, amylase	64
	Polysaccharides, amylopectin	64
869	Proline	31
870	Most probably due to single bond stretching vibrations for the amino acids proline and valine and polysaccharides	53
	C–C stretching, hypro (collagen assignment)	123
873	Hydroxyproline, tryptophan	50
874	C–C stretching, hypro (collagen assignment)	123
875	Antisymmetric stretch vibration of choline group N <sup>+</sup> (CH <sub>3</sub> ) <sub>3</sub> , characteristic of phospholipids	71
	Phosphatidylcholine, sphingomyelin	71
876	$\nu(\text{C}-\text{C})$ , hydroxyproline (protein assignment)	20
	C–C stretching, hydroxyproline (collagen assignment)	123
877	C–C–N <sup>+</sup> symmetric stretching (lipids)	122
	C–O–C ring (carbohydrate)	122
879	Hydroxyproline, tryptophan	50
880	Tryptophan, $\delta(\text{ring})$	64
883	$\rho(\text{CH}_2)$ (protein assignment)	126
884	Proteins, including collagen I	110
885	Disaccharide (cellobiose), (C–O–C) skeletal mode	64

(Continued on next page)

**Table 1**  
Spectral interpretations (*Continued*)

Peak (cm <sup>-1</sup> )	Assignment	Reference
889	Methylene rocking	127
890	Protein bands	2, 3
	Structural protein modes of tumors	27
	$\beta$ -Anomers	71
891	Saccharide band (overlaps with acyl band)	71
893	Backbone, C—C skeletal	103
893–896	Phosphodiester, deoxyribose	106
898	Monosaccharides ( $\beta$ -glucose), (C—O—C) skeletal mode	64
	Disaccharide (maltose), (C—O—C) skeletal mode	64
	Adenine	30
904	C—C skeletal stretching	39
906	Tyrosine	37
907	Formalin contamination peak on fixed tissues	35
912	Calcium oxalate	54
913	Glucose	71
915	Ribose vibration, one of the distinct RNA modes (with 915 and 974 cm <sup>-1</sup> )	103
918	Proline, hydroxyproline	50
	Glycogen and lactic acid	110
920	C—C stretch of proline ring/glucose/lactic acid	30, 31
	C—C, praline ring (collagen assignment)	123
921	Proline ring/glucose/lactic acid/praline ring	51
922	C—C stretch	28
928–940	$\nu$ (C—C), stretching; probably in amino acids proline and valine (protein band)	56
931	Carbohydrates peak for solutions and solids	3
932	Skeletal C—C, $\alpha$ -helix	31
933	Proline, hydroxyproline, $\nu$ (C—C) skeletal of collagen backbone	50
934	C—C backbone (collagen assignment)	123
935	C—C stretching mode of proline and valine and protein backbone ( $\alpha$ -helix conformation)/glycogen (protein assignment)	20, 30
	P(CH <sub>3</sub> ) terminal, proline, valine + $\nu$ (CC) $\alpha$ -helix keratin (protein assignment)	31
937	Proline (collagen type I)	50
	Amino acid side chain vibrations of proline and hydroxyproline, as well as a (C—C) vibration of the collagen backbone	50
	C—C backbone (collagen assignment)	123
	Glycogen	110
	$\nu$ (C—C) residues ( $\alpha$ -helix)	70
	C—C stretching, $\alpha$ -helix (proteins)	122
	C—O—C glycodides (carbohydrates)	122
	Collagen	59

(Continued on next page)

**Table 1**  
Spectral interpretations (*Continued*)

Peak (cm <sup>-1</sup> )	Assignment	Reference
937–938	Proline, hydroxyproline, $\nu(\text{C}-\text{C})$ skeletal of collagen backbone	50
938	C–C stretch backbone	31
941	Skeletal modes (polysaccharides, amylose)	64
	Skeletal modes (polysaccharides, amylopectin)	64
950	Most probably due to single bond stretching vibrations for the amino acids proline and valine and polysaccharides	53
	Calcium phosphate stretch band	51
950–1050	Amphetamine has a group of three bands at this region	125
951	$\nu_s(\text{CH}_3)$ of proteins ( $\alpha$ -helix)	70
956	Carotenoids (absent in normal tissues)	1
957	Hydroxyapatite, carotenoid, cholesterol	31
960	Symmetric stretching vibration of $\nu_1\text{PO}_4^{3-}$ (phosphate of HA)	50
	Calcium–phosphate stretch band (high quantities of cholesterol)	3, 87
	Quinoid ring in-plane deformation	124
	Calcium hydroxyapatite	68
962	Phosphate symmetric stretching vibration of calcium hydroxyapatite	94
963	Unassigned in protein assignments	20
	$\text{CH}_{2,6'}$ out-of-plane bending	121
966	Hydroxyapatite	31
968	Lipids	3
970	Phosphate monoester groups of phosphorylated proteins and cellular nucleic acids	3
971	$\nu(\text{C}-\text{C})$ wagging	70
972	Lipid	141
972–923	C–C backbone (collagen assignment)	123
973	$\rho(\text{CH}_3)$ , $\delta(\text{CCH})$ olefinic (protein assignment)	126
974	Ribose vibration, one of the distinct RNA modes (with 874 and 915 cm <sup>-1</sup> )	103
980	C–C stretching $\beta$ -sheet (proteins)	122
991	Single human RBC, phenylalanine, NADH	38
996	C–O ribose, C–C	3
999	$\nu_{45}(\text{CC})$ , observed in the spectra of single human RBC	98
1000	Phenylalanine	76
	Bound and free NADH	76
1001	Symmetric ring breathing mode of phenylalanine	30, 31, 52
1002	C–C aromatic ring stretching	111
	Phenylalanine	76
1002	Phenylalanine	50
	Phenylalanine (collagen assignment)	123
1003	Phenylalanine, C–C skeletal	103

(Continued on next page)

**Table 1**  
Spectral interpretations (*Continued*)

Peak (cm <sup>-1</sup> )	Assignment	Reference
1004	Phenylalanine ( of collagen)	50
	$\nu_s$ (C—C), symmetric ring breathing, phenylalanine (protein assignment)	20, 126
	Phenylalanine (collagen assignment)	123
	Phenyl breathing mode	126
	$\nu$ (C—C) phenylalanine	70
1005	Phenylalanine (proteins)	122
	Proteins	122
	Symmetric ring breathing of phenylalanine	122
	Carotenoids	141
1006	Carotenoids (absent in normal tissues)	1
	Phenylalanine, $\delta$ (ring)	64
1007	Phenylalanine, carbamide	37
1008	Phenylalanine	102
	$\nu$ (CO), $\nu$ (CC), $\delta$ (OCH), ring (polysaccharides, pectin)	64
1011	Tryptophan ring breathing	52
1016	Carbohydrates peak for solids	3
1017	Ribose	51
1018	Stretching C—O ribose	128
1022	Glycogen	3
1023	Glycogen	3
1025	Carbohydrates peak for solutions	3
	Glycogen	3, 129
1029, 1030	O—CH <sub>3</sub> stretching of methoxy groups	121
1030	Phenylalanine of collagen	50
	$\nu$ (CC) skeletal, keratin (protein assignment)	126
	C—H bending	52
1031	$\delta$ (C—H), phenylalanine (protein assignment)	20
	C—H in-plane bending mode of phenylalanine	30
	Carbohydrate residues of collagen	3
	Phenylalanine, C—N stretching of proteins	103
	C—H in-plane bending mode of phenylalanine	31
1032	CH <sub>2</sub> CH <sub>3</sub> bending modes of collagen and phospholipids	20
	C—C skeletal stretch (one of C—C ring vibration to be expected in aromatic structure of xylene)	111
	Phenylalanine of collagen	50
	Proline (collagen assignment)	123
1033	Differences in collagen content	3
	Phenylalanine mode	103
	$\nu$ (CO), $\nu$ (CC), $\nu$ (CCO) (polysaccharides, pectin)	64
	C—H in-plane phenylalanine (proteins)	122
1034	Phenylalanine of collagen	50
1035	Collagen	130

(Continued on next page)

**Table 1**  
Spectral interpretations (*Continued*)

Peak (cm <sup>-1</sup> )	Assignment	Reference
1040, 1041	Formalin peaks appearing in the fixed normal and tumor tissues	131
1043	Carbohydrates peak for solutions and solids	3
	Proline (collagen assignment)	123, 132
1044	$\nu_3\text{PO}_4^{3-}$ (symmetric stretching vibration of $\nu_3\text{PO}_4^{3-}$ of HA)	50
	Proline	51
1048	Glycogen	110
1053	C—O stretching, C—N stretching (protein)	103
1055	In the solid, the most significant difference between the two nucleic acids is the ratio intensity of the bands in this area	3
1057	Lipids	3
1060–1095	$\text{PO}_2^-$ stretching (DNA/RNA)	122
	Chain C—C stretching (lipids)	122
	C—O, C—C stretching (carbohydrates)	122
1060–1130	C—C skeletal stretching	127
1061	C—C in-plane bending (one of C—C ring vibration to be expected in aromatic structure of xylene)	111
	C—N stretching	52
	Ceramide	91
1063	C—C skeletal stretch random conformation	111
1064	Skeletal C—C stretch of lipids	31
	Acyl chains	71
	$\nu(\text{C—C})$ <i>trans</i>	70
1065	Palmitic acid	71
	Fatty acid	71
	Proline	51
1066–1067	Proline (collagen assignment)	123
1070	Triglycerides (fatty acids)	94
1070–1090	Symmetric $\text{PO}_2^-$ stretching of DNA (represents more DNA in cell)	140
1071	Glucose	71
1073	Carbonate symmetric stretching vibration of calcium carbonate apatite	94
	Triglycerides (fatty acids)	94
1074	Glucose, triglycerides, C—C (lipid)	38
1076	C—C (lipid in normal tissues)	76
	Symmetric stretching vibration of $\nu_3\text{PO}_4^{3-}$ (phosphate of HA)	50
1078	$\nu(\text{C—C})$ or $\nu(\text{C—O})$ , phospholipids (lipid assignment)	20
	Pronounced symmetric phosphate stretch	20
	Phospholipids	20
	C—C or C—O stretching mode of phospholipids	20
	Carbohydrate peak for solids	3
	C—C or C—O stretch (lipid), C—C or $\text{PO}_2$ stretch (nucleic acid)	31
	$\nu(\text{CC})$ skeletal	126

(Continued on next page)

**Table 1**  
Spectral interpretations (*Continued*)

Peak (cm <sup>-1</sup> )	Assignment	Reference
1078	$\nu(\text{CC})$ vitor <sub>s</sub> (PO <sub>2</sub> <sup>-</sup> ) nucleic acid	126
1080	Amide II (?)	3
	Typical phospholipids	76
	Phosphate vibrations (phosphodiester groups in nucleic acids)	22
	Collagen	130
	Tryptophan	30
1081	$\nu_1\text{CO}_3^{2-}$ , $\nu_3\text{PO}_4^{3-}$ , $\nu(\text{C}-\text{C})$ skeletal of acyl backbone in lipid ( <i>gauche</i> conformation)	50
1082	Carbohydrate residues of collagen	3
	Carbohydrates peak for solutions	3
	Nucleic acids	3
1083	C-N stretching mode of proteins (and lipid mode of lesser degree)	30
	C-N stretching mode of proteins (and lipid mode to a lesser degree)	31
1084	Phosphodiester groups in nucleic acids	3
1086	$\nu(\text{C}-\text{C})$ <i>gauche</i>	70
1087	$\nu_1\text{CO}_3^{2-}$ , $\nu_3\text{PO}_4^{3-}$ , $\nu(\text{C}-\text{C})$ skeletal of acyl backbone in lipid ( <i>gauche</i> conformation)	50
1087–1090	C-C stretch	31
	PO <sub>2</sub> <sup>-</sup> stretch	
1090	Symmetric phosphate stretching vibrations	3
1092–1093	Phosphodioxy	106
1093	Symmetric PO <sub>2</sub> <sup>-</sup> stretching vibration of the DNA backbone; phosphate backbone vibration as a marker mode for the DNA concentration; C-N of proteins	91, 103
1094	DNA	76
	C-N stretching	52
1095	Lipid	133
	$\nu(\text{C}-\text{N})$	50
	Phosphodioxy group (PO <sub>2</sub> <sup>-</sup> in nucleic acids)	122
1096	Phosphodioxy (PO <sub>2</sub> <sup>-</sup> ) groups	71
1099	$\nu(\text{C}-\text{N})$	50
1100	C-C vibration mode of the <i>gauche</i> -bonded chain	127
1100–1375	Several bands of moderate intensity, belonging to amide III and other groups (proteins)	70
1100–1800	$\nu(\text{C}-\text{C})$ ; lipids, fatty acids	64
1101	O-P-O backbone stretch of DNA	28
1104	Phenylalanine (proteins)	70
1105	Carbohydrates peak for solutions	3
1111	Benzoid ring deformation	124
1112	Saccharide band (overlaps with acyl band)	71
1115, 1116	CH <sub>2,6</sub> in-plane bend and C <sub>1</sub> -C <sub><math>\alpha</math></sub> -H <sub><math>\alpha</math></sub> bend	121
1117	Glucose	71

(Continued on next page)

**Table 1**  
Spectral interpretations (*Continued*)

Peak (cm <sup>-1</sup> )	Assignment	Reference
1117–1119	C–C stretch (breast lipid)	31
1120	The strong C–O band of ribose (serves as a marker band for RNA in solutions)	3
	Carotene	76
1122	$\nu_{22}$ (porphyrin half ring), observed in the spectra of single human RBC	98
	$\nu_s$ (CC) skeletal	126
	$\nu_{\text{sym}}$ (C–O–C) (polysaccharides, cellulose)	64
	$\nu$ (C–C) <i>trans</i>	70
1123	(C–N), proteins (protein assignment)	20
	C–C stretching mode of lipids and protein, C–N stretch	30, 31
	Glucose	31
1124	$\nu$ (C–C) skeletal of acyl backbone in lipid ( <i>trans</i> conformation)	50
1126	Paraffin	3
	$\nu$ (C–C) skeletal of acyl backbone in lipid ( <i>trans</i> conformation)	50
	C–N stretching vibration (protein vibration)	103
	$\nu$ (C–O) + $\nu$ (C–C), disaccharides, sucrose	64
1126	C–N stretching	39
1127	$\nu$ (C–N)	70
1128	C–N stretching (proteins)	122
	C–O stretching (carbohydrates)	122
	Ceramide	59
1128–1129	$\nu$ (C–C) skeletal of acyl backbone in lipid ( <i>trans</i> conformation)	50
1130	C–C skeletal stretch transconformation	111
	Phospholipid structural changes ( <i>trans</i> versus <i>gauche</i> isomerism)	129
	Acyl chains	71
1131	Palmitic acid	71
	Fatty acid	71
	C–C skeletal stretching	39
1149	Carbohydrates peak for solids	3
1150	Glycogen	3
	Carotenoid	2
1152	$\nu$ (C–N), proteins (protein assignment)	20
	$\nu$ (C–C), carotenoids	20
	Carotenoid peaks due to C–C and conjugated C=C band stretch	20
1153	Carbohydrates peak for solutions	3
1154	$\beta$ -Carotenes	30
1155–1157	Carotenoids	141
1155	C–C (and C–N) stretching of proteins (also carotenoids)	30, 31
	Glycogen	3
	$\nu$ (C–C); diagnostic for the presence of a carotenoid structure, most likely a cellular pigment	102

(Continued on next page)

**Table 1**  
Spectral interpretations (*Continued*)

Peak (cm <sup>-1</sup> )	Assignment	Reference
1156	C—C, C—N stretching (protein)	103
1156–1157	Carotenoids (absent in normal tissue)	1
1157	In-plane vibrations of the conjugated =C—C= β-Carotene accumulation (C=C stretch mode)	95 94
1158	C—C/C—N stretching (proteins)	122
1160	C—C/C—N stretching (proteins)	38
1161	Deformative vibrations of quinoid ring	124
1163	Tyrosine (collagen type I)	50
	Tyrosine	50
1167	N=Quinoid ring=N stretching and C—H in plane bending	124
1168	Lipids	3
	ν(C=C) δ(COH) (lipid assignment)	126
	ν(C—C), carotenoids	126
1169	Tyrosine (collagen type I)	50
	Tyrosine	50
1170	C—H in-plane bending mode of tyrosine	30, 31
1171	Tyrosine (collagen type I)	50
	Tyrosine	50
	(CH) Phenylalanine, tyrosine	70
1172	δ(C—H), tyrosine (protein assignment)	20
1173	Cytosine, guanine	106
	Tyrosine (collagen type I)	50
1174	Tyrosine, phenylalanine, C—H bend (protein)	103
1175–1176	Cytosine, guanine	106
1176	C—H bending tyrosine (proteins)	122
1177	Cytosine, guanine	106
1180	Cytosine, guanine	106
1180–1184	Cytosine, guanine, adenine	31
1185–1300	Antisymmetric phosphate vibrations	130
1199	Tryptophan ring breathing	39
1200	Nucleic acids and phosphates	130
	Aromatic C—O and C—N	134
1200–1300	Amide III (proteins)	122
1200–1350	Amide III; due to C—N stretching and N-H bending	76, 103
1200–1360	Electronic structure of nucleotides	103
1203	C—C <sub>6</sub> H <sub>5</sub> stretch mode (one of C—C ring vibration to be expected in aromatic structure of xylene)	11
1204	Amide III and CH <sub>2</sub> wagging vibrations from glycine backbone and proline side chains	3
	Collagen	
	Tyrosine, phenylalanine (IgG)	129, 130
1205	Differences in collagen content	3
1206	Hydroxyproline, tyrosine (collagen assignment)	123
	Hydroxyproline, tyrosine	31

(Continued on next page)

**Table 1**  
Spectral interpretations (*Continued*)

Peak (cm <sup>-1</sup> )	Assignment	Reference
1208	$\nu(\text{C}-\text{C}_6\text{H}_5)$ , tryptophan, phenylalanine (protein assignment)	20, 126
	Tryptophan	50
	A, T (ring breathing modes of the DNA/RNA bases); amide III (protein)	103
1209	Tryptophan and phenylalanine $\nu(\text{C}-\text{C}_6\text{H}_5)$ mode	30, 31, 122
1210	$\text{C}-\text{C}_6\text{H}_5$ stretching mode in tyrosine and phenylalanine	78
	$\nu_{18}(\delta: \text{C}_m\text{H})$ , observed in the spectra of single human RBC	102
1216	Stretching of C-N	124
1220	C=N=C stretching	124
1220, 1221	Amide III ( $\beta$ -sheet)	31
1220-1284	T, A (DNA/RNA)	122
	Amide III (proteins)	122
1220-1300	Amide III (arising from coupling of C-N stretching and N-H bonding; can be mixed with vibrations of side chains); (protein band)	53
1223	$\nu(\text{PO}_2^-)$ , nucleic acids	20
	Cellular nucleic acids	20
	A concerted ring mode	104
	Proteins, including collagen I	110
1224	Amide III ( $\beta$ sheet structure)	70
1230	Antisymmetric phosphate stretching vibration	3
1230-1300	Amide III (arising from coupling of C-N stretching and N-H bonding; can be mixed with vibrations of side chains)	3
1234	A concerted ring mode	104
1235	Amide III	64
1237	Amide III and CH <sub>2</sub> wagging vibrations from glycine backbone and proline side chains	3
1239	Amide III	111
1240	One of the two most distinct peaks for RNA (with 813 cm <sup>-1</sup> )	103
	Differences in collagen content	3
	Asymmetric phosphate [PO <sub>2</sub> <sup>-</sup> (asym.)] stretching modes	30
	Collagen	130
1241	Asymmetric phosphate [PO <sub>2</sub> <sup>-</sup> (asym.)] stretching modes (phosphate stretching modes originate from the phosphodiester groups of nucleic acids and suggest an increase in the nucleic acids in the malignant tissues). (Generally, the PO <sub>2</sub> <sup>-</sup> groups of phospholipids do not contribute to these bands)	50
1242	Amide III ( $\beta$ sheet and random coils)	70
1243	Amide III	3
	Asymmetric phosphate [PO <sub>2</sub> <sup>-</sup> (asym.)] stretching modes (phosphate stretching modes originate from the phosphodiester groups of nucleic acids and suggest an increase the in nucleic acids in the malignant tissues). (Generally, the PO <sub>2</sub> <sup>-</sup> groups of phospholipids do not contribute to these bands)	

(Continued on next page)

**Table 1**  
Spectral interpretations (*Continued*)

Peak (cm <sup>-1</sup> )	Assignment	Reference
1243	C—O <sub>4</sub> aromatic stretch	50
	Amide III of collagen (CH <sub>2</sub> wagging, C—N stretching) and pyrimidine bases (C, T)	31, 121
1245	Amide III	64
1246	Amide III (of collagen)	50
1247	Amide III (collagen assignment)	123
1247–1248	Guanine, cytosine (NH <sub>2</sub> )	106
1248	Amide III	28
1250	Amide III	102
1250–1252	Guanine, cytosine (NH <sub>2</sub> )	106
1252	C—O <sub>4</sub> aromatic stretch	121
1254	Formalin contamination on fixed tissues	35
	C—N in plane stretching	124
1255	Lipids	3
1257	A, T (ring breathing modes of the DNA/RNA bases); amide III (protein)	103
1258	Amide III, adenine, cytosine	31
1258	CH <sub>2</sub> in plane deformation	38
1259	Guanine, cytosine (NH <sub>2</sub> )	106
	Amide III	123
1260	Amide III (protein band)	3
	Protein band	2
1260	Second amide	1
	Amide III (unordered)	31
	Structural protein modes of tumors	27
	Amide III vibration mode of structural proteins	94
	CH <sub>2</sub> in-plane deformation (lipids)	113
1263	T, A (ring breathing modes of the DNA/RNA bases); =C—H bend (protein)	103
1263, 1265, 1259	Lipids	141
1264	Triglycerides (fatty acids)	94
1265	Amide III of collagen	35
	Amide III (collagen assignment)	123
	Amide III	126
	$\nu(\text{CN})$ , $\delta(\text{NH})$ amide III, $\alpha$ -helix, collagen (protein assignment)	126
1266	Amide III (of proteins in the $\alpha$ -helix conformation)	20, 50
1266	$\nu(\text{CN})$ , $\delta(\text{NH})$ amide III, $\alpha$ -helix, collagen, tryptophan (protein assignment)	20
	$\delta(=\text{C—H})$ <i>cis</i>	64
	Amide III ( $\alpha$ -helix)	70
1267	C—H (lipid in normal tissue)	76
	Amide III (collagen assignment)	
1268	$\Delta(=\text{C—H})$ (phospholipids)	70

(Continued on next page)

**Table 1**  
Spectral interpretations (*Continued*)

Peak (cm <sup>-1</sup> )	Assignment	Reference
1268–1269	Amide III (collagen assignment)	123
1270	Typical phospholipids	76
	Amide III band in proteins	52
	Has traditionally been attributed to amide III, a C–N stretch from alpha helix proteins	112
	C=C groups in unsaturated fatty acids	71
1272–1273	CH <sub>α'</sub> rocking	121
1273	δ (C=CH)	28
1275	Amide III	64
1278	Proteins, including collagen I	110
1279	Amide III (α-helix)	31
1280	Amide III and CH <sub>2</sub> wagging vibrations from glycine backbone and proline side chains	3
	Collagen	
	Nucleic acids and phosphates	130
1283	Differences in collagen content	3
1287–1288	Cytosine	106
1288	Phosphodiester groups in nucleic acids	3
1290	Cytosine	106
1290–1400	CH bending	135
1291–1292	Cytosine	106
1294	Methylene twisting	127
1296	CH <sub>2</sub> deformation	111
	Ceramide	59
1297	Palmitic acid	38
1298	Palmitic acid	71
	Acyl chains	71
	Fatty acids	71
1299–1300	CH <sub>2</sub> deformation (lipid)	31
1300, 1301, 1305, 1305	Lipid	141
1300	–(CH <sub>2</sub> ) <sub>n</sub> ; in-plane twist vibration (lipid band)	53
	Fatty acids	3
	Fatty acids	2
	δ(CH <sub>2</sub> ); lipids, fatty acids	64
	CH <sub>2</sub> twisting modes	126
	δ(CH), τ(CH <sub>2</sub> ) (α-helix)	70
	CH <sub>2</sub> twisting (lipids)	70
	CH <sub>2</sub> twisting and wagging (lipids)	113

(Continued on next page)

**Table 1**  
Spectral interpretations (*Continued*)

Peak (cm <sup>-1</sup> )	Assignment	Reference
1301	Assign from Parker (lipid in normal tissue)	76
	Triglycerides (fatty acids)	94
	$\tau(\text{CH}_2)$ , lipids	70
	C—H vibration (lipids)	122
	Lipids	122
	CH <sub>2</sub> twisting (lipids)	122
1302	$\delta(\text{CH}_2)$ twisting, wagging, collagen (protein assignment)	20, 126
	$\delta(\text{CH}_2)$ twisting, wagging, phospholipids (lipid assignment)	20, 126
	CH <sub>3</sub> /CH <sub>2</sub> twisting or bending mode of lipid/collagen	50
	Amide III (protein)	103
	Methylene bending mode (a combination of proteins and phospholipids)	35
1303–1304	CH <sub>3</sub> , CH <sub>2</sub> twisting (collagen assignment)	123
1304	CH <sub>2</sub> deformation (lipid), adenine, cytosine	31
1307	CH <sub>3</sub> /CH <sub>2</sub> twisting or bending mode of lipid/collagen	50
	CH <sub>3</sub> /CH <sub>2</sub> twisting, wagging, and/or bending mode of collagens and lipids	50
1308	C—N asymmetric stretching in asymmetric aromatic amines	124
1309	CH <sub>3</sub> /CH <sub>2</sub> twisting or bending mode of lipid/collagen	50
	CH <sub>3</sub> /CH <sub>2</sub> twisting, wagging, and/or bending mode of collagens and lipids	50
1313	CH <sub>3</sub> CH <sub>2</sub> twisting mode of collagen/lipid	30, 31
1314	CH <sub>3</sub> CH <sub>2</sub> twisting mode of collagen	81
1315	Guanine (B, Z-marker)	106
1317–1319	Guanine (B, Z-marker)	106
1318	G (ring breathing modes of the DNA/RNA bases); C—H deformation (protein)	103
	Amide III ( $\alpha$ -helix)	70
1319	Guanine (B, Z-marker)	106
	CH <sub>3</sub> CH <sub>2</sub> twisting (collagen assignment)	123
	G (DNA/RNA)	122
1320	CH deformation (proteins)	122
	Amide III ( $\alpha$ -helix)	70
1321	CH <sub>2</sub> deformation of lipids	28
	CH <sub>3</sub> CH <sub>2</sub> twisting, collagen	20
1322	CH <sub>3</sub> CH <sub>2</sub> twisting and wagging in collagen	20
	CH <sub>3</sub> CH <sub>2</sub> deforming modes of collagen and nucleic acids	35
	Guanine (B, Z marker)	106
1323	CH deformation	39
	CH <sub>3</sub> CH <sub>2</sub> wagging mode present in collagen and purine bases of DNA	78
1325–1330	CH <sub>3</sub> CH <sub>2</sub> wagging mode in purine bases of nucleic acids	59, 112

(Continued on next page)

**Table 1**  
Spectral interpretations (*Continued*)

Peak (cm <sup>-1</sup> )	Assignment	Reference
1330	Typical phospholipids	76
	Region associated with DNA and phospholipids	27
	Collagen	130
	Nucleic acids and phosphates	130
1332	C—C stretch of phenyl (1) and C <sub>3</sub> —C <sub>3</sub> stretch and C <sub>5</sub> —O <sub>5</sub> stretch CH <sub>α</sub> in-plane bend	121
1333	Guanine	106
1335	CH <sub>3</sub> CH <sub>2</sub> wagging, collagen (protein assignment)	20
	CH <sub>3</sub> CH <sub>2</sub> wagging, nucleic acid	20
	CH <sub>3</sub> CH <sub>2</sub> wagging mode of collagen and polynucleotide chain (DNA purine bases)	30
	CH <sub>3</sub> CH <sub>2</sub> twisting and wagging in collagen	20
	Cellular nucleic acids	20
	CH <sub>3</sub> CH <sub>2</sub> deforming modes of collagen and nucleic acids	35
	An unassigned mode	104
1335–1345	CH <sub>3</sub> CH <sub>2</sub> wagging mode of collagen	31
1335–1336	Guanine	106
1336	Polynucleotide chain (DNA purine bases)	31
	δ(CH <sub>3</sub> ) δ(CH <sub>2</sub> ) twisting, collagen (protein assignment)	126
1337	Amide III and CH <sub>2</sub> wagging vibrations from glycine backbone and proline side chain	3
	A, G (ring breathing modes in the DNA bases); C—H deformation (protein)	103
1337, 1339	Tryptophan	50
	CH <sub>2</sub> /CH <sub>3</sub> wagging, twisting and/or bending mode of collagens and lipids	50
	CH <sub>2</sub> /CH <sub>3</sub> wagging and twisting mode in collagen, nucleic acid and tryptophan	50
1339	C—C stretch of phenyl (1) and C <sub>3</sub> —C <sub>3</sub> stretch and C <sub>5</sub> —O <sub>5</sub> stretch CH <sub>α</sub> in-plane bend	144
1340	Nucleic acid mode	1
	Differences in collagen content	3
	Nucleic acid modes indicating the nucleic acid content in tissues	145
1341	A or G of DNA	67
1342	G (DNA/RNA)	122
	CH deformation (proteins and carbohydrates)	122
1343	CH <sub>3</sub> , CH <sub>2</sub> wagging (collagen assignment)	123
	Glucose	49
1343–1344	δ(CH), residual vibrations	70
1347	An unassigned mode	104
1350	Carbon particle	33
1355, 1357	Guanine (N <sub>7</sub> , B, Z-marker)	106
1359	Tryptophan	50
1360, 1364	Tryptophan	37, 64

(Continued on next page)

**Table 1**  
Spectral interpretations (*Continued*)

Peak (cm <sup>-1</sup> )	Assignment	Reference
1361–1363, 1365	Guanine (N <sub>7</sub> , B, Z-marker)	106
1365	Tryptophan	50
1367	$\nu_s$ (CH <sub>3</sub> ) (phospholipids)	70
1369	Guanine, TRP (protein), porphyrins, lipids	34
1370	The most pronounced saccharide band	71
1371	CH <sub>3</sub> stretching	39
<b>1373</b>	<b>T, A, G (ring breathing modes of the DNA/RNA bases)</b>	103
1378	Paraffin	3
1379	$\delta$ CH <sub>3</sub> symmetric (lipid assignment)	126
1383	CH <sub>3</sub> band	38
1386	CH <sub>3</sub> band	31
1391	CH rocking	121
1392	C–N stretching, quinoid ring–benzoid ring–quinoid ring	124
1393	CH rocking	121
1396	$\beta$ -carotene	29
1398	C=O symmetric stretch	111
	CH <sub>2</sub> deformation	50
1400	NH in-plane deformation	104
1400–1430	$\nu$ (C=O)O <sup>-</sup> (amino acids, aspartic and glutamic acid)	64
1401	Bending modes of methyl groups (one of vibrational modes of collagen)	3
1404	CH deformation	39
1406	$\nu_s$ COO <sup>-</sup> (IgG?)	70
1409	$\nu_s$ COO <sup>-</sup> (IgG?)	70
1417	C=C stretching in quinoid ring	124
1420–1450	CH <sub>2</sub> scissoring vibration (lipid band)	53
1420–1470	(prominent peak at 1445 cm <sup>-1</sup> being of diagnostic significance) CH <sub>2</sub> bending mode of proteins and lipids	81
1420–1480	G, A (DNA, RNA)	122
	CH deformation (DNA/RNA and proteins and lipids and carbohydrates)	122
1420–1421	Deoxyribose (B, Z-marker)	106
1421	A, G (ring breathing modes of the DNA/RNA bases)	103
1422	Deoxyribose (B, Z-marker)	106
1423	NH in-plane deformation	104
1424	Deoxyribose (B, Z-marker)	106
1436	CH <sub>2</sub> scissoring	106
1437	CH <sub>2</sub> (lipids in normal tissue)	76
	CH <sub>2</sub> deformation (lipid)	31
	Acyl chains	71
1437–1442	CH <sub>2</sub> deformation	71
1437–1453	CH <sub>2</sub> deformation	113
1438–1440, 1442–1443	Lipid	141

(Continued on next page)

**Table 1**  
Spectral interpretations (*Continued*)

Peak (cm <sup>-1</sup> )	Assignment	Reference	
1439	CH <sub>2</sub> bending mode in normal tissue	21	
	CH <sub>3</sub> ,CH <sub>2</sub> deformation (collagen assignment)	123	
	CH <sub>2</sub> scissoring	119	
	CH <sub>2</sub> deformation in normal breast tissue	123	
	CH <sub>2</sub> deformation	123	
	CH <sub>2</sub>	76	
	δ(CH <sub>2</sub> ) (lipids)	70	
1440	CH <sub>2</sub> and CH <sub>3</sub> deformation vibrations	2	
	CH deformation	71	
	Cholesterol, fatty acid band	71	
	δ(CH <sub>2</sub> ) (lipids)	70	
	CH <sub>2</sub> bending (lipids)	70, 113	
1441	CH <sub>2</sub> scissoring and CH <sub>3</sub> bending in lipids	78	
	Cholesterol and its esters	94	
	C–H bending mode of accumulated lipids in the vecrotic core of the atheromatous plaque	94	
1442	Fatty acids	2, 3	
	CH <sub>2</sub> bending mode	1	
	Due to changes in chemical environment of the CH <sub>2</sub> bending mode	2	
	CH <sub>3</sub> , CH <sub>2</sub> deformation (collagen assignment)	123	
	Triglycerides (fatty acids)	94	
1443	CH <sub>2</sub> deformation (lipids and proteins)	31	
	Triglycerides (fatty acids)	94	
1444	Cholesterol band (associated to atherosclerotic spectrum)	94	
	ν <sub>28</sub> (C <sub>α</sub> C <sub>m</sub> ), observed in the spectra of single human RBC	98	
	δ(CH <sub>2</sub> ), lipids, fatty acids	63	
1445	δ(CH <sub>2</sub> ), δ(CH <sub>3</sub> ), collagen (protein assignment)	20, 126	
	δ(CH <sub>2</sub> ), δ(CH <sub>3</sub> ), scissoring, phospholipids (lipid assignment)	20, 126	
	CH <sub>2</sub> CH <sub>3</sub> bending modes of collagen and phospholipids	20, 65	
	CH <sub>2</sub> scissoring	20	
1445	CH <sub>2</sub> bending mode of proteins and lipids being of diagnostic significance	81	
	CH <sub>2</sub> bending and scissoring modes of collagen and phospholipids	35	
	Methylene bending mode (a combination of proteins and phospholipids)	35	
	CH <sub>2</sub> bending modes	126	
	CH <sub>2</sub> deformation	113	
	1446	CH <sub>2</sub> bending mode of proteins and lipids	30, 31
		CH <sub>2</sub> deformation	123

(Continued on next page)

**Table 1**  
Spectral interpretations (*Continued*)

Peak (cm <sup>-1</sup> )	Assignment	Reference
1447	CH <sub>2</sub> bending mode of proteins and lipids	111
	CH <sub>2</sub> deformation (protein vibration), a marker for protein concentration	103
	δ <sub>as</sub> (CH <sub>3</sub> ) δ(CH <sub>2</sub> ) of proteins	70
1448	CH <sub>2</sub> CH <sub>3</sub> deformation	50
	CH <sub>2</sub> deformation	123
	CH <sub>2</sub>	76
	Collagen	34
	CH deformation	29
1449	C—H vibration (proteins)	122
	C—H vibration (lipids)	122
	Lipids	122
1450	CH <sub>2</sub> bending	51, 62, 76
	CH <sub>2</sub> bending mode in malignant tissues	21
	Bending modes of methyl groups (one of the vibrational modes of collagen)	
	Methylene deformation in biomolecules	3
	CH <sub>2</sub> deformation in IDC breast tissue	123
	C—H deformation bands (CH functional groups in lipids, amino acid side chains of the proteins and carbohydrates)	102
	δ(C—H)	102
	CH <sub>2</sub> bending (proteins)	70
1451	CH <sub>2</sub> CH <sub>3</sub> deformation	70
	CH <sub>2</sub> CH <sub>3</sub> deformation (collagen assignment)	123
1453	Protein bands	2, 3
	Umbrella mode of methoxyl (4)	121
	C—H bending mode of structural proteins	94
1453	Structural protein modes of tumors	27
1454	CH <sub>2</sub> stretching/CH <sub>3</sub> asymmetric deformation	111
	Overlapping asymmetric CH <sub>3</sub> bending and CH <sub>2</sub> scissoring (is associated with elastin, collagen, and phospholipids)	81
	Collagen and phospholipids	27
1455	Deoxyribose	106
	δ(CH <sub>2</sub> )	70
1457	Deoxyribose	106
1458	Nucleic acid modes	1
	Nucleic acid modes indicating the nucleic acid content in tissues	137, 145
1459	Deoxyribose	106
	δ(CH <sub>2</sub> )	70
1460	CH <sub>2</sub> /CH <sub>3</sub> deformation of lipids and collagen	50
	CH <sub>2</sub> wagging, CH <sub>2</sub> /CH <sub>3</sub> deformation	50
	Deoxyribose	106
1462	δCH <sub>2</sub> , disaccharides, sucrose	64

(Continued on next page)

**Table 1**  
Spectral interpretations (*Continued*)

Peak (cm <sup>-1</sup> )	Assignment	Reference
1463	Fermi interaction $\delta(\text{CH}_2)$ and $\gamma(\text{CH}_2)$	70
1465	Lipids	3
1470	C=N stretching	124
1472	Paraffin	3
1477	Calcium oxalate	47
1480–1575	Amide II (largely due to a coupling of CN stretching and in-plane bending of the N-H group; is not often used for structural studies per se because it is less sensitive and is subject to interference from absorption bounds of amino acid side chain vibrations)	3
1485	G, A (ring breathing modes in the DNA bases)	103
	Nucleotide acid purine bases (guanine and adenine)	31
1485–1550	NH <sub>3</sub> <sup>+</sup>	111
1487–1488	Guanine (N <sub>7</sub> )	106
1488	Collagen	34
1490	DNA	76
	Formalin peak appearing in the fixed normal and tumor tissues	35
1491	C–N stretching vibration coupled with the in-plane C–H bending in amino radical cations	111
1492	Formalin peak appearing in the fixed normal and tumor tissues	35
1499	C–C stretching in benzenoid ring	124
1506	N-H bending	124
1506, 1508		
1510	Cytosine	106
1510	A (ring breathing modes in the DNA bases)	103
1513	Cytosine	106
1514	$\nu(\text{C}=\text{C})$ ; diagnostic for the presence of a carotenoid structure, most likely a cellular pigment	102
	$\nu(\text{C}=\text{C})$ carotenoids	126
1515	Cytosine	106
1515, 1525		
1526	Carotenoids	141
1517	$\beta$ -Carotene accumulation (C–C stretch mode)	94
1518	$\nu(\text{C}=\text{C})$ , porphyrin	20
	Carotenoid peaks due to C–C and conjugated C=C band stretch	20
1520	Carotene	76
1520–1538	-C=C- carotenoids	29, 31
1524	Carotenoid (absent in normal tissues)	1
1525	In-plane vibrations of the conjugated -C=C-	95
1528	Carotenoid (absent in normal tissues)	1
1540–1680	Amide carbonyl group vibrations and aromatic hydrogens	134
1542	Single human RBC, amide II	38
1543	$\nu_{11}(\text{C}_\beta\text{C}_\beta)$ , observed in the spectra of single human RBC	102

(Continued on next page)

**Table 1**  
Spectral interpretations (*Continued*)

Peak (cm <sup>-1</sup> )	Assignment	Reference
1544	Amide II	3
1545	C <sub>6</sub> -H deformation mode	104
1546	Bound and free NADH	76
	Tryptophan	67
1547	Proline	29
1548	Tryptophan	30, 31
1552	Tryptophan	20
	$\nu(\text{C}=\text{C})$ , tryptophan (protein assignment)	20
	$\nu(\text{C}=\text{C})$ , porphyrin	20
1554	Amide II	111
1558	Tryptophan	50
	$\nu(\text{CN})$ and $\delta(\text{NH})$ amide II (protein assignment)	126
	$\nu(\text{C}=\text{C})$ porphyrin	126
	Tyrosine, amide II, COO <sup>-</sup>	70
1560	Tryptophan	52
1560–1600	COO <sup>-</sup>	6
1573	Guanine, adenine, TRP (protein)	31
1575	Ring breathing modes in the DNA bases	103
	G, A (ring breathing modes of the DNA/RNA bases)	
1576	Nucleic acid mode	1
	Nucleic acid modes indicating the nucleic acid content in tissues	137
<b>1576, 1577</b>	<b>Guanine (N<sub>3</sub>)</b>	106
1577	Bound and free NADH	76
	IgG?	70
1578	Guanine (N <sub>3</sub> )	106
	Guanine, adenine	122
1579	Pyrimidine ring (nucleic acids) and heme protein	30, 31
1580	C–C stretching	124
	C=C bending mode of phenylalanine	100
1582	$\delta(\text{C}=\text{C})$ , phenylalanine	20
	Phenylalanine	20
1583	C=C bending mode of phenylalanine	81
1585	C=C olefinic stretch	111
	C=C olefinic stretch (protein assignment)	127
1585	Phenylalanine, hydroxyproline	38
1586, 1588	Phenylalanine, hydroxyproline	50
1590	Carbon particles	33
1593	C=N and C=C stretching in quinoid ring	124
1600–1800	Amide I band of proteins; due to C=O stretching	52, 103
	Amide I (which is due mostly to the C=O stretching vibrations of the peptide backbone; has been used the most for structural studies due to its high sensitivity to small changes in molecular geometry and hydrogen bonding of peptide group)	3

(Continued on next page)

**Table 1**  
Spectral interpretations (*Continued*)

Peak (cm <sup>-1</sup> )	Assignment	Reference
1602	Phenylalanine	20
	$\delta(\text{C}=\text{C})$ , phenylalanine (protein assignment)	50
1603	C=C in-plane bending mode of phenylalanine and tyrosine	30, 31
	Ring C—C stretch of phenyl (1)	121
1605	Cytosine (NH <sub>2</sub> )	102
	Ring C—C stretch of phenyl (1)	121
	Phenylalanine, tyrosine, C=C (protein)	103
1606	C=C bending	39
1607	Tyrosine, phenylalanine ring vibration	70
	C=C phenylalanine, tyrosine	122
1608, 1609	Cytosine (NH <sub>2</sub> )	106
1610	Cytosine (NH <sub>2</sub> )	106
1614	Tyrosine	50
1615	Tyrosine, tryptophan, C=C (protein)	103
	Adenine	30
1616	C=C stretching mode of tyrosine and tryptophan	30, 31
1617	$\nu(\text{C}_a\text{C}_b)$ , observed in the spectra of single human RBC	102
	C=C phenylalanine, tyrosine	122
1618	$\nu(\text{C}=\text{C})$ , tryptophan (protein assignment)	20
	$\nu(\text{C}=\text{C})$ , porphyrin	20
	Tryptophan	20
	Bound and free NADH	76
1620	$\nu(\text{C}=\text{C})$ , porphyrin	126
1620–1750	In-plane double end vibrations of bases; the spectra in this region are very sensitive to base-pairing interactions and base-stacking effects; i.e., effects of hydrogen bond formation	3
1622	Tryptophan	50
	Tryptophan and/or $\beta$ -sheet	50
	Tryptophan (IgG)	70
1623	Tryptophan	38
1628	C $_{\alpha}$ =C $_{\alpha}$ stretch	121
	Amide C=O stretching absorption for the $\beta$ -form polypeptide films	6
1634	Amide I	3
1635	Differences in collagen content	3
1637	Amide I band	111
	Amide I band (both $\alpha$ -helix and $\beta$ -structure)	70
1638	Intermolecular bending mode of water	31
	Very weak and broad $\nu_2$ mode of water	70
1640–1680	Amide I band (protein band)	150
1645	Amide I ( $\alpha$ -helix)	31
1647	Random coils	70

(Continued on next page)

**Table 1**  
Spectral interpretations (*Continued*)

Peak (cm <sup>-1</sup> )	Assignment	Reference
1650	(C=C) amide I Protein amide I absorption Amide I	76  55
1652, 1653	Lipid (C=C stretch)	31
1653–1655	Lipid	141
1653	Carbonyl stretch (C=O), amide I	38, 104
1654	Due to a combination of C=C stretch and the amide I bands + amide I Amide I (collagen assignment) C=C stretch Amide I (C=O stretching mode of proteins, $\alpha$ -helix conformation)/C=C lipid stretch Collagen	3, 21  123 123 31  27
1655	Amide I (of collagen) C=C (of lipids in normal tissues, not that of amide I) $\nu$ (C=O) amide I, $\alpha$ -helix, collagen Amide I (C=O stretching mode of proteins, $\alpha$ -helix conformation)/C=C lipid stretch In normal tissues: C=C of lipids (and not amide I) C=O stretching of collagen and elastin (protein assignment) Amide I of proteins Amide I (collagen assignment) Amide I (typically associated with collagen) Amide I ( $\alpha$ -helix), amide I	50 77 20, 62, 126 30, 31  20 20 35, 126 123 112 39, 64
1655–1680	Amide I (proteins) C=O stretching (lipids)	122 122
1656	C=C (lipids) Amide I (proteins)	70 70
1655–1680	T, G, C (ring breathing modes of the DNA/RNA bases); amide I (protein)	103
1656	$\nu$ (C=C) <i>cis</i> (phospholipids)	70
1657	Fatty acids Amide I (collagen assignment) Triglycerides (fatty acids)	2, 3 123 94
1658	Amide I ( $\alpha$ -helix)	70
1659	Amide I vibration (collagen like proteins) Amide C=O stretching absorption for the $\alpha$ -folded polypeptide films Cholesterol band (associated to atherosclerotic spectrum) Glutathione	33, 131 6  94 29

(Continued on next page)

**Table 1**  
Spectral interpretations (*Continued*)

Peak (cm <sup>-1</sup> )	Assignment	Reference
1660	Amide I band	102
	Amide I	102
	Amide I vibration mode of structural proteins	94
	$\nu(\text{C}=\text{C})$ <i>cis</i> , lipids, fatty acids	64
	C=C groups in unsaturated fatty acids	71
	Ceramide backbone	71
	Amide I (protein)	122
	Lipids	122
1662	Nucleic acid modes	1
	Nucleic acid modes indicating the nucleic acid content in tissues	146
1663	DNA	110
	Proteins, including collagen I	110
1664–1665	Amide I	50
1665	Amide I (of collagen)	50
	Amide I	50
	Amide I (collagen assignment)	123
	Amide I (disordered structure-solvated)	64
	$\nu_s(\text{C}=\text{O})$	147
1666	Collagen	34
1667	Protein band	2, 3
	C=C stretching band	1
	$\alpha$ -Helical structure of amide I	20
	Structural protein modes of tumors	27
	Carbonyl stretch (C=O)	104
1669	Carbonyl stretch (C=O)	104
	Cholesterol ester	71
1670	Amide I	51
1670	C=C stretching vibrations	2
	Cholesterol and its esters	94
	C=C stretching vibration mode of steroid ring	94
	Amide I (anti-parallel $\beta$ -sheet)	64
	$\nu(\text{C}=\text{C})$ <i>trans</i> , lipids, fatty acids	64
1672	C=C stretch	121
	Amide I band (C=O stretch coupled to a N-H bending)	71
	Ceramide	71
1673	Amide I	111
1674	C=C stretch vibration	71
	Cholesterol	71
1676	Amide I ( $\beta$ -sheet)	70
1678	Bound and free NADH	76
1682	One of absorption positions for the C=O stretching vibrations of cortisone	6
1685	Amide I (disordered structure; non-hydrogen bonded)	64

(Continued on next page)

**Table 1**  
Spectral interpretations (*Continued*)

Peak (cm <sup>-1</sup> )	Assignment	Reference
1697	Amide I (turns and bands)	70
1700–1750	$\nu(\text{C}=\text{O})\text{OH}$ (amino acids aspartic and glutamic acid)	64
1710	One of absorption positions for the C=O stretching vibrations of cortisone	6
1716–1741	C=O	71
1720	Lipid	37
1725	C=O lipids	38
1729	Ester group	71
1732	One of absorption positions for the C=O stretching vibrations of cortisone	6
1734	Esters, C=O stretching (lipids)	122
1736	C=O ester (lipids)	122
1737	C=O ester (lipids)	38
1738	Lipids	3
1739	Ester group	71
1740	Ester group	71
1743, 1745	Lipid	141
1744	Carbonyl feature of lipid spectra	42
	Ester group	71
1745	Phospholipids	20
1745	$\nu(\text{C}=\text{O})$ , phospholipids (lipid assignment)	20, 126
	$\nu(\text{C}=\text{O})$ , phospholipids	131
	Triglycerides (fatty acids)	94
	$\nu(\text{C}=\text{O})$ (polysaccharides, pectin)	64
1746	C=O stretch (lipid)	31
1747	C=O, lipids	70
1750	C=O (lipid in normal tissues)	76
	$\nu(\text{C}=\text{C})$ lipids, fatty acids	64
1754	C=O (lipid)	70
1756	One of absorption positions for the C=O stretching vibrations of cortisone	6
2095	C–N stretch (one of three thiocyanate peaks, with 445 and 735 cm <sup>-1</sup> )	104
2225	C≡N	19
2300–3800	Region of the OH-NH-CH stretching vibrations	128
2343	Asymmetric stretching band of CO <sub>2</sub> <sup>-</sup> hydrates	128
2550–2580	$\nu(\text{S-H})$ (amino acid methionine)	64
2700–3300	C–H stretches	19
2700–3500	Stretching vibrations of CH, NH, and OH groups	71
2741	Stretching vibrations of CH, NH, and OH groups	38
2800–3050	Contributions from acyl chans	71
2800–3100	CH, CH <sub>2</sub> , and CH <sub>3</sub> symmetric and antisymmetric stretching	148

(*Continued on next page*)

**Table 1**  
Spectral interpretations (*Continued*)

Peak (cm <sup>-1</sup> )	Assignment	Reference
2817–2849	CH <sub>2</sub> symmetric stretch of lipids (suggests change in the amount of lipid)	113
2840–2875	CH <sub>3</sub> symmetric stretch of lipids	113
2850	$\nu_s$ CH <sub>2</sub> , lipids, fatty acids CH <sub>2</sub> symmetric	64
2850–2875	CH <sub>2</sub> symmetric stretch of lipids	113
2853–2881	CH <sub>2</sub> symmetric stretch of lipids and CH <sub>2</sub> asymmetric stretch of lipids and proteins	113
2876–2906	CH <sub>2</sub> asymmetric stretch and CH stretch of lipids and proteins	113
2876–2919	CH <sub>2</sub> asymmetric stretch of lipids and proteins	113
2879	CH <sub>2</sub> and CH of lipids and proteins	38
2883	CH <sub>2</sub> asymmetric stretch of lipids and proteins	113
2885	$\nu_s$ CH <sub>3</sub> , lipids, fatty acids	64
2886	Fermi resonance CH <sub>2</sub> stretch	71
2889–2908	CH <sub>2</sub> asymmetric stretch of lipids and proteins	113
2900	CH stretch of lipids and proteins	113
2893–2895	CH <sub>3</sub> symmetric stretch	142
2900	CH stretch	149
2910–2965	CH <sub>3</sub> stretching vibrations	55
2913–2938	CH stretch of lipids and proteins	38, 133
2915	CH band of lipids and proteins (the lipid band has a tendency towards higher levels of energy, such as 2855 cm <sup>-1</sup> , while the protein band's tendency is toward lower energy levels like 2920 cm <sup>-1</sup> )	42
2928	Symmetric CH <sub>3</sub> stretch Due primarily to protein	42 42
2929–2940	CH <sub>2</sub> asymmetric stretch	113
2933	CH <sub>2</sub> asymmetric stretch	113
2935	Chain end CH <sub>3</sub> symmetric band	71
2940	C–H vibrations in lipids and proteins $\nu_{as}$ CH <sub>2</sub> , lipids, fatty acids	52 64
2956–2957	CH <sub>3</sub> asymmetric stretch	151
2960	Out-of-plane chain end antisymmetric CH <sub>3</sub> stretch band	71
2970	$\nu_{as}$ CH <sub>3</sub> , lipids, fatty acids Cholesterol and cholesterol ester	64 71
2971, 2973	Asymmetric stretching of methoxy(4)	121
2987	cholesterol ester cholesterol ester	38
3000	CH stretching	135
3006	Bond –C–H stretch	141
3008	$\nu_{as}$ (–C–H), lipids, fatty acids	64
3010	Unsaturated =CH stretch	71

(Continued on next page)

**Table 1**  
Spectral interpretations (*Continued*)

Peak (cm <sup>-1</sup> )	Assignment	Reference
3015	$\nu$ =CH of lipids	121
3232	O-H and N-H stretching vibrations (hydrogen bonding network may vary in the malignant tissues)	142
3296	NH asymmetric stretching (proteins), amide A	28
3300	Attributed to OH stretch	71
3329	N-H vibration of proteins	55
3350–3550	OH stretching	55
3550	O-H stretching vibration	152

photon has the same frequency as the incident photon. This is known as Rayleigh or elastic scattering. When energy is transferred either from the molecule to the photon or vice versa, the scattered photon has less or more than the energy of the incident photon. This is inelastic or Raman scattering and was first observed in 1928 by Sir C. V. Raman, an Indian physicist, who received the Nobel Prize 2 years later for work in this field (18). A very small portion (1 in  $10^{10}$ ) of the light, however, is elastically scattered at a different wavelength to the incident light (19). If the photon has a higher frequency and therefore lower energy than the incident light, this is known as Stokes-Raman and is due to the change in vibrational mode of the sample molecule.

Raman spectra are a plot of scattered intensity as a function of the energy difference between the incident and scattered photons and are obtained by pointing a monochromatic laser beam at a sample. The loss (or gain) in the photon energies corresponds to the difference in the final and initial vibrational energy levels of the molecules participating in the interaction. The resultant spectra are characterized by shifts in wave numbers (inverse of wavelength in cm<sup>-1</sup>) from the incident frequency.

The frequency difference between incident and Raman-scattered light is termed the Raman shift, which is unique for individual molecules and is measured by the machine detector and is represented as 1/cm. Raman peaks are spectrally narrow and in many cases can be associated with the vibration of a particular chemical bond (or a single functional group) in the molecule (4, 20–22).

### ***Raman Spectroscopy of Biological Molecules***

A number of researchers have reported on Raman spectroscopy of biological tissues, including investigations on bone (23–25), cornea (26), cervical tissue (27–29), epithelial tissue (30–32), lung (20, 33–40), breast (21, 41–49), skin (50–61), gastrointestinal tissue (62–69), brain (70–75), oral tissue (76–82), liver (83–85), testicular (86), heme protein (87), atherosclerotic plaque (88), serum (89–93), human coronary arteries (94), lymphocytes (95), human blood cells (96–99), mixed cancer cells (100), human living cells (101), microbial cells (102), individual cells (103), saliva (104), DNA (105–108), cancer genes (109), anticancer drugs (110), tissue processing (111), Raft cultures (112), meningiomas (113), cancer field effects (114), prostate lesions (115), neuroblastoma (116), cancerous cells (to be targeted) (117), and mammalian cell cultures (118).

This article is divided into two parts. In the first part, a brief summary of the related research is presented, which provides a background for spectral data tabulated in the second part.

Huang et al. (20) reported on diagnosis of lung cancer using near-infrared (NIR) Raman spectroscopy. The objective of their study was to explore the technique for distinguishing tumor from normal bronchial tissue. A rapid acquisition dispersive-type NIR Raman spectroscopy system was used for tissue Raman studies at 785 nm. Raman spectra differed significantly between normal and malignant tumor tissues, namely, squamous cell carcinoma and adenocarcinoma. Tumors showed higher percentage signals for nucleic acids, tryptophan, and phenylalanine and lower percentage signals for phospholipids, proline, and valine in comparison with normal tissues. Raman spectral shape differences between normal and tumor tissues were also observed particularly in the region of 1000–1100, 1200–1400, and 1500–1700  $\text{cm}^{-1}$ , which contain signals related to protein and lipid conformations and nucleic acids' CH stretching modes. The ratio of Raman intensities at 1445–1655  $\text{cm}^{-1}$  provided good differentiation between normal and malignant bronchial tissue ( $p < 0.0001$ ). The results of this exploratory study indicated that NIR Raman spectroscopy provides significant potential for noninvasive diagnosis of lung cancer in vivo based on the optic evaluation of biomolecules.

Shafer-Peltier et al. (21) reported on a Raman spectroscopic model of human breast tissue and its implications for breast cancer diagnosis in vivo. They believed that Raman spectroscopy has the potential to provide real-time, in situ diagnosis of breast cancer during needle biopsy or surgery via an optical fiber probe. To understand the relationship between the Raman spectrum of a sample of breast tissue and its disease state, NIR Raman spectroscopic images of human breast tissue were acquired using a confocal microscope. These images were then compared with phase contrast and hematoxylin- and eosin-stained images to develop a chemical/morphological model of breast tissue Raman spectra. The model explained the spectral features of a range of normal and diseased breast tissue samples, including breast cancer, and it also could be used to relate the Raman spectrum of a breast tissue sample to diagnostic parameters used by pathologists.

McManus et al. (24) reported that Raman spectroscopy could be used as a molecular detective to understand the crystallinity and bone quality from human primary osteoblasts and osteoblast-like cells. The spectra of both cell lines have shown amide I (1655  $\text{cm}^{-1}$ ), amide III (1248  $\text{cm}^{-1}$ ), C–N stretching (720  $\text{cm}^{-1}$ ), CH bending (985 and 1319  $\text{cm}^{-1}$ ), CH deformation (1448  $\text{cm}^{-1}$ ), and O–P–O stretch (788  $\text{cm}^{-1}$ ) vibrations. Osteoblast-like cells have explicitly shown tyrosine ring breathing (826  $\text{cm}^{-1}$ ) and O–P–O asymmetric stretching (857  $\text{cm}^{-1}$ ) vibrations. Nucleic acid (DNA/RNA) and O–P–O are higher intensities in osteoblast-like cells compared to primary osteoblasts. After 28 days of culture, Raman spectra of osteoblast-like cells have shown mineralizing features and peaks associated with this are at 1246–1269  $\text{cm}^{-1}$  (amide III) and 1595–1720  $\text{cm}^{-1}$  (amide I). Furthermore, the appearance of PO stretch at 960  $\text{cm}^{-1}$  denotes the inclusion of hydroxyapatite in the extracellular matrix. A combination of univariate peak analysis and principal component analysis (PCA) has proved that osteoblast-like cells have analogous features like bone as well as primary osteoblasts in terms of carbonate-to-phosphate ratio, mineral-to-matrix ratio, and crystallinity. This study has contradicted previous studies and explored Raman as a decisive tool for identifying compositional differences between the osteoblast-like cell lines and primary osteoblasts.

Nyman et al. (25) reported that confocal Raman spectroscopy could be used in quantifying differences in compositional properties of osteonal and interstitial bone tissues. This study is based on the hypothesis that collagen peaks are least affected by the

orientation of bone tissue and demonstrates statistically significant differences in bone composition, namely, the mineral-to-collagen ratio, between osteonal and interstitial tissue. Raman spectra were acquired from the polished surface of the bone tissue with a 785-nm laser diode source with a spectral resolution of  $1\text{ cm}^{-1}$ . Raw peak intensities using custom developed software were obtained, and the intensities were calculated for  $\nu_1$  phosphate at  $960\text{--}962\text{ cm}^{-1}$  ( $\nu_1\text{PO}_4$ ),  $\nu_2$  phosphate at  $431\text{--}433\text{ cm}^{-1}$  ( $\nu_2\text{PO}_4$ ),  $\nu_4$  phosphate at  $584\text{--}589\text{ cm}^{-1}$  ( $\nu_4\text{PO}_4$ ), type B carbonate at  $1071\text{--}1072\text{ cm}^{-1}$  (Carb), proline at  $855\text{--}857\text{ cm}^{-1}$ , amide III at  $1247\text{--}1248\text{ cm}^{-1}$ ,  $\text{CH}_2$ -wag at  $1451\text{--}1452\text{ cm}^{-1}$ , and amide I at  $1666\text{--}1667\text{ cm}^{-1}$ . They also calculated 15 peak ratios such as  $\nu_1\text{PO}_4/\text{amide I}$ ,  $\nu_2\text{PO}_4/\text{amide III}$ ,  $\nu_4\text{PO}_4/\text{proline}$ ,  $\nu_1\text{PO}_4/\text{CH}_2\text{-wag}$  and  $\text{Carb}/\nu_4\text{PO}_4$ ; furthermore, the inverse of the full width of the  $\nu_1\text{PO}_4$  peak at half-max ( $\nu_1\text{FWHM-1}$ ) wherein the maximum intensity was normalized. Results have illustrated peak ratios of m1 phosphate ( $\text{PO}_4$ ) to proline and m1 phosphate ( $\text{PO}_4$ ) to amide III calculated to increase from 15.4 or 12.5%, respectively, in composition from osteonal to interstitial tissue. The coefficient of variance was below 5% for each as opposed to a value of 8% for the traditional  $\nu_1\text{PO}_4/\text{amide I}$  a peak ratio, which was more varied between transverse and longitudinal cuts of each tissue type. Raman peaks were affected by embedding and it also cannot obscure modifications in peak ratios that are related to mineralization between two different tissue types. Further studies with limited sample size but a greater number of Raman spectra are most likely to detect a compositional differences among samples; the number of Raman spectra per specimen must be sufficient to attain spatial averaging  $\nu_1\text{PO}_4/\text{amide III}$  or  $\nu_1\text{PO}_4/\text{proline}$ . The  $\nu_1\text{PO}_4/\text{proline}$  and  $\nu_1\text{PO}_4/\text{amide III}$  ratios basically illustrate the mineral-to-matrix ratio of bone tissue; the ratio is related to the degree of mineralization in the matrix over time. The higher variance in  $\nu_1\text{PO}_4/\text{amide I}$  ratio might suggest that amide I intensity is dependent on orientation of both collagen fibrils and incident laser light polarization.

Uttinger et al. (27) introduced an NIR Raman spectroscopic method for in vivo detection of cervical precancers. The main focus of the project was on squamous dysplasia, a precursor of cervical cancer. A pilot clinical trial was carried out at three clinical sites. Raman spectra were measured from one normal and one abnormal area of the cervix. These sites were then biopsied and submitted for routine histologic analysis. Twenty-four measurements were made in vivo in 13 patients. Cervical tissue Raman spectra contained peaks in the vicinity of 1070, 1180, 1195, 1210, 1245, 1330, 1400, 1454, 1505, 1555, 1656, and  $1760\text{ cm}^{-1}$ . The ratio of intensities at  $1454\text{--}1656\text{ cm}^{-1}$  is greater for squamous dysplasia than all other tissue types, and the ratio of intensities at  $1330\text{--}1454\text{ cm}^{-1}$  is lower for samples with squamous dysplasia than all other tissue types. A simple algorithm based on these two intensity ratios separated high-grade squamous dysplasia, misclassifying only one sample. Spectra measured in vivo resembled those measured in vitro. It was believed that cervical epithelial cells might contribute to tissue spectra at  $1330\text{ cm}^{-1}$ , a region associated with DNA. In contrast, epithelial cells probably do not contribute to spectra at  $1454\text{ cm}^{-1}$ , a region associated with collagen and phospholipids.

Kamemoto et al. (28) used NIR Raman spectroscopy as molecular marker detective to discriminate between normal and invasive cervical cancer tissue samples. This study has concentrated on the final stage of invasive carcinoma and collected 14 tissue samples from four healthy individuals with no cervical cancer record and three patients with cervical squamous cell carcinoma. The wavelength of the laser used was 785 nm to excite both normal and cancer cells. The spectrum of normal squamous cells has shown good amounts of  $\delta$  (CCH) aliphatic of collagen ( $816\text{ cm}^{-1}$ ), ring breathing in tyrosine and CCH deformation ( $854\text{ cm}^{-1}$ ), C-C stretch ( $922\text{ cm}^{-1}$ ), C-C skeletal stretch ( $938\text{ cm}^{-1}$ ), phenylalanine (Phe) and C=H in-plane bending ( $1003\text{ cm}^{-1}$ ), O-P-O backbone stretch

of DNA ( $1101\text{ cm}^{-1}$ ), amide III ( $1247\text{ cm}^{-1}$ ),  $\delta$  (C=CH) ( $1273\text{ cm}^{-1}$ ),  $\text{CH}_2$  deformation of lipids ( $1321, 1450\text{ cm}^{-1}$ ), DNA ( $1342\text{ cm}^{-1}$ ), and  $\alpha$ -helix of amide I ( $1664\text{ cm}^{-1}$ ). The outcome of this work has shown two specific differences between normal and malignant cells. Firstly, several well-defined Raman peaks of collagen ( $775\text{--}975\text{ cm}^{-1}$ ) were observed in normal squamous cells, but these were absent in invasive cancer cells. Secondly, the amide III ( $1248\text{ cm}^{-1}$ ) was present in normal cells, whereas it was absent in cancer cells. This investigation also revealed that the C=H stretching mode ( $2800\text{--}3100\text{ cm}^{-1}$ ) is six times lower in the factor in cancer cells compared to normal cells.

Gonzalez-Solis et al. (29) reported the detection of cervical cancer by investigating blood samples with Raman spectroscopy and multivariate analysis. In this study, serum was obtained from fresh blood samples from 20 patients and 10 healthy volunteers and 240 spectra was collected from these samples. Of these, 80 spectra were collected from 10 control patients, 160 spectra from 10 cervical cancer, and 10 spectra from early cervical cancer patients. PCA and linear discrimination analysis (LDA) were performed after removing the fluorescence contribution, smoothing, and the baseline correction. Raman spectra have shown clear evidence in peak intensities between normal and cervical cancer states. The peaks of phenylalanine ( $1002\text{ cm}^{-1}$ ) and  $\beta$ -carotenes ( $1154, 1523\text{ cm}^{-1}$ ) of the cervical spectrum are higher than the peaks of the control spectrum. This study also found that peaks at  $898, 1615\text{ cm}^{-1}$  (adenine),  $1080, 1313\text{ cm}^{-1}$  (tryptophan),  $1449\text{ cm}^{-1}$  ( $\beta$ -sheet and phospholipids),  $1547\text{ cm}^{-1}$  (proline),  $1659\text{ cm}^{-1}$  (glutathione),  $1396\text{ cm}^{-1}$  ( $\beta$ -carotene), and  $1765\text{ cm}^{-1}$  were present only in the spectrum of cancer cells, whereas the peaks at  $1266\text{ cm}^{-1}$  (amide III) and  $1722\text{ cm}^{-1}$  were present only in the control spectrum. This study has allowed biological molecule like adenine, tryptophan, proline, glutathione, and  $\beta$ -carotene to be used to discriminate between normal and cancerous samples.

Stone et al. (30) applied NIR Raman spectroscopy for the classification of epithelial cancers and precancers. The aim of their research was to evaluate the use of the technique in interrogating epithelial tissue biochemistry and distinguishing between normal and abnormal tissues. Tissues were selected for clinical significance and to include those that develop into carcinoma from squamous, transitional, or columnar epithelial cells. Rigorous histopathological protocols were followed. The epithelial tissues were obtained from larynx, tonsil, esophagus, stomach, bladder, and prostate. Sensitivities and specificities of up to 100% in separating the samples were obtained.

The same research group performed Raman spectroscopic investigations for identification of epithelial cancer (31). They evaluated the potential for the technique to develop a noninvasive real-time probe for accurate and repeatable measurement of pathological samples. The study followed rigorous sample collection protocols and histopathological analysis using a board of expert pathologists. Only the data from samples with full agreement of a homogeneous pathology were used to construct a training data set of Raman spectra. Measurements of tissue specimens from the full spectrum of different pathological groups found in each tissue were made. Diagnostic predictive models were constructed and optimized. High levels of discrimination between pathology groups were demonstrated (greater than 90% sensitivity and specificity for all tissues). However, it was outlined that larger sample numbers are required for successful implementation of in vivo Raman detection of early malignancies.

Keller et al. (32) employed Raman microspectroscopy (RMS) for discriminating normal cervixes of healthy patients versus those of patients with previous disease history. Cervical mapping study of in vitro epithelium and stroma showed spectral signatures for samples containing disease only in epithelial layers. Raman peaks at  $1250$  and  $1400\text{ cm}^{-1}$

were found consistently different between health cervixes, previously diagnosed abnormal cervixes, and cervixes with no history of disease. The peak at  $1250\text{ cm}^{-1}$  is associated with collagen; hence, the spectral difference could be due to a small amount of collagenous tissue left at the previous disease area. Overall accuracy for determining disease was greater than 99%. Raman can also differentiate normal and diseased tissues and the band intensities were increased at  $1334$  and  $1082\text{ cm}^{-1}$  due to the DNA content of the cells. An increase amount of DNA in diseased tissues suggests enhanced proliferation. Peak intensities of the band in the regions from  $1000$  to  $1100\text{ cm}^{-1}$  and from  $1250$  to  $1350\text{ cm}^{-1}$  are higher in normal tissue. Some of these peak differences are associated with glycogen and were reported at  $1048$ ,  $1083$ ,  $1256$ , and  $1333\text{ cm}^{-1}$ . It is known that the glycogen in epithelia decreases with disease, but there is no mention of what happens in the stroma as a result of disease in the epithelium. This study has demonstrated that Raman spectroscopy as a diagnostic tool to detect subtle tissue changes and to identify disease markers associated with cervical cancer.

Min et al. (33) reported on NIR  $1,064\text{-nm}$  multichannel Raman spectroscopy of fresh human lung tissues. Excitation at  $785\text{ nm}$  failed to detect any Raman bands because of an extremely high fluorescence backbone. As a result, it was confirmed that  $1,064\text{ nm}$  excitation was a requisite for the Raman study of the fresh lung tissue. The observed Raman spectra of lung tissues made a clear distinction between the normal and cancerous states. It was demonstrated that  $1,064\text{ nm}$  NIR multichannel Raman spectroscopy is a feasible tool for in vivo, noninvasive, and molecular-level clinical diagnosis of diseases including cancer.

Kaminaka et al. (34) investigated the possibility of molecular-level cancer diagnosis of human lung tissues using NIR Raman spectroscopy. They used a  $1,064\text{-nm}$  Nd:YAG laser and could collect totally fluorescence-free Raman spectra of normal and cancerous lung tissues. It was concluded that the technique probed lung cancer unambiguously at the molecular level and could be used as a tool for cancer diagnosis.

Huang et al. (35) employed NIR Raman spectroscopy to study the effect of formalin fixation of normal and cancerous human bronchial tissues. The aim of the study was to determine whether the variations of the Raman spectra caused by formalin fixation would affect the potential diagnostic ability for the lung cancer detection. A rapid dispersive-type NIR Raman system with an excitation wavelength of  $785\text{ nm}$  was used. Bronchial tissue samples were obtained from six patients with known or suspected malignancies of the lung. Raman spectra of fresh normal and tumor tissue were compared with spectra of formalin-fixed normal and tumor tissue. Changes in the ratios of Raman intensities at  $1445\text{--}1655$  and  $1302\text{--}1265\text{ cm}^{-1}$  versus formalin fixing times varying from 2 to 24 h were also examined. The major Raman spectral peaks were found at  $1265$ ,  $1302$ ,  $1445$ , and  $1655\text{ cm}^{-1}$  in both fresh and fixed bronchial tissues. However, bronchial tissues preserved in formalin showed a progressive decrease in overall intensities of these Raman peaks. The results showed that NIR Raman spectra of human bronchial tissues were significantly affected by formalin fixing and tissue hydration. Diagnostic markers at the  $980\text{--}1100$  and  $1500\text{--}1650\text{ cm}^{-1}$  regions derived from fixed tissues did not appear to be applicable for in vivo lung cancer detection. It was shown that to yield valid Raman diagnostic information for in vivo applications, fresh tissue should be used; if only fixed tissue is available, thorough rinsing of specimens in phosphate-buffered saline before spectral measurements may help reduce the formalin fixation artefacts on tissue Raman spectra.

Oshima et al. (36) applied Raman spectroscopy to demonstrate differences among cultures of normal and cancerous lung cell lines. This study has used four different types of lung cancer cell lines, namely, adenocarcinoma and squamous cell carcinoma with low to medium malignancy and small cell carcinoma and large cell carcinoma with high

malignancy. Single-cell Raman spectra were obtained by using 532-nm excitation wavelength instead of 785 or 633 nm. High-quality spectra were obtained at 60 s/cell without any damage. The purpose of this study is to find diagnosis through a suitable Raman marker for lung cancer cell lines and their malignancy. The spectra have shown strong band for cyc-c and laser has contributed much resonance in the spectra. PCA was successfully applied and 80% accuracy was achieved in discrimination between cancer lines. Stepwise LDA was performed on these cell lines to identify malignancy type and strain. Cross-validation provided 100% accuracy of discrimination. The current study has shown the potential of a 532-nm laser in Raman diagnosis.

Li et al. (37) employed surface-enhanced Raman spectroscopy (SERS) to detect biofluids at the molecular level, so that prediction of lung cancer can be possible at early stages. SERS was performed on saliva samples to detect vibrational features of the lung cancer pathology. Raman spectra of control and cancerous sample have shown peaks at  $791\text{ cm}^{-1}$  (pyrimidine),  $906\text{ cm}^{-1}$  (tyrosine),  $1007\text{ cm}^{-1}$  (phenylalanine and carbamide),  $1364\text{ cm}^{-1}$  (tryptophan), and  $1720\text{ cm}^{-1}$  (lipid). Only minute differences such as peak intensities were found between the both spectra. This group has used multivariate analysis such as PCA to extract the main factors and then LDA for discrimination between both groups. PCA and LDA were successfully employed and 82% total accuracy was achieved. This study has shown the promising approach of SERS in detection of lung cancer.

Huang et al. (38) described applications of Raman spectroscopy in their review article to chemically characterize different organs of mice. This group has reported no spectral differences between blood pellets and blood. The major Raman vibrations were observed in this study were DNA, tryptophan, phosphatidylinositol, red blood cell (RBC), NADH, phenylalanine, triglycerides, glucose, collagen, tyrosine, amide II, carotene, C—C or C—N stretching of proteins,  $\text{CH}_3/\text{CH}_2$  wagging, and  $\text{CH}_3$ ,  $\text{CH}_2$  of lipids and proteins. Further studies have demonstrated that Raman bands at  $1375$ ,  $1590$ , and  $1640\text{ cm}^{-1}$  have increased during oxygen saturation. A whole-blood spectrum showed a pointed peak at  $2330\text{ cm}^{-1}$  due to high atmospheric nitrogen and high laser intensity. The spectra of serum showed vibrations regarding protein, proline,  $\text{CH}_3/\text{CH}_2$  wagging, collagen,  $\text{CH}_3$ , fatty acids,  $\text{CH}_2$ , RBC, and amide I. Proline and amide I were observed in the serum spectrum but not in the whole-blood spectrum.

Huang et al. (38) further reported on Raman studies of adipocytes, muscle, and skin. Adipocytes showed predominant bands of palmitic acid, amide I, C55O ester, cholesterol, cholesterol ester, C—C, CH, and  $\text{CH}_2$  stretch of lipids. This spectrum resembled the palmitic acid spectrum, which is one of the most frequent saturated fatty acids present in the animal kingdom. Furthermore, these spectra showed a close resemblance with other saturated fatty acids, such as lauric and myristic acid. Muscle cells have glycogen as reserve sources for energy and Raman was applied for the first time on human muscle cells. The spectra of muscle cells were dominated by tyrosine, proline, amide III, cholesterol, and cholesterol esters. Raman spectra of skin showed peak intensities corresponding to palmitic acid, adenine, cytosine, amides I, II, and III, and  $\text{CH}_2$  and CH of lipids and proteins. The spectrum of skin showed high similarity to adipose cells due to the same composition of fat and proteins.

Huang et al.'s review article (38) reported Raman fingerprinting of the gastrointestinal tract such as the stomach, intestine, and colon. Raman bands of stomach tissue demonstrated the presence of tyrosine, DNA, polysaccharides, NADH, proline, and amide III. This group further reported Raman studies in the gastrointestinal tract including the stomach, small intestine, and colon. The characteristic Raman peaks of normal stomach tissue were

observed at 828, 851, 991, 1044, 1258, 1302, 1442, 1653, 1725, 2139, 2177, and 2917  $\text{cm}^{-1}$ ; there is no study reported in the literature on Raman spectra of the stomach in the high-frequency region. The characteristic Raman peaks of normal small intestine tissue were observed at 828, 921, 991, 1044, 1074, 1160, 1258, 1302, 1335, 1442, 1542, 1653, 1725, 2139, 2177, 2870, and 2917  $\text{cm}^{-1}$ ; there are currently no studies in the literature regarding the intestine. The Raman spectra of normal colorectal tissue showed prominent bands at 1080, 1260, 1300, 1450, 1650, and 1750  $\text{cm}^{-1}$ . The gastrointestinal tract showed similar peaks at 828, 1258, 1302, 1442, 1653, 1725, 2136, 2169, and 2917  $\text{cm}^{-1}$ . These peaks have revealed interesting features of chemical fingerprint of gastrointestinal tract. The peaks at 828 and 1258  $\text{cm}^{-1}$ ; 1302, 1442, 1653, and 2917  $\text{cm}^{-1}$ ; and 1725, 2136, and 2169  $\text{cm}^{-1}$  appeared due to protein and DNA, lipids and proteins, and lipids and water, respectively.

This study (38) has also covered Raman progress in the urinary bladder, lung, and brain. The spectrum of urinary bladder was similar to the gastrointestinal tract. The characteristic Raman peaks were observed at 828, 991, 1044, 1258, 1302, 1442, 1542, 1614, 1653, 1725, 2139, and 2917  $\text{cm}^{-1}$ . The spectra of both organs showed similar intensities at 828, 991, 1044, 1442, 1653, 1725, 2139, and 2917  $\text{cm}^{-1}$ . The Raman spectra of the bladder showed weaker intensities at 1258, 1302, and 1542  $\text{cm}^{-1}$  than the gastrointestinal tract. The spectral similarities were observed due to common structure of the intestinal wall in both organs. The prominent Raman bands of lung were reported at 800, 991, 1044, 1302, 1335, 1442, 1542, 1590, 1614, 1653, 1725, 2139, and 2917  $\text{cm}^{-1}$ . A strong peak at 1590  $\text{cm}^{-1}$  was observed in the lung spectra, but it is not clear why. The Raman spectra of the brain showed characteristic peaks at 962, 991, 1044, 1302, 1442, 1542, 1614, 1653, 1725, 2139, 2879, and 2917  $\text{cm}^{-1}$ . In the spectrum of brain tissue a prominent peak was observed at 2879  $\text{cm}^{-1}$ , which also appeared in skin and adipose tissue due to lipids and proteins. This peak is believed to be originated from lipids because lipids are so abundant in brain tissue.

Nawaz et al. (39) reported that confocal RMS could be used to study the efficacy of the chemotherapeutic agent cisplatin on A549 adenocarcinoma cells. The aim of this study is to explore chemical changes in cell membranes and cytoplasm of A549 cells after 96 h of exposure to cisplatin. Multiple spectra were obtained from different regions of the cell, including the cell membrane, cytoplasm, and nucleus. The spectral data was used to analyze the difference in cellular components and peak changes after cisplatin treatment and multivariate analysis techniques like PCA, partial least squares regression (PLSR), and PLS jack-knifing were used. This study has identified a band at 726  $\text{cm}^{-1}$  that represented tryptophan as well as  $\text{CH}_3$  stretching of lipids present in a cytoplasm spectrum but not in a nuclear spectrum. Similarly, the Raman peaks at 1423 and 1510  $\text{cm}^{-1}$  were assigned to  $\text{CH}_3$  deformation of aromatic lipids and  $\text{C}=\text{C}$  stretching of tryptophan and tyrosine, respectively. These bands were observed predominately in cell membranes and cytoplasm spectra rather than in nuclear membrane mean spectra. The effect of cisplatin on the cell membrane spectra revealed the appearance of protein-related peaks at 671 and 728  $\text{cm}^{-1}$  (ring breathing of the tryptophan), 1030  $\text{cm}^{-1}$  ( $\text{C}-\text{H}$  bending), 1094 and 1126  $\text{cm}^{-1}$  ( $\text{C}-\text{N}$  stretching), and 1655  $\text{cm}^{-1}$  (amide I). The Raman bands at 1371  $\text{cm}^{-1}$  ( $\text{CH}_3$  stretching) and 1448  $\text{cm}^{-1}$  ( $\text{CH}$  deformation) are related to cell membrane lipids and significant peak shifts were observed at 1371–1376  $\text{cm}^{-1}$  and 1488–1450  $\text{cm}^{-1}$ . They also extracted protein from control and treated cisplatin cells and analyzed the spectral differences. This group has reported major changes in the Raman bands include an intensification of the 904 and 1131  $\text{cm}^{-1}$  ( $\text{C}-\text{C}$  skeletal stretching), 1001  $\text{cm}^{-1}$  (phenylalanine), 1061  $\text{cm}^{-1}$  ( $\text{C}-\text{N}$  stretching), 1131 and 639  $\text{cm}^{-1}$  (tyrosine ring breathing), 961 and 1199  $\text{cm}^{-1}$ , 1011  $\text{cm}^{-1}$  (tryptophan ring breathing), 1323 and 1404  $\text{cm}^{-1}$  ( $\text{CH}$  deformation), and 1606  $\text{cm}^{-1}$  ( $\text{C}=\text{C}$

bending). PLS jack-knifing analysis of cell membranes has demonstrated that cisplatin seems interacted with membrane lipids and caused some changes in their structure. Jack-knifing results for cytoplasm suggested that changes in cell physiology in term of ring breathing of tryptophan, RNA, and CH bending were observed due to cisplatin's action.

Magee et al. (40) demonstrated that a mini-fiber optic probe coupled with shifted subtracted Raman spectroscopy could be used to distinguish between *ex vivo* normal and malignant lung tissue. A mini Raman probe was specifically designed for the purpose of working in the channel of bronchoscope and SSRS was specifically designed to reduce fluorescence. Seven patients undergoing lung resection for non-small lung cancer participated in this study. The Raman peak intensities at  $1070\text{ cm}^{-1}$  (C–C or C–N or C–O) and  $1300$  and  $1445\text{ cm}^{-1}$  (collagen and phospholipids) were higher in healthy tissues, whereas the peaks at  $855, 920, 935, 1002\text{ cm}^{-1}$  (phenylalanine),  $1260\text{ cm}^{-1}$  (amide III), and  $1665\text{ cm}^{-1}$  (amide I) exhibited higher intensity in the tumor spectra. Spectral data were analyzed using PCA with leave-one-out cross-validation. Principal component 5 has separated normal spectra from cancerous precisely to 100% with a cutoff score of 0.1. This study was done *ex vivo* but has shown great potential for Raman spectroscopy as a real-time diagnostic tool. A larger and independent database containing a set of spectra from malignant and normal tissue in the clinical setting is required to validate this model.

Kline and Treado (42) reported on chemical imaging of breast tissue using Raman spectroscopy. Raman chemical imaging of lipid and protein distribution in the breast was performed without the use of invasive contrast agents. Instead, tissue component discrimination was based on the unique vibrational spectra intrinsic to lipids and proteins. It was suggested that visualization of breast tissue components is an essential step in the development of a quantitative Raman optical biopsy technique suitable for the noninvasive detection and classification of breast cancer.

Tam et al. (43) carried out a study on sample processing techniques of breast cancer using Raman spectroscopy. Fifty breast biopsies were studied using Raman spectroscopy prior to receipt of pathology reports. This was applied to at least two of the three available tissue processing techniques using point spectroscopy, mapping, and imaging. Differences in the spectra were related to the various sample processing methods.

Haka et al. (44) employed Raman spectroscopy to diagnose benign and malignant lesions in human breast tissue based on chemical composition. This study used a microspectroscopic model of breast tissue that was built upon nine basis spectra. The basis spectra represent the epithelial cell cytoplasm, cell nucleus, fat,  $\beta$ -carotene, collagen, calcium hydroxyapatite, calcium oxalate dihydrate, cholesterol-like lipid deposits, and water. This group has developed a diagnostic algorithm for pathological diagnosis with 94% sensitivity and 96% specificity. This study has shown the potential of Raman spectroscopy in *in vivo* studies to accurately classify breast lesions, thereby reducing number of biopsies.

Rehman et al. (45) used Raman spectroscopy to examine the biochemical changes taking place within the breast. Spectra of the normal breast tissue were compared with those of malignant tissue. Raman was used to identify chemical changes in different grades of ductal carcinoma in situ (DCIS) (low nuclear grade, intermediate nuclear grade, and high nuclear grade) and Invasive ductal carcinoma (IDC; grade I, grade II, and grade III) were analyzed using Raman spectroscopy. The Raman spectra of normal breast tissue showed a peak at  $1662\text{ cm}^{-1}$  due to amide I group of proteins. The band's intensity varies with the degree of fatty acid unsaturation and it depends mainly on the lipid to protein ratio. The peak reported at  $1442\text{ cm}^{-1}$  represents protein assignment of  $\text{CH}_2$  and  $\nu_{\text{as}}\text{CH}_3$  of collagen or a lipid assignment attributed to  $\nu_{\text{as}}\text{CH}_2$ , scissoring, phospholipids and is of diagnostic significance. The normal tissue has shown weaker intensity than that of IDC tissue in Raman

spectrum, and with increasing grades the intensity of peaks increases; that is, grade I with a minimum intensity, grade II in between, and grade III at the maximum. The increase in intensity of the OH-NH-CH peaks suggests a change in the lipids, proteins, and DNA contents. The absolute intensity of each of the OH-NH-CH peaks in the 3500–2700  $\text{cm}^{-1}$  region varies with increasing grade (I, II, and III), indicating varying concentrations of fatty acyl chains, phospholipids, cholesterol, creatine, proteins, and nucleic acids. There were obvious spectroscopic differences found between the three DCIS grades in both the relative and absolute intensities of absorption bands in the spectra. The spectra from high nuclear grade is rich in lipid/acylglycerides, the spectra from low nuclear grade is protein rich, and the spectra from intermediate nuclear grade contains significant amounts of both lipids/acylglycerides and proteins.

Haka et al. (46) examined *in vitro* fresh-frozen tissues involving four types of tissue, including normal breast tissue, fibrocystic change, fibroadenoma, and invasive carcinoma taken from 126 sites of 58 patients. In order to extract information from the Raman spectra, a spectroscopic model was employed. The modeling of the Raman spectrum included fit coefficients that reflect the chemical makeup of the lesion, which was in turn linked with morphological changes that pathologists routinely rely on to diagnose breast cancer. The resulting diagnostic algorithm, which classifies tissues not even as benign or malignant but also according to pathological diagnoses, attained a sensitivity of 94%, specificity of 96%, and a total test efficiency of 95% for the diagnosis. In their study, Raman spectra were recorded using an 830-nm diode laser with spectral resolution of 8  $\text{cm}^{-1}$ . The diagnostic algorithm, which was developed earlier, was then applied prospectively to get the Raman spectral diagnoses, which were further compared to traditional histopathology diagnoses. This group has developed an algorithm based on the fit coefficients for fat and collagen. The current algorithm has diagnosed 5 out of 20 DCIS specimen as cancerous, and the remaining 15 DCIS specimens were identified as noncancerous, which includes seven fibrocystic change, seven normal breast tissue, and one fibroadenoma. This study included spectra recorded from patients who had undergone preoperative chemotherapy. All of these spectra were incorrectly diagnosed by this algorithm. It is clear that other fit coefficients must be incorporated into the algorithm to correctly diagnose DCIS. Studies are presently in progress to expand the diagnostic algorithm to incorporate DCIS.

Saha et al. (47) applied Raman spectroscopy for detecting microcalcifications in breast tissue based on their chemical composition. Raman spectra were acquired from tissue samples collected through core needle breast biopsy procedures. The algorithm developed to identify microcalcifications was based on model fit coefficients for total calcium, collagen, and fat. The spectra of breast biopsies were characterized by the presence of Raman peaks at 912 and 1477  $\text{cm}^{-1}$  (calcium oxalate) and 960  $\text{cm}^{-1}$  (calcium hydroxyapatite). This group has detected microcalcifications up to 2,150  $\mu\text{m}$  depth in the breast biopsies, whereas previous studies were reported maximum transmission depth of only 1 mm (1,000  $\mu\text{m}$ ). This algorithm has a positive predictive value of 97%, a negative predicted value of 85%, and sensitivity of 86% for detection of microcalcifications; this study not only identified microcalcifications but also distinguished type I microcalcifications from type II.

Abramczyk et al. (48, 49) applied Raman imaging to distinguish between normal and cancerous breast tissue. The main aim of this study was not only to avoid histological studies based on biopsies, which are often prone to subjective interpretations, but also improve biochemical analysis of vibrational properties of tissue. Optical fiber catheters coupled to a micro-Raman spectrometer were used in this study. The Raman images showed clear differences in carotenoids and fatty acid composition and products of their metabolism between cancerous tissue and surrounding noncancerous tissue. Spectral data

confirmed that noncancerous tissue is almost identical to monosaturated oleic acid, which is a common component of triglycerides and adipose tissue, whereas cancerous tissue is likely to be dominated by arachidonic acid derivatives, mainly cyclic eicosanoids catalyzed by cyclooxygenase. This study suggested that carotenoids and lipids can be used as Raman biomarkers in breast cancer pathology.

Cheng et al. (50) reported on micro-Raman spectroscopy used to identify and grade human skin pilomatrixoma (PMX). The normal skin dermis, collagen type I, and hydroxyapatite (HA) were used as controls. The Raman spectrum of normal skin dermis was found to be similar to that of collagen type I, confirming that the collagen was a predominant component in normal skin dermis. The most significant differences in the collected spectra of normal skin dermis and soft and hard PMX were the peaks at  $1665\text{ cm}^{-1}$ , which is assigned to the amide I band, and  $1246\text{ cm}^{-1}$ , which is assigned to the amide III band. The considerable changes in collagen content and its structural conformation, the higher content of tryptophan, and disulfide formation in PMX masses were markedly evidenced. In addition, the peak at  $960\text{ cm}^{-1}$  assigned to the stretching vibration of  $\text{PO}_4^{3-}$  HA appeared in the Raman spectra of hard and soft PMX masses, suggesting the occurrence of calcification of HA in the PMX tissue. The results indicated that the micro-Raman spectroscopy may provide a highly sensitive and specific method for identifying normal skin dermis and how it differs in chemical composition from different PMX tissues.

Kaminaka et al. (51) reported on NIR multichannel Raman spectroscopy for real-time in vivo cancer diagnosis. The method enabled them to measure an in vivo Raman spectrum of live human tissue (skin) in one minute using fiber probe optics. By applying the system to human lung tissue, they found that Raman spectroscopy makes a clear distinction not only between normal and cancerous tissues but also between two different parts of lung carcinoma. The results indicated a promising future for the noninvasive real-time Raman diagnosis of cancer.

Sigurdsson et al. (52) studied the detection of skin cancer by classification of Raman spectra. The classification framework was probabilistic and highly automated. Correct classification of  $80.5 \pm 5.3\%$  for malignant melanoma and  $95.8 \pm 2.7\%$  for basal cell carcinoma was reported, which is excellent and similar to that of trained dermatologists. The results were shown to be reproducible and small distinctive bands in the spectrum, corresponding to specific lipids and proteins, were also shown to hold discriminating information used to diagnose skin lesions.

Diagnosis of the most common skin cancer, basal cell carcinoma (BCC), by Raman spectroscopy was carried out by Gniadecka et al. (53). Biopsies of histopathologically verified BCC and normal skin were harvested and analyzed by NIR-Fourier transform (FT) Raman spectroscopy using a 1,064-nm Nd:YAG laser as a radiation source. The results indicated alterations in proteins and lipids structure in skin cancer samples. Spectral changes were observed in protein bands, amide I ( $1640\text{--}1680\text{ cm}^{-1}$ ), amide III ( $1220\text{--}1300\text{ cm}^{-1}$ ), and  $\nu(\text{C}\text{--}\text{C})$  stretching (probably in amino acids proline and valine,  $928\text{--}940\text{ cm}^{-1}$ ) and in bands characteristic of lipids,  $\text{CH}_2$  scissoring vibration ( $1420\text{--}1450\text{ cm}^{-1}$ ), and  $-(\text{CH}_2)_n$ -in-phase twist vibration around  $1300\text{ cm}^{-1}$ . Moreover, possible changes in polysaccharide structure were found in the region  $840\text{--}860\text{ cm}^{-1}$ . Analysis of band intensities in the regions of  $1220\text{--}1360$ ,  $900\text{--}990$ , and  $830\text{--}900\text{ cm}^{-1}$  allowed for a complete separation between BCC and normal skin spectra. In conclusion, Raman spectra of BCC differed considerably from those of normal skin and the technique can be viewed as a promising tool for the diagnosis of skin cancer.

A study on confocal RMS as a noninvasive in vivo optical method to measure molecular concentration profiles in the skin was carried out by Caspers et al. (55). It was shown that the

technique can be applied to determine the water concentration in the stratum corneum as a function of distance to the skin surface, with a depth resolution of  $5\ \mu\text{m}$ . The resulting in vivo concentration profiles were in qualitative and quantitative agreement with published data. No other noninvasive in vivo technique exists for analysis of skin molecular compositions as a function distance to the skin surface with similar detail and spatial resolution.

Larraona-puy et al. (56) have employed RMS in order to access its accuracy in detection and imaging BCC. This automated evaluation was carried out on skin tissues excised during Mohs micrographic surgery and skin surgery. A spectral database was developed using 329 tissue regions from 20 patients and it was used to construct the multivariate classification model. The model has classified the spectra of BCC, dermis, and epidermis. Collagen type I spectral features mainly contributed to differentiate between dermis and BCC. On the other hand, DNA peaks provided evidence in discrimination of BCC from epidermis. Healthy dermis was characterized by proline and C—C backbone vibrations of proteins. This study has shown high sensitivity and specificity in discrimination of normal healthy tissue from BCC. Moreover, this approach has developed two-dimensional biochemical images using supervised models, which further supported the positive and strong correlation with histopathological detection.

Cartaxo et al. (57) reported that FT-Raman spectroscopy could be used to differentiate cutaneous melanoma from pigmented nevus. Spectral measurements were recorded from normal, neoplastic, and pigmented nevi tissues using a 1,064-nm Nd:YAG laser with a spectral resolution of  $4\ \text{cm}^{-1}$ . A total of 140 spectra from neoplastic tissue, 105 from normal tissue, and 126 from pigmented nevi were collected. Raman spectra were first preprocessed by correcting the baseline and performing the vector normalization using Minitab software. The model of variance analysis with a constant factor was used at first phase, and this indicated that all variables showed an affiliation with their own group. In the next phase of the statistical study, a discrimination analysis was performed. The result of this analytical approach has demonstrated a significant differentiation between the three groups. Significant differences were found in the region of  $800\text{--}980\ \text{cm}^{-1}$ . Peaks at  $855$  and  $937\ \text{cm}^{-1}$  represent characteristics of the collagen spectrum. These peaks were reported due to the presence of proline and C—C stretching vibrations of protein structure. The Raman peak shifts were observed from  $1540\text{--}1620\ \text{cm}^{-1}$  and  $1040\text{--}1100\ \text{cm}^{-1}$  and this corresponded to DNA's vibrational mode. An increase in spectral intensity was reported in primary melanoma and it represents the increased duplication of genetic material responsible for the proliferation of malignant cells. The discriminatory analysis has demonstrated 75.3% efficiency in the differentiation among normal, neoplastic, and pigmented nevi groups.

Larraona-puy et al. (58) further reported that RMS could be used to discriminate between hair follicles and BCC in excised skin tissue explants during Mohs micrographic surgery. Spectral differences were observed among epidermis, BCC, and hair follicles. Raman spectral data of hair follicles was very similar to epidermis, whereas BCC spectral data were dissimilar and showed a high amount of DNA. Spectral differences clearly differentiated between hair follicles and BCC. This study has developed an LDA model, which is based on supervised Raman band selection. This approach has diagnosed BCC with  $90 \pm 9\%$  sensitivity and  $85 \pm 9\%$  specificity. It was also used to generate automated Raman spectral images and provide a diagnosis for new tissue sections containing BCC, dermis, epidermis, and hair follicles. Raman spectral images can differentiate hair follicles due to the greater amount of nucleic acids than the external epithelial layer spectra. These images have reported excellent correlation with hematoxylin and eosin images.

Wang et al. (59) developed a noninvasive system that combined two modalities, including Raman spectroscopy and confocal microscopy, to analyze a cutaneous murine tumor

model in vivo in terms of microstructures at different depths. A total of 494 Raman spectra were recorded from 24 tumor-bearing mice in vivo to assess the Raman spectral differences between different skin layers. The spectral changes involved in the epidermis, dermis, normal peritumoral skin, and skin immediately overlying subcutaneous tumors were analyzed in this study. The mean normalized Raman spectra of epidermis skin showed strong bands at 1061, 1128, and 1296  $\text{cm}^{-1}$  due to ceramide, whereas dermal spectra showed peaks at 855 and 937  $\text{cm}^{-1}$  due to the presence of collagen. The skin tumors' mean spectrum has higher intensities for the peaks at 724 and 1093  $\text{cm}^{-1}$  and the band at 1325–1330  $\text{cm}^{-1}$ , which occur from nucleic acids, pointing to a higher density of cells or nuclei in the tumor. Normal and tumor skin tissues showed clear spectral differences in phenylalanine, proline, and fatty acid absorption. Multivariate data analysis techniques such as PCA and LDA were used to analyze Raman spectra. This study has established sensitivity of 95.8% and specificity of 93.8% for tumor diagnosis. However, the micro-Raman system has the potential to demonstrate much higher accuracy in detecting specific spectral biomarkers and significantly improve the clinical diagnosis of different skin diseases.

Konig et al. (60) carried out multiphoton autofluorescence/second harmonics generation and coherent anti-Stokes Raman scattering (CARS) tomography on skin biopsies not only to detect biochemical changes but also to explore tissue architecture, intratissue cell morphology, and accumulation of various products in the pharmaceutical and cosmetic industries. The combination of these multiple techniques has produced a hybrid tomogram, which has provided valuable information about the outermost skin layer. Distributions of keratin and polygonal patterns of intracellular lipids in stratum corneum were revealed in this study. In vivo CARS was used to study the diffusion pattern of water and oil on the skin. This study has suggested partial accumulation of oil at the skinfold boundary and water was distributed within the tissue and the lipid-free fold regions. CARS was used to distinguish differences between normal healthy skin and psoriasis skin. CARS images revealed that corneocytes of healthy skin were always surrounded by bright lipid structures, whereas pathological skin lacked such structures and the intracellular spaces appeared dark.

de Oliverira et al. (61) applied FT-Raman spectroscopy to discriminate between primary and metastatic cutaneous melanoma, aiming toward a differential diagnosis. This study analyzed fragments of normal skin, cutaneous melanoma, and lymph node metastasis. A 1,064-nm Nd:YAG laser was used as the excitation source for FT-Raman spectral recording. The melanoma spectrum showed a decrease in the amide I peak with spectral area distortion between 1640 and 1670  $\text{cm}^{-1}$  due to alterations in protein molecular composition. The melanoma spectra showed increased intensities at 1475 to 1640  $\text{cm}^{-1}$  (proteins and lipids), 1200 to 1300  $\text{cm}^{-1}$  (amide III and lipids), and 1300–1400  $\text{cm}^{-1}$  (melanin) and decreased intensities at 920 to 980  $\text{cm}^{-1}$  (protein). Although DNA vibrational mode peak shifts were observed at 1540–1620  $\text{cm}^{-1}$  and 1040–1100  $\text{cm}^{-1}$  in both primary and metastatic melanoma, the metastatic group showed higher intensities due to an increase in nucleic acids and mitosis. The metastasis group showed a decrease in amide I intensities and an increase in melanin, amide III, protein, and lipid intensities compared to the primary melanoma group. This study has laid foundations to establish FT-Raman research in the diagnosis of cutaneous melanoma in vivo.

The design of an auto-classifying system and its application in Raman spectroscopy diagnosis of gastric carcinoma was investigated by Tan et al. (62). They developed a tentative user-friendly auto-classifying system to classify Raman spectra of gastric carcinoma tissues. They also suggested that the software could be applied for classification of other tissues by some necessary alterations.

Shetty et al. (64) demonstrated the potential of Raman spectroscopy for the identification and classification of the malignant changes in esophageal carcinomas. The study aimed to understand the biochemical changes that distinguish between the different stages of disease through Raman mapping studies. This technique was used to analyze 20- $\mu\text{m}$  sections of tissue from 29 snap-frozen oesophageal biopsies. Contiguous hematoxylin and eosin sections were reviewed by a consulting pathologist. Changes were noted in the distribution of DNA, glycogen, lipids, and proteins. The main spectra obtained from selected regions demonstrated increased levels of glycogen in the squamous area compared to increased DNA levels in abnormal region. It was concluded that Raman spectroscopy is a highly sensitive and specific technique for demonstration of biochemical changes in carcinogenesis, and there is potential for in vivo application for real-time endoscopic optical diagnosis.

Feng et al. (65) recently reported SERS on blood plasma analysis for nasopharyngeal cancer detection. In this investigation, the application of SERS in combination with multivariate analysis was explored for noninvasive gastric cancer detection. This study has revealed significant SERS spectral differences between normal and tumor samples. Primary SERS bands at 494, 589, 638, 725, 813, 886, 1004, 1075, 1134, 1207, 1330, 1445, 1580, and 1653  $\text{cm}^{-1}$  were all observed in both normal and tumor blood plasma, with the strongest intensities at 494, 638, and 1134  $\text{cm}^{-1}$ . The SERS peak-normalized intensities at 494, 589, 638, 813, and 1134  $\text{cm}^{-1}$  were more intense for normal plasma than for tumor plasma, whereas SERS peaks at 1330, 1445, and 1580  $\text{cm}^{-1}$  were higher in gastric cancer plasma samples. The SERS band at 1445  $\text{cm}^{-1}$  corresponded to the C–H bending mode of collagen or phospholipids and was higher in cancer plasma than in normal plasma. The SERS band at 1580  $\text{cm}^{-1}$  corresponded to the C=C bending mode of phenylalanine, where the percentage signals were significantly increased in cancer patient plasma, pointing out an increase in the percentage of phenylalanine content relative to the total SERS-active components in the plasma of gastric cancer patients. Multivariate approaches such as PCA and LDA differentiated gastric cancer normal samples with diagnostic sensitivity of 79.5% and specificity of 91%. This study has revealed great promise for developing SERS plasma analysis for noninvasive detection and screening of gastric cancers.

Chen et al. (119) reported that a combination of Raman spectroscopy and a multivariate approach can improve the diagnosis of nasopharyngeal carcinoma detection. Classification algorithms like PCA, LDA, Bayesian classification (BC), and Mahalanobis distance were used to improve better classification from normal to cancerous tissues. Raman spectra were collected from nasopharyngeal tissue biopsies and analyzed using a 785-nm diode laser. Spectral variations between normal and cancer cells were relatively small but relative peak intensities of normal versus cancer cells showed increased amounts of collagen and nucleic acid content. Chemometric approaches have separated cancer spectrum from normal with high sensitivity, specificity, and overall diagnostic accuracy of 98, 99, and 99%, respectively.

Kawabata et al. (66) reported that NIR multichannel Raman spectroscopy could be used as a potential diagnostic tool in gastric malignancies. This study has used a 1,064-nm laser to distinguish nonneoplastic samples from cancer lesions, which were surgically resected after diagnosis of gastric cancer. A total of 213 Raman spectra were obtained from both types of samples. PCA was performed and 10 PCs were considered further discrimination analysis. The PCA-based diagnostic algorithm yields a sensitivity and specificity of 73% and overall accuracy of 72% for detecting cancer. The discrimination algorithm resulting from PCA attained a sensitivity of 98%, specificity of 84%, and overall accuracy of 93% for discriminating early cancer from advanced stages. This unsupervised algorithm yields sensitivity of 95%, specificity of 100%, and overall accuracy of 98% for distinguishing differentiated cancer from undifferentiated cancer. This study might be helpful for

physicians who perform complete endoscopic submucosal dissection as well as in endoscopic treatment.

Su et al. (67) applied Raman confocal microspectroscopy to detect biochemical variations between normal and malignant oral tissues and normal and oral squamous cell carcinoma cells. Spectral profiles of normal and malignant samples showed many marked differences, and multiple Raman markers were identified in this study. These markers were mainly associated with DNA and protein vibrational features to distinguish between normal and cancerous samples. PCA was performed to reduce the number of parameters needed to represent the variance and the new principal component scores represented the maximum variance in the data. The most pronounced differences were observed in the range of 700–1800  $\text{cm}^{-1}$ . The Raman spectra of both normal and malignant tissue have shown tryptophan (756 and 1546  $\text{cm}^{-1}$ ) and phenylalanine (1004  $\text{cm}^{-1}$ ) peaks. The malignant tissue displayed Raman peaks at 1341 and 1655  $\text{cm}^{-1}$ , which corresponds to adenine and guanine of DNA and amide I of protein, respectively. The essential findings of this work have proven that Raman spectroscopy offers enormous potential in distinguishing between normal and malignant lesions and it can assist histopathologists.

Kendall et al. (69) reported that novel confocal Raman probe design technology could be used as a potential optical biopsy targeting tool in diagnosis of esophageal adenocarcinoma. This group developed a Raman classification model in their previous study. The model was based on the discrimination of nine pathological groups, namely, normal squamous epithelia, cardiac-type mucosa, fundic-type mucosa, intestinal-type Barrett's, low-grade dysplasia, high-grade dysplasia, adenocarcinoma, squamous dysplasia, and squamous cell carcinoma. A total of 1,304 Raman spectra were collected from 123 esophageal biopsy samples, which were grouped as normal, low risk (Barrett's oesophagus), and high risk (dysplasia and cancer) using an 830-nm laser excitation source. A training model was developed using 590 spectra measured with an acquisition in 10 s. This model has shown sensitivity of 71–81% and specificity of 81–98%. The classification ability of the 2-s spectra has yielded 66–81% sensitivity and 80–98% specificity. When these 2-s spectra were projected on training model, it yielded 66–84% sensitivity and 81–96% specificity. This study found a remarkable number of false negatives, where high-risk samples were misclassified as either normal or low risk groups. This study was able to successfully differentiate between normal and other tissues, although there was considerable variance between the low- and high-risk groups. An optical biopsy probe is an endoscopic equivalent tool that provides high signal-to-noise spectral information in a clinical setting in minimal time. Current endoscopic procedures require multiple biopsies that can be reduced substantially; in addition, the Raman probe can facilitate targeted excisional biopsy in esophageal cancer.

Lloyd et al. (120) reported that an ex vivo Raman confocal fiber-optic probe could be useful in improving diagnosis standard of esophageal cancer. Raman spectra were collected from tissue biopsies using an 830-nm diode laser. This study used a semi-supervised learning approach such as semi-supervised LDA (ssLDA) to discriminate between different grades of esophageal cancer grades. The aim of this study was to identify the diagnostic accuracy of nonconsensus samples from true pathological biopsies, which was determined by the LDA model. Significant sensitivity and specificity were achieved in discrimination among intestinal metaplasia, dysplasia, and low-grade dysplasia. The current study has proved that application of chemometrics not only increases disease classification performance but also allows larger training data sets to develop more robust diagnostic models.

Almond et al. (121) employed endoscopic Raman spectroscopy for diagnosis of adenocarcinoma and esophageal high-grade dysplasia. Raman spectra were collected from ex

vivo esophageal tissue biopsies using a Raman probe provided with an 830-nm laser resource. Raman has successfully differentiated epithelial and mucosal disease samples with a sensitivity of 96% and specificity of 92%. LDA trained classification models have detected high-grade dysplasia and esophageal adenocarcinoma with sensitivity and specificity of 86% and 88%, respectively. The results based on this study have proved that endoscopic Raman spectroscopy has potential as a rapid objective in *in vivo* diagnosis.

Lakshmi et al. (70) conducted a Raman study on radiation damage of brain tissue in mice. A set of studies was carried out on brain tissue from mice subjected to irradiation to identify the biochemical changes in tissue as the result of radiotherapy and radiation injury. It was shown that brain irradiation produces drastic spectral changes even in tissue far removed from the irradiation site. The changes were very similar to those produced by the stress of inoculation and restraint and the administration of an anesthetic drug. Though the changes produced by stress or anesthetics last for only a short time (a few hours to 1 or 2 days), radiation-induced changes persist even after one week. The results also supported the hypothesis that various protective factors are released throughout the body when the central nervous system is exposed to radiation.

Human brain tissue, in particular white matter, contains a high lipid content. These brain lipids can be divided into three principal classes: neutral lipids including the steroid cholesterol, phospholipids, and sphingolipids. Major lipids in normal human brain tissue are phosphatidylcholine, phosphatidylethanolamine, phosphatidylserine, phosphatidylinositol, phosphatidic acid, sphingomyelin, galactocerebrosides, gangliosides, sulfatides, and cholesterol. Minor lipids are cholesterol ester and triacylglycerides. Detailed research on NIR Raman spectra was carried out by Krafft et al. (71). They recorded the Raman spectra of 12 major and minor brain lipids with 785 nm excitation in order to identify their spectral fingerprints for qualitative and quantitative analysis.

Sato et al. (72) reported that Raman spectroscopy could be used to detect molecular changes occurring due to physiological changes in living brain tissue *in situ*. This study used an NIR Raman system equipped with a Raman probe made up of ball lens hollow fibers and a Ti:sapphire laser; 785- and 720-nm excitation wavelengths were used to obtain Raman spectra in the fingerprint region ( $600\text{--}1800\text{ cm}^{-1}$ ) and high wavenumber region ( $2600\text{--}3800\text{ cm}^{-1}$ ), respectively, in order to avoid the low-sensitivity range ( $>1,000\text{ nm}$ ) of the CCD detector. The aim of this study was to identify protein and lipid alterations and water cluster conformation under different conditions, namely, inhalation of sodium pentobarbital (SP) and diethyl vapor (DE) after euthanasia. The spectra of sodium pentobarbital showed peaks at  $1664$ ,  $1446$ , and  $1003\text{ cm}^{-1}$ , which are consigned to amide I, CH bending, and phenylalanine, respectively. The spectra of DE showed peaks at  $2846$ ,  $2881$ , and  $2928\text{ cm}^{-1}$ , which are associated with the CH stretching modes of the protein and lipid groups. The peak at  $3453\text{ cm}^{-1}$  are associated with water cluster species and it denotes that the change in conformational clusters due to the inhalation of DE. The intensity of the water band decreased approximately 7.7% in the spectrum obtained after euthanasia. This study has provided new insights for Raman approach for further analysis in conscious animals.

Kohler et al. (73) reported that Raman spectroscopy could be used to characterize the biochemical changes in lipid extracts of brain tumors. This study used fresh porcine brains, glioblastoma multiforme (GBM) tissue, and healthy brain tissue for Raman investigation. The spectra of porcine brain showed Raman peaks at  $720$  and  $878\text{ cm}^{-1}$ , which corresponds to the choline group of phosphatidylcholine and sphingomyelin. The bands near  $1087\text{ cm}^{-1}$  are consigned to the phosphodioxo group present in phospholipids and in sphingomyelin. Differences in porcine gray and white matter were observed at peaks  $1268$  and  $1660\text{ cm}^{-1}$ , which are assigned to unsaturated fatty acids; Raman peaks were at  $430$ ,  $546$ ,  $608$ ,  $701$ ,

and  $1440\text{ cm}^{-1}$ , which correspond to cholesterol content. Fatty acid unsaturation was predominant in gray matter, whereas high cholesterol content was reported in white matter. Lipid extracted from GBM was analyzed using Raman spectroscopy, the intensity ratios of the bands appeared at  $720$  and  $701\text{ cm}^{-1}$ , which represent phosphatidylcholine and cholesterol, respectively. The intensity ratio of phosphatidylcholine and cholesterol bands was increased in GBM compared to healthy brain. Raman spectra of GBM illustrated increased intensities at  $1159$  and  $1527\text{ cm}^{-1}$ , assigned to carotenoids, that have also formerly been identified in Raman spectra of brain tumors. The lipid composition and lipid content are correlated with the tumor grade, and this approach has shown great promise in the diagnosis of brain tumors.

Kirsch et al. (74) demonstrated that Raman imaging could be used to study intercerebral tumors. Brain tissue sections, pristine brain tissue, and whole mouse brain *ex vivo* were used to examine cerebral pathology through *in vivo* Raman mapping to localize cerebral brain metastases. The spectral band near  $2933\text{ cm}^{-1}$  is associated with vibrations of  $\text{CH}_2$  and  $\text{CH}_3$  moieties in proteins and lipids. Other spectral bands of normal brain tissue slightly differ in the intensities of valence vibrations of OH bonds near  $3245$  and  $3245\text{ cm}^{-1}$  that are mainly allocated to water. Most prominent bands are allocated to the aromatic amino acid phenylalanine ( $1004\text{ cm}^{-1}$ ), unsaturated fatty acids ( $1267$  and  $1661\text{ cm}^{-1}$ ),  $\text{CH}_2$  and  $\text{CH}_3$  deformation vibrations ( $1301$  and  $1445\text{ cm}^{-1}$ ), and the amide bands of protein backbones ( $1267$  and  $1661\text{ cm}^{-1}$ ) that overlap with spectral contributions of fatty acids. The Raman spectrum of the midline contains additional peaks due to oxygenated haemoglobin near  $750$ ,  $1002$ ,  $1212$ ,  $1546$ ,  $1605$ , and  $1619\text{ cm}^{-1}$ . Raman spectra of the tumor demonstrate spectral contributions due to melanin near  $597$ ,  $976$ ,  $1404$ , and  $1595\text{ cm}^{-1}$ . The melanin pigment was expressed by tumor cells and it can be used as an inherent marker of these brain metastases. Hence, further development in nonlinear Raman spectroscopy-associated fiber probe research can increase the prospect of Raman spectroscopy as a diagnostic tool for localized and metastatic diagnosis of various primary organs in mice.

Tay et al. (75) reported the first Raman spectroscopic signature of the brain, using the motor cortex from acute mouse brain injury. In this study, the injury was mechanically initiated in the motor cortex through a cranial window and Raman was performed on the healthy and injured motor cortices immediately after the whole brain was isolated from the skull. A comparative study has shown several common peaks at  $1002$ ,  $1090$ ,  $1130$ ,  $1274$ ,  $1450$ , and  $1660\text{ cm}^{-1}$  in the fresh and fixed tissue, whereas the Raman bands at  $1003\text{ cm}^{-1}$  (C–N stretch of phenylalanine) and  $1740\text{ cm}^{-1}$  (lipid carbonyl stretch) are consistently different between both samples. The characteristic amide I vibration at  $1660\text{ cm}^{-1}$ , one of the most foremost features observed from all healthy brain tissues, was much weaker in the spectra reported from the injured brain tissues. Spectral data from injury showed the band at  $1002\text{ cm}^{-1}$  (phenylalanine). It was observed that it was either weak or absent compared to the strong feature in the undamaged hemisphere. In addition to above peak, this group noticed a peak structure in the region of the amide III vibration, and two additional bands at  $1175$  and  $1227$ – $1740\text{ cm}^{-1}$  were observed in spectra obtained from the injured site. The spectral fingerprint obtained from Raman was further complemented by neurobiological and immunohistochemical experiments. These results have established a possible correlation between new Raman peaks and caspase 3-associated mitochondrial cellular apoptosis. Multivariate analysis such as PCA and LDA will facilitate further investigation of biochemical differences related to brain injury.

Malini et al. (76) worked on discrimination of normal, inflammatory, premalignant and malignant oral tissue using Raman spectroscopy. Spectral profiles of different samples

showed pronounced differences between one another. It was demonstrated that all four tissue types could be discriminated and diagnosed correctly. The biochemical differences between normal and pathological conditions of oral tissue were also discussed.

Application of a Fourier transform infrared (FTIR) fiber-optic technique for distinguishing malignant from normal oral tissues was reported by Wu et al. (77). According to the results, the  $1745\text{ cm}^{-1}$  band, which is assigned to the ester group (C=O) vibration of triglycerides, is a reliable marker that is present in normal tissue but absent or weak in malignant oral tissues. In addition, other bands such as C—H stretching and the amide bands are helpful in distinguishing the two groups of samples. Raman spectroscopic measurements were in agreement with results observed from FTIR spectra.

In another work, Lau et al. (78) studied Raman spectroscopy for optical diagnosis of the larynx. The objective of the research was to determine whether Raman spectra could be obtained rapidly from laryngeal tissue *in vitro* and compare Raman spectra from normal, benign, and cancerous laryngeal tissue. Good quality spectra were obtained with a 5-s signal acquisition time. Spectral peak analysis showed prediction sensitivities of 89, 69, and 88% and specificities of 86, 94, and 94% for normal tissue, carcinoma, and papilloma. Spectral differences appeared to exist between different samples and it was concluded that the ability of obtaining the spectra rapidly supports potential for future *in vivo* studies.

An FT-NIR Raman spectrometer was used in the present research in order to detect samples of oral mucosa, leukoplakia, and squamous cell carcinoma. Normal oral mucosa was acquired from squamous cell carcinoma patients and was characterized into groups by pathologist. Raman spectra were recorded using an Nd:YAG laser (1,064 nm) with a resolution of  $8\text{ cm}^{-1}$ . A support vector machine was employed to classify the Raman spectra of different groups and to establish discriminating model. The efficiency of this algorithm was evaluated by its specificity, sensitivity, accuracy, Matthew coefficient correlation, and rigidity. Raman spectra of squamous cell carcinoma showed peaks at 747, 897, 939, 1060, 1125, and  $1610\text{ cm}^{-1}$  corresponding to  $\text{CH}_2$  rocking, C—C skeletal stretching, C—C stretching, C=C bending in phenylalanine and tyrosine, C—N stretching in phenylalanine, and amide I, respectively. The difference between the mean spectra was relatively small in normal mucosa and leukoplakia. In addition, by comparison with subtracted mean spectrum of normal mucosa and squamous cell carcinoma, the peaks were not as noticeable in the background noise. The primary purpose of this model was able to differentiate correctly between the two classes of spectra, and FT-NIR-Raman and this algorithm successfully separated squamous cell carcinoma from normal mucosa. The efficiency of this model in discriminating the normal tissue and leukoplakia was lower, but resulted in further elimination of the low-grade hyperplasia data set, and the accuracy and rigidity of the model improved. This might be due to the less proliferative nature of leukoplakia and the difference in biochemical fingerprinting, between leukoplakia and normal mucosa was not as significant as that between squamous cell carcinoma and normal mucosa. Therefore, using these approaches in combination demonstrated great potentiality for detection. This investigation provides a research-based and theoretical foundation for developing a real-time, trauma-free, and accurate diagnostic strategy for oral mucosal lesions (79).

The major aim of this Raman investigation is to assess the biochemical variations and inter-anatomical variations of different normal tissues in the oral cavity. Bergholt et al. (80) studied different tissue sites in the fingerprint region of *in vivo* Raman spectra. There were eight measurement sites, which were predefined and had distinctive anatomical locations in the oral cavity, including the hard palate, soft palate, buccal, inner lip, attached gingiva, floor, anterior dorsal tongue, and ventral tongue. This research work has identified distinct Raman bands that are highly associated with proteins, DNA, lipids, and bone/tooth

minerals. There were marked differences in the spectral properties among the various anatomical sites. Raman peak intensity changes, especially for the Raman bands at 820, 853, 936, 956, 1070, 1265, 1302, 1450, 1575, 1670, and 1745  $\text{cm}^{-1}$ , reconfirmed that the oral tissue indeed is relatively complex. A semiquantitative spectral modeling was employed based on non-negativity-constrained least squares minimization and PLS-DA for the evaluation of inter-anatomical variability and to render multiclass algorithms for clusterings of different tissues in the oral cavity. For multiclass classification, PLS-DA was employed and the clustering dendrogram has divided into three major clusterings, namely, (1) buccal, inner lip, and soft palate; (2) dorsal, ventral tongue, and floor; (3) gingiva and hard palate. A range of difference in spectra along with these algorithms revealed that inter-anatomical variability is significant and it should be considered as an important parameter in the interpretation and rendering of diagnostic decision on oral tissue diagnosis and characterization.

Lau et al. (81) reported on Raman spectroscopy for optical diagnosis in normal and cancerous tissue of the nasopharynx. The tissues obtained from biopsies were studied using a rapid acquisition Raman spectrometer. The spectra were collected in 5 s and consistent differences were noted between normal and cancerous tissue in three bands at 1290–1320, 1420–1470, and 1530–1580  $\text{cm}^{-1}$ .

Raman spectroscopy was used to quantify the cellular activities such as monitoring of the biomaterial during fabrication in a tissue-engineered ex vivo model. Lo et al. (82) reported that Raman can be successfully used as real-time monitoring tool to understand keratinocytes maturation during fabrication processes. Raman spectra were taken from human normal oral mucosa and the corresponding tissue-engineered ex vivo model with a confocal Raman spectroscopy system with a 632-nm, 18-mW He-Ne laser. The normal human keratinized oral mucosa Raman spectrum showed a weak amide I peak at 1650  $\text{cm}^{-1}$ , a strong  $\text{CH}_2$  deformation peak at 1440  $\text{cm}^{-1}$ , broad peaks in amide III at 1200–1350  $\text{cm}^{-1}$ , a broad C–OH peak at 1080  $\text{cm}^{-1}$ , and a sharp phenylalanine peak at 1004  $\text{cm}^{-1}$ . The peaks collected clearly indicate contributions from proteins and lipids. The Raman spectra of the tissue-engineered ex vivo model showed a sharp and strong amide I peak at 1655  $\text{cm}^{-1}$ , a strong  $\text{CH}_2$  deformation peak at 1440  $\text{cm}^{-1}$ , broad peaks in the amide III region at 1200–1350  $\text{cm}^{-1}$ , a broad C–OH peak at 1080  $\text{cm}^{-1}$ , and a sharp phenylalanine peak at 1001  $\text{cm}^{-1}$ . A credible linear regression of the amide I/phenylalanine peak ratio of the tissue-engineered ex vivo model at different cultivating days with different maturation stages was observed. The stable peak intensity of the phenylalanine band at 1004  $\text{cm}^{-1}$  could be explained by the active catalysis of phenylalanine by viable keratinocytes grown on the tissue-engineered ex vivo model. This study has established Raman as a good quantitative marker for understanding the maturation process of the three-dimensional constructs.

Li et al. (83) applied Raman spectroscopy and fluorescence for the detection of liver cancer and abnormal liver tissue. They measured laser-induced human serum Raman spectra of liver cancer and analyzed the spectral differences between people without liver cancer and liver cancer patients. The results from more than 200 case measurements showed that the spectral diagnosis was in good agreement with the clinical results. The experiment indicated that the blue shift of fluorescence peak difference between normal, liver fibrosis, and liver cirrhosis.

Guo et al. (84) reported that Raman spectroscopy could be used to differentiate malignant hepatocytes from normal liver cells. In this study, the research was focused on exploring whether a Raman spectroscopy-associated statistical analysis method is capable of categorizing normal and malignant hepatocytes with high accuracy and attain more information about the spectral differences between normal and malignant hepatocytes.

Statistical methods such as *t* test, PCA, and LDA were used to analyze the Raman spectra of both cell lines. The mean Raman spectra of normal and malignant cells in the region of 600–1800  $\text{cm}^{-1}$  showed that the strong bands at 1447 and 1656  $\text{cm}^{-1}$  can be attributed to the  $\text{CH}_2$  deformation mode and the  $\text{C}=\text{C}$  stretching mode of the lipids and proteins, respectively. The band originating at 786  $\text{cm}^{-1}$  can be assigned to the  $\text{O}-\text{P}-\text{O}$  stretching mode of DNA. The bands appearing at 1004 and 1032  $\text{cm}^{-1}$  can be assigned to the symmetric ring breathing mode and the  $\text{C}-\text{H}$  in-plane bending mode of phenylalanine, respectively. A *t* test was carried out on the nine major bands at 786, 825, 852, 1004, 1230–1280, 1311, 1447, 1585, and 1625–1720  $\text{cm}^{-1}$ . The results of *t* test confirmed that the intensities of these bands are considerably different between two cell lines, except for the 1585 and 1625–1720  $\text{cm}^{-1}$  bands. In order to differentiate between normal and malignant hepatocytes, a total of 50 spectra were analyzed by PCA and LDA. Ten principal components from PCA were used to feed the LDA model by leave-one-out cross-validation, and then one discriminant function was obtained. The results visibly demonstrated that the high accuracy of 100% for Raman spectroscopic identification of normal and malignant hepatocytes was based on PCA and LDA.

Schie et al. (85) employed CARS and Raman spectroscopy to study dynamic changes of lipid droplets in live primary hepatocytes. A pathologic hallmark of liver injury is an increased accumulation of intracellular lipid droplets within hepatocytes. The laser (1,064 nm Nd:YVO4) was used as the Stokes probe beam to image lipid dynamics in primary rat hepatocytes. Raman spectra of lipid droplets were acquired over the spectral region from 500 to 3100  $\text{cm}^{-1}$  from variable-sized lipid droplets within hepatocytes. This spectrum corresponds to a typical lipid Raman spectrum composed mainly of contributions from  $\text{C}-\text{C}$ ,  $\text{C}-\text{H}$ , and  $\text{C}=\text{O}$  bond vibrations. Specifically, the 1266 and 1302  $\text{cm}^{-1}$  are an in-plane  $1/4\text{C}-\text{H}$  double-bond vibration in the *cis* configuration and  $\text{CH}_2$  twisting mode, respectively. The 1446  $\text{cm}^{-1}$  vibration is a combination of a  $\text{CH}_2$  twisting mode and the 1455  $\text{cm}^{-1}$   $\text{CH}_2$  scissoring mode and its intensity is a good measure of the total lipid content in the droplets. The peak at 1655  $\text{cm}^{-1}$  is a  $\text{C}=\text{C}$  stretch vibration in the *cis* configuration and represents the degree of hydrocarbon chain unsaturation. The peak at 1742  $\text{cm}^{-1}$  indicates the  $\text{C}=\text{O}$  ester group and represents triglyceride esterification within the lipid droplets. Palmitic acid treatment resulted in an increase in the intensities at 1302 and 1444  $\text{cm}^{-1}$ . Additionally, a new peak at 1630  $\text{cm}^{-1}$  assigned to 13-hydroxy-9,11-octadecadienoic acid (13-HODE) appeared and the 1656  $\text{cm}^{-1}$  unsaturated lipid peak decreased considerably. This reduction pointed out that 13-HODE is an important factor leading to the increased accumulation of saturated fatty acids in lipid droplets. Treatment of hepatocytes with a combination of palmitic acid and 13-HODE led to a stark change in the lipid droplet spectra. The 860  $\text{cm}^{-1}$  peak disappeared and a new peak at 891  $\text{cm}^{-1}$  became apparent, corresponding to a  $\text{CH}_2$  rocking vibration. These findings provided insight into a combined approach of CARS and Raman in studying the effects of metabolic disorders and diseases.

Movasaghi et al. (86) employed Raman spectroscopy to study testicular cancer at the cellular level. The aim of this study was to identify spectral differences between sensitive and resistant types of cell lines. Spectra were obtained using different lasers. The sensitive subtype expressed specific bands at 483  $\text{cm}^{-1}$  ( $\text{PO}_4^{3-}$  vibration) and 862  $\text{cm}^{-1}$  ( $\text{C}-\text{C}$  stretching and  $\text{C}-\text{H}$  bending). These are not found in resistant subtypes. A PLS-DA algorithm was applied on spectral data to discriminate between these two subtypes. The advantage of this method over other unsupervised approaches is identification of linear combination, which can be used in LDA analysis. The peaks at 437 and 487  $\text{cm}^{-1}$  were selected for ratio classifier in distinguishing between these two cell types. This approach

has achieved discrimination accuracy of 96–100% and has provided new understandings of the chemical fingerprint of testicular cancer tissues.

Another FT-Raman spectroscopy study was carried out Chiang et al. (87) on the carcinogenic polycyclic aromatic hydrocarbons in biological systems and their banding to heme proteins. The Raman spectra of benzo[a]pyrene (BaP), a typical carcinogenic polycyclic aromatic hydrocarbon, were acquired under different conditions and analyzed. It was concluded that CH wagging and ring stretching mixed strongly with CH in-plane bending were the most significantly affected vibrations.

It was confirmed that the intrinsic Raman scattering intensity of single-walled carbon nanotubes (SWNTs) does not decay over time. Raman spectroscopy was subsequently used to measure the postinjection blood concentration of SWNTs with different polyethylene-glycol (PEG) coatings in mice and therefore glean nanotube blood circulation times. Raman spectroscopy and Raman imaging were also employed in this investigation to probe the bio-distribution of SWNTs in various organs of mice *ex vivo* over a period of several months. It was established that the surface chemistry of nanotubes was critical to their *in vivo* behavior. This result was expected due to pristine carbon nanotubes, which have very hydrophobic surfaces and are highly nonspecific in binding to biological species. Recently, it was discovered that intravenously injected pristine SWNTs are highly rich in the lung and also in reticuloendothelial system and remain in mice indefinitely. This hydrophobicity has to be blocked by proper chemical functionalization such as the PEG coatings, which enables biologically inert SWNTs with long blood circulation, low reticuloendothelial system uptake, and relatively fast clearance from organs and excretion from the body. For the *in vivo* behavior of nanotubes the degree of PEGylation of SWNTs is important. Longer PEG chains, especially those with branched structures, are excellent in affording SWNTs with the most desirable characteristics for *in vivo* applications. This finding should also be applicable to functionalization of various other nanomaterials such as nanocrystals, particles for *in vivo* research. SWNTs detected in the faeces of mice clearly revealed that the biliary excretion pathway. A proportion of nanotubes seemed to be excreted via the renal pathway. In addition, no obvious toxic effect was found in the necropsy, histology, and blood chemistry studies, which warrants the safety of properly functionalised carbon nanotubes for future *in vivo* biomedical applications (122).

van de Poll et al. (88) reported on Raman spectroscopic evaluation of the effects of diet and lipid-lowering therapy on atherosclerotic plaque development in mice. Through this technique, they could quantitatively characterize the plaque without using standard destructive histopathological methods such as sectioning. Raman spectra were obtained over the full width and entire length of the ascending aorta and aortic arch. Spectra were modeled to calculate the relative dry weights of cholesterol and calcium salts, and quantitative maps of their distribution were created. In conclusion, Raman spectroscopy could be used to quantitatively study the size and distribution of depositions of cholesterol and calcification. It also could be used for the quantitative investigation of atherosclerosis and lipid-lowering therapy in larger animals or humans *in vivo*.

Duarte et al. (89) investigated the use of NIR Raman spectroscopy to detect immunoglobulin G and immunoglobulin M antibodies against *Toxoplasma gondii* in serum samples of domestic cats. The aim of this work was to investigate a new method to diagnosis *T. gondii*, instead of serological tests, which usually have a high cost and are time consuming as well. In conclusion, the possibility of antibody detection by Raman spectroscopy was confirmed.

Application of Raman spectroscopy of serum for cancer detection was investigated by Li et al. (90). The spectra of serum from cancerous and normal individuals were analyzed.

Three Raman peaks with intensities of 1005, 1156, and 1523  $\text{cm}^{-1}$  were consistently observed from normal blood serum samples, whereas no peaks or only very weak peaks were detected from tumorous cases.

Rohleder et al. (91) applied Raman spectroscopy as a tool for predicting the concentrations of different parameters in serum and serum ultrafiltrate. In an investigation using sample from 247 blood donors, the concentrations of glucose, triglycerides, urea, total protein, cholesterol, high-density lipoprotein, low-density lipoprotein, and uric acid were determined with accuracy within the clinically interesting range. After training a multivariate algorithm for the data analysis using 148 samples, concentrations were predicted blindly for the remaining 99 serum samples based solely on the Raman spectra. Relative errors of prediction around 12% were obtained. It was also shown that ultrafiltration can efficiently reduce fluorescent light background to improve prediction accuracy.

Neugebauer et al. (92) further reported that Raman imaging could be used to identify and differentiate circulating tumor cells from peripheral blood. Circulating tumor cells play an important role in tumor diagnosis and the alteration in these numbers over time can serve as a marker for tumor therapeutic studies. The aim of this study is to identify leukocytes, myeloid leukaemia cells, and solid tumor cells by using a combination of Raman spectroscopy and statistical approaches. Raman images were collected from dried cells using a 785-nm laser with a spectral resolution of 4  $\text{cm}^{-1}$ . The general features of these cells' spectra look very much alike but leukocytes showed higher intensities. Negative differences were observed near 780, 811, 851, 1004, 1034, 1302, 1441, and 1656  $\text{cm}^{-1}$  due to an increase in nucleic acid, lipid, and amino acid contents of cancer cells. An unsupervised statistical method such as hierarchical cluster analysis was applied on vector normalized average spectral region between 1800 and 500  $\text{cm}^{-1}$ . This analysis was performed using a Euclidean distance method and Ward's algorithm. The resulting dendrogram has well-separated leukocytes from other cell types. PCA studies further supported the clustering results. A supervised approach such as support vector machines classified the cells with high prediction accuracy of more than 97.7%. This pioneering research could assist not only in early cancer detection but could also be useful in monitoring cancer therapy.

Neugebauer et al. (93) applied Raman spectroscopy to detect and identify tumor cells based on biochemical variation. Leukocytes and erythrocytes were isolated from the peripheral blood of healthy donors, and myeloid leukaemia cells and breast carcinoma derived cells were obtained from cell cultures. A laser emitting 785-nm light was used for optical trapping of the single cells in the laser focus. Raman spectra were acquired from single cells in aqueous medium using a microscopic setup, which acted as optical tweezers. Raman spectra of cells suspended in phosphate-buffered saline buffer showed amide I (1657  $\text{cm}^{-1}$ ), phenylalanine and tyrosine (1605 and 1585  $\text{cm}^{-1}$ ),  $\text{CH}_2$  deformation (1450  $\text{cm}^{-1}$ ), amide III (1255  $\text{cm}^{-1}$ ), tryptophan (758  $\text{cm}^{-1}$ ), and  $\text{PO}_2^-$  backbone vibrations (1094  $\text{cm}^{-1}$ ). Raman spectra of the cancer cells and the leukocytes looked very much alike; the Raman spectrum of erythrocytes looked remarkably different from hemoglobin content, which gives rise to prominent sharp bands around 1621, 1584, 1564, 1374, and 755  $\text{cm}^{-1}$ . In order to develop a classification model for Raman spectra of five cell types in suspension, a supervised statistical approach such as support vector machines was used. Differentiation of cancer cells and normal cells from different donors and cultivation batches was achieved by employing supervised statistical methods with high sensitivity of >99.7% and specificity of >99.5%. Though the prediction accuracy of 92.4% is slightly lower for the differentiation between different cell types, the Raman-based approach also holds promise for determining the cell type and, consequently, the origin of the cancer cells.

Silveira et al. (94) reported on the correlation between NIR Raman spectroscopy and the histopathological analysis of the atherosclerosis in human coronary arteries. The objective of the study was to obtain feasible diagnostic information to detect atheromatous plaque using NIR spectroscopy. An 830-nm Ti:sapphire laser pumped by argon was used. A spectrograph dispersed light scattered from arterial tissue and a liquid nitrogen-cooled CCD detector was used to obtain Raman spectra. A total of 111 arterial fragments were scanned and Raman results were compared with histopathology. An algorithm was modeled for tissue classification into three categories, nonatherosclerotic (NA), noncalcified (NC), and calcified (C), using Raman spectra. Spectra were randomly separated into training and prospective groups. It was found that for the NA tissue the algorithm has sensitivity of 84 and 78% and specificity of 91 and 93% for training and prospective groups, respectively. For NC tissue the algorithm had sensitivity of 88 and 90% and specificity of 88 and 83%. For the C tissue both sensitivity and specificity were 100%.

Puppels et al. (95) investigated carotenoids located in human lymphocyte subpopulations (CD4+, CD8+, T-cell receptor- $\gamma\delta$ +, and CD19+) and natural killer cells (CD16+) using RMS. In CD4+ lymphocytes, a high concentration of carotenoids was found in the Gall body (about  $10^{-3}$  M). In other cell groups, except CD19+, carotenoids appeared to be concentrated in the Golgi complex (about  $10^{-4}$  M). The concentration of carotenoids in CD19+ lymphocytes was found to be below the present detection limit (about  $10^{-6}$  to  $10^{-5}$  M). The results provided new possibilities to investigate the mechanisms behind the suggested protective role of carotenoids against development of cancers.

Dochow et al. (96) employed a combination of Raman spectroscopy and optical traps to identify tumor cells in microfluid environments such as saliva, urine, or blood. Raman spectra were recorded from individual cells using optical tweezers and a 514-nm excitation source. This study used two optical traps, a quartz capillary coupled to a 785-nm laser source and a microfluidic glass chip associated with laser fibers of the optical trap. LDA classified normal cells and tumor cells and even identified cell type based on small variations. The LDA classification model for quartz capillary-based approach yielded an overall accuracy of 92.2%. The individual accuracy for erythrocytes, leukocytes, breast tumor cells, and myeloid leukemia cells was 95, 97.2, 94.5, and 94.6%, respectively. The overall accuracy of the second approach was 94.9% and LDA classified myeloid leukemia cells, breast tumor cells, and leukocytes with accuracies of 96.3, 95.4, and 86.2%, respectively. Erythrocytes were identified based on their size, shape, and pigmentation; leukocytes and leukemia cells have a shared common ancestry and are closely related to each other.

Lin et al. (97) reported on confocal micro-Raman spectroscopy to analyze the effects of paclitaxel on human Burkitt lymphoma cells. In this study, Raman was used to detect structural and functional changes associated with lymphoma cells, which are treated with different concentrations of paclitaxel. Raman spectra were recorded in the range of  $300\text{--}1800\text{ cm}^{-1}$  using a 785-nm diode laser with spectral resolution of  $2\text{ cm}^{-1}$ . The Raman spectra of control and treated cells showed clear spectral differences. As the concentration of drug increased, the band intensities at  $1094\text{ cm}^{-1}$  (O—P—O symmetric stretching) and  $1338$  and  $1578\text{ cm}^{-1}$  (adenine and guanine) decreased, which shows the effect of DNA replication due to destruction of DNA bases. On the contrary, the band intensities of O—P—O symmetric stretching ( $831\text{ cm}^{-1}$ ) and amide III ( $1258\text{ cm}^{-1}$ ) and amide I ( $1658\text{ cm}^{-1}$ ) increased due to possible conformational changes in DNA and protein double helix, respectively. Multivariate statistical approaches such as PCA and LDA were performed on Raman data to differentiate lymphoma cells from treated cells. The sensitivity and specificity of both approaches increased with increasing doses of drug and was up to 100% with high drug doses. Raman coupled with a multivariate approach has proved

that a 5  $\mu\text{g/mL}$  drug concentration is as effective and appropriate for damaging Burkitt lymphoma cells. This work has shown the potential of Raman to explore cytotoxicity and drug interaction studies.

Deng et al. (98) carried out a study on the effect of alcohol on single human red blood cells (RBCs) using NIR laser tweezers Raman spectroscopy. A low-power diode laser at 785 nm was applied for the trapping of a living cell and the excitation of its Raman spectrum. The denaturation process of single RBCs in 20% alcohol solution was investigated by detecting the time evolution of the Raman spectra at the single-cell level. The vitality of RBCs was characterized by Raman bands at  $752\text{ cm}^{-1}$ , which corresponds to the porphyrin breathing mode. They found that the intensity of this band decreased by 34.1% over a period of 25 min after the administration of alcohol. In a further study of the dependence of the denaturation on alcohol concentration, it was discovered that the decrease in the intensity of the  $752\text{ cm}^{-1}$  band became more prominent as the alcohol concentration increased.

Bonnier and Byrne (123) reported that a combination of Raman maps and vector quantization could be used to study molecular information of single cancer cells. K-means cluster analysis and PCA successfully differentiated molecular differences among cellular regions such as cytoplasm, nucleus, and nucleoli. Initially PCA was applied on pure biomolecular components such as albumin, RNA, and histones and scatterplots were correlated with loading points and resulting spectral differences were applied on complex data sets of single cells. The loading plots provided a complex mixture of molecular vibrations regarding lipids and nucleic acids. A pair-wise analysis approach clearly identified subcellular regions based on biochemical differences.

Liu et al. (99) employed Raman spectroscopy to study tumor apoptotic interactions between flavonoids and protease inhibitors. Both compounds share common functional features and they are divergent in structural and more of action. Spectra were collected from samples containing natural flavonoids like quercetin and protease inhibitors such as bortezomib and MG-262. Raman revealed significant stretching and ring vibrational differences between bortezomib and the combination of bortezomib and quercetin at  $950\text{ cm}^{-1}$  (C–C),  $830\text{ cm}^{-1}$  (C–O), and  $820\text{--}760\text{ cm}^{-1}$ , respectively. Spectral differences were at C–O symmetric and C–C twisting between quercetin and MG-262.

Krishna et al. (100) used micro-Raman spectroscopy to investigate randomly mixed cancer cell populations, including human promyelocytic leukaemia, human breast cancer, and human uterine sarcoma, as well as their respective pure cell lines. In this study, the efficiency of micro-Raman spectroscopy to identify a cell type in a randomly distributed mixed cell population was assessed. According to the results, cells from different origins can display variances in their spectral signatures and the technique can be used to identify a cell type in a mixed cell population via its spectral signatures.

Kuhnert and Thumser (101) reported on the use of RMS using a diode laser at 785 nm or argon ion laser at 512 nm. This technique was employed for detection of vibrationally labeled compounds in living human cells and positive results were obtained. They suggested that future research should concentrate on sensitivity and experimental setup in order to achieve better detection limits.

Chan et al. (103) worked on detection of the individual neoplastic and normal hematopoietic cells using micro-Raman spectroscopy. The potential application of confocal micro-Raman spectroscopy as a clinical tool for single-cell cancer detection based on intrinsic biomolecular signatures was demonstrated. They showed that this method can discriminate between different kinds of unfixed lymphocytes, and single-cell Raman spectra

provide a highly reproducible biomolecular fingerprint of each cell type. Characteristic peaks, mostly due to different DNA and protein concentrations, allowed discrimination between normal lymphocytes from transformed ones with high confidence ( $p \ll 0.05$ ). The method was shown to have a sensitivity of 98.3% for cancer detection, with 97.2% of the cells being correctly classified as belonging to the normal or transformed type.

Farguharson et al. (104) measured the chemotherapeutic drug 5-fluorouracil in saliva using SERS. A silver-doped sol-gel provided SERS and also some chemical selectivity. 5-Fluorouracil and physiological thiocyanate produced SERS, whereas large biochemicals, such as enzymes and proteins, did not, supporting the expectation that the larger molecules do not diffuse through the sol-gel to any appreciable extent. In addition, 5-fluorouracil samples of  $2 \mu\text{g/mL}$  were easily measured, and an estimated limit of detection of  $5 \mu\text{g/mL}$  in 5 min should provide sufficient sensitivity to perform pharmacokinetic studies and to monitor and regulate patient dosage.

Barhoumi and Halas (105) reported that SERS could be used to detect posttranslational modifications of DNA, and this study developed a link between chemical and DNA fingerprinting studies. Single-stranded DNA sequences of normal, adenine-methylated, and a mixture of both DNA with a length of 12 bases were used for spectroscopic studies. Adenine breathing mode at  $736 \text{ cm}^{-1}$  was dominant in normal DNA spectra and three new peaks at 390, 1100, and  $1197 \text{ cm}^{-1}$  were observed in adenine-methylated DNA due to 6-methyladenine. This study also identified methylated and hydroxymethylated cytosine and oxidized guanine in purely synthesized DNA. This study offered SERS as a promising tool for DNA-based diagnostic applications.

Characterization of conformational changes on guanine–cytosine and adenine–thymine oligonucleotides induced by amiooxy analogues of spermidine using Raman spectroscopy was accomplished by Ruiz-Chica et al. (106). These analogues resulted from the substitution of the two terminal aminomethylene groups of spermidine,  $^+\text{NH}_3\text{CH}_2$ , by an amnooxy one,  $\text{H}_2\text{NO}$ . The spectra demonstrated the existence of strong differences in the oligonucleotide-analogue interactions depending on base sequences. Different spectral features were observed. This fact supported the idea that the two amino terminal groups of spermidine could have different roles in the interaction this biogenic polyamine with DNA.

Jalkanen et al. (107) used vibrational spectroscopy to study protein and DNA structure and hydration and binding of biomolecules as a combined theoretical and experimental approach. The systems studied systematically were the amino acids, peptides, and a variety of small molecules. The goal was to interpret the experimentally measured vibrational spectra for these molecules to the greatest extent possible and to understand the structure, function, and electronic properties of these molecules in their various environments. It was also believed that the application of different spectroscopic methods to biophysical and environmental assays is expanding, and therefore a true understanding of the phenomenon from a rigorous theoretical basis is required.

Zhang et al. (108) demonstrated that stimulated Raman scattering (SRS) could be used for live cell imaging of nucleic acids. SRS, a coherent Raman scattering technique, has advantage over CARS in nonresonant background and spectral distortion. This study showed live cell imaging of two mammalian cell lines, namely, human embryonic kidney cells and breast cancer cells, and single polytene chromosomes within the salivary glands of *Drosophila melanogaster*, commonly known as the fruit fly. The targeted molecule concentration is linearly propositional to the SRS signal that can be used for imaging in the fingerprint region. Two excitation beams ( $1,064 \text{ nm}$  Nd:YVO4 laser and  $532 \text{ nm}$  Nd:YVO4 laser) with the frequency difference matching the vibrational frequency of targeted molecules were applied. Due to the high DNA concentration, the spectrum of

*D. melanogaster* larvae showed peaks at  $2845\text{ cm}^{-1}$  ( $\text{CH}_2$  vibration in lipids),  $1655\text{ cm}^{-1}$  (amide I proteins),  $785\text{ cm}^{-1}$  (phosphodiester stretch), and  $1090\text{ cm}^{-1}$  (dioxy stretch of the phosphate backbone). This study identified sporadic regions of heterochromatin and euchromatin and these are source of the banding pattern of polytene chromosomes. Raman can also detect cell division through imaging of DNA. Raman has impending perspective to identify cells undergoing cell division or apoptosis within living tissue.

Viehoever et al. (112) examined the use of organotypic raft as an in vitro model of in vivo tissue conditions in an attempt to overcome some of the limitations of previously used methods. In this study, organotypic raft cultures resembling normal and dysplastic epithelial cervical tissue were conducted and grown at an air-liquid interface for 2 weeks. Raman spectra of normal as well as dysplastic raft cultures were measured and compared with in vivo spectra from the corresponding tissue type. These investigations showed that the Raman spectra of the raft cultures were similar to the spectra acquired from the cervix in vivo for both normal and dysplastic tissues. It was concluded that this type of culture is an effective and useful tool for the cellular and biochemical analysis of tissue spectra.

Koljenovic et al. (113) conducted a study on meningioma and normal dura matter by Raman microspectroscopy to assess the possibility of developing an in vivo Raman method for guidance of meningioma resections. Raman maps were constructed of cryosections of dura and meningioma obtained from 20 patients. A comparison of these maps with histopathology enabled assignment of the spectra to either meningioma or dura. It was concluded that large differences exist between the Raman spectra of dura and meningioma, due to the high collagen content of dura and the increased lipid content of tumors. In this study, a classification model for dura and tumor tissue based on linear discriminant analysis of Raman spectra yielded an accuracy of 100%. It was shown that Raman spectra enable meningioma to be distinguished from dura. According to the authors, this can make Raman spectroscopy a viable candidate for guidance of surgical resection of meningioma.

Lieber et al. (114) reported that cancer field effects (CFEs) could be detected in normal tissues using Raman spectroscopy. The changes in normal tissues due to the effect of surrounding neoplastic lesions are collectively defined as CFEs or malignancy-associated changes. Organotypic tissue culture raft models were used in this study and Raman measurement were recorded from dermis and epidermis of both naïve and tumor-associated populations. Raman spectra of epidermis showed differences in amino acids near  $855\text{ cm}^{-1}$  (tyrosine and proline) and  $1004\text{ cm}^{-1}$  (phenylalanine). The Raman peak at  $1004\text{ cm}^{-1}$  suggests C-C vibration of keratin. The results showed some changes in amide III, protein, and lipid bands in the region  $1250$  and  $1340\text{ cm}^{-1}$ . Major differences were seen at the  $858\text{ cm}^{-1}$  shoulder of the  $855\text{ cm}^{-1}$  (tyrosine/proline) peak and in the  $1018\text{ cm}^{-1}$  neck region between the  $1004\text{ cm}^{-1}$  (phenylalanine/keratin) peak and the  $1040\text{ cm}^{-1}$  peak attributed to both proline and oxidized albumin. Furthermore, dermal spectra showed distinct differences in  $\text{CH}_2$  and  $\text{CH}_3$  deformations in the  $1420\text{ cm}^{-1}$  region. PCA classified naïve and tumor-associated rafts with a sensitivity of 94% and specificity of 78%. The results demonstrated above and previous data from various raft models showed Raman spectral changes to be a result of CFEs. This study validates the use of Raman in animal and clinical studies to detect the nature of CFE in multitissue and trans-organ environs, including the effects of hemodynamics and lymphatic circulation. Further research can potentially allow Raman as a tool to rapidly screen and diagnose internal tumors by analyzing readily available anatomy.

Silva et al. (115) reported that a combination of Raman spectroscopy and multivariate analysis such as PCA and Mahalanobis distance could be used to distinguish between

normal and prostate cancer (CaP) tissue. Raman spectra were collected from normal prostate tissues and neoplastic (CaP) tissues from patients submitted to radical prostatectomy using an 830-nm laser. The spectra of both tissues showed clear visible differences. The Raman spectra of cancerous tissues showed a lower intensity band at  $1655\text{ cm}^{-1}$  (C=O stretching mode of amide I of proteins and C=C stretching of lipids) and high intensity peaks at  $1452\text{ cm}^{-1}$  ( $\text{CH}_2$  bending mode of proteins),  $1330\text{ cm}^{-1}$  (DNA purine bases and  $\text{CH}_2/\text{CH}_3$  wagging of collagen), and  $1563\text{ cm}^{-1}$  (guanine and adenine from nucleic acid). The presence of high amounts of genetic material and protein represents the malignant nature of the cancer. The PCA analytical model showed better results compared to the biochemical model. It showed the capability of PCA/Mahalanobis to categorize the spectra. Despite the minor diagnostic capability, the simplified biochemical model exhibited that N tissue had greater protein-like characters and CaP has greater lipid-like characters.

Rabah et al. (116) reported that Raman spectroscopy can diagnose and classify neuroblastoma in children. A total 698 spectra were collected from normal adrenal glands, neuroblastomas, ganglioneuromas, nerve sheath tumors, and pheochromocytoma using a 785-nm laser resource. Higher amounts of carotenoids ( $1002$ ,  $1160$ , and  $1518\text{ cm}^{-1}$ ) were observed in the Raman spectrum of normal adrenal tissue. These peaks ( $1160$  and  $1518\text{ cm}^{-1}$ ) were absent in neuroblastomas and ganglioneuromas, signifying that their absence may also play a role in the carcinogenesis. The spectra of neuroblastomas and ganglioneuromas showed high protein intensity peaks at  $754$ ,  $853$ ,  $938$ ,  $1002$ ,  $1300$ – $1345$ ,  $1447$ ,  $1550$ ,  $1620$ , and  $1660\text{ cm}^{-1}$ . Raman spectroscopy successfully differentiated between normal adrenal glands, neuroblastoma, and ganglio-neuroma with 100% sensitivity and 100% specificity. These results are well correlated with the Shimada's histologic classification system with 100% sensitivity and 100% specificity. This study suggested that spectral profiles from different paediatric tissues and tumors will be use to create a library of molecular fingerprints. A large database can be accumulated from different institutes, which can then help to design and optimize a probe that can collect data in clinical paediatrics.

Finally, Short et al. (118) reported that Raman spectroscopy can monitor changes due to cell proliferation. This was done by investigating cultures in the plateau (nonproliferating) and exponential (proliferating) phases of growth and estimating the relative amounts of biochemical components (lipid, protein, DNA, RNA) in cells and nuclei. Using relative amounts and ratios of biochemical components, reproducible differences were detected and quantified. It was shown that the differences due to cell proliferation can be assigned to specific biochemical changes. A detailed explanation of the changes in quantities of these compounds and their ratios was presented, and it was concluded that this information can be important for Raman detection of rapidly dividing populations of cancer cells in vivo.

It has also been reported that the intrinsic Raman scattering intensity of SWNTs does not decay over time. Raman spectroscopy can subsequently be used to measure the postinjection blood concentration of SWNTs with different PEG coatings in mice and therefore glean nanotube blood circulation times. Raman spectroscopy and Raman imaging were employed to probe the bio-distribution of SWNTs in various organs of mice *ex vivo* over a period of several months. It has been established that the surface chemistry of nanotubes is critical to their *in vivo* behavior. This is due to pristine carbon nanotubes which have significantly hydrophobic surfaces and are highly nonspecific in binding to biological species. Recently, it was discovered that intravenously injected pristine SWNTs are highly rich in the lung and also in reticuloendothelial system and remain in mice indefinitely. This hydrophobicity has to be blocked by proper chemical functionalisation such as the PEG coatings, which enables biologically inert SWNTs with long blood circulation, low RES uptake, and relatively fast clearance from organs and excretion from the body. For the

in vivo behavior of nanotubes the degree of PEGylation of SWNTs is important. Longer PEG chains, especially those with branched structures, are excellent in affording SWNTs with the most desirable characteristics for in vivo applications. This finding should also be applicable to functionalization of various other nanomaterials such as nanocrystals, particles for in vivo research. SWNTs detected in the feces of mice clearly revealed the biliary excretion pathway. A proportion of nanotubes seems to be excreted via the renal pathway. In addition, no obvious toxic effect is found in necropsy, histology, and blood chemistry studies, which warrants the safety of properly functionalized carbon nanotubes for future in vivo biomedical applications (122).

Shapiro et al. (124) employed Raman microscopy to diagnose urothelial carcinoma commonly known as bladder cancer (BCa), from epithelial cells of the voided urine. Previous studies have attempted to discriminate BCa from normal bladder tissue using Raman spectroscopy. Raman spectra were obtained from normal and cancerous tissues using a 532-nm visible laser. A distinct peak at  $1584\text{ cm}^{-1}$  was observed in malignant tissue and it was absent in normal tissues. This group has developed a model based on peak height ( $1584\text{ cm}^{-1}$ ) of normalized spectrum and used sets of thresholds of the height to classify healthy, low-grade, and high-grade tumors. The model precisely classified low-grade tumors in 88% and high-grade tumors in 98.6%. Raman molecular imaging yields a 92% sensitivity and 91% specificity for detecting BCa. This study has very high accuracy in differentiating low-grade tumors from high-grade tumors. Low-grade tumors were precisely assigned in 74% of the cases and high-grade tumors in 98.5%.

Zong et al. (125) reported that telomeric elongation controlled SERS (TEC-SERS) could be useful in cancer diagnostic and therapeutic approaches. This approach involves binding of Raman reporter molecules and thiolated telomerase substrate primer to gold nanoparticles to construct a SERS tag. This active tag forms G-quadruplex structures in the presence of telomerase and elongation step stops in the absence of telomerase. TEC-SERS detection was applied on telomerase extract from cancer cell lines such as HeLa, SKBR3, and MCF7 and normal fibroblasts MRC-5. TEC-SERS has great reliability, simplicity, and sensitivity in detecting SERS substrates. This method can detect telomerase up to 3 orders of magnitude and avoid the high cost associated polymerase chain reaction procedures.

Bhattacharjee et al. (126, 127) reported that Swiss bare mice are the best option for transcutaneous breast cancer studies through Raman spectroscopy. Transcutaneous spectra of Swiss mice have shown not only the best signal-to-noise ratio but also closer similarities with ex vivo and in vivo human breast spectra. The spectral classification efficiency between normal breast and breast tumors was 99% and breast-to-bone metastasis can also be studied.

Sahu et al. (127) conducted a pilot study to explore Raman spectroscopic detection of serum specific markers in treated, mild, moderate, and advanced stages of asthma samples. Currently, the force expiratory volume in one-second value is considered a gold standard method for diagnosis and classification of different grades of asthma. Raman spectra were collected from serum samples on  $\text{CaF}_2$  windows using a 785-nm diode laser. Major spectral differences were reported between treated and different grades in the region of amide I, DNA, and  $\delta\text{-CH}_2$  deformation. Spectra of disease samples showed high amounts of proteins, plasma-free amino acids, and DNA. These peaks might indicate higher amounts of prostaglandins, leukotrienes, histamines, and glycosaminoglycans. These compounds play an important role in the inflammatory response and will appear in large amounts during an asthma attack. Chemometrics algorithms such as PCA, PC-LDA, and leave-one-out cross-validation were applied on spectral data to classify control and diseased serum samples. A multivariate approach has also classified different grades of asthma and treated versus untreated.

Fullwood et al. (128) reported the importance of substrate choice and sample preparation in spectroscopic studies to understand histopathology. This study has covered the effects of dewaxing procedure, spectral efficiency of different substrates such as low-E MirrIR slides, spectrosil quartz, and calcium fluoride ( $\text{CaF}_2$ ). Low-E glass slides showed the highest baseline and  $\text{CaF}_2$  had the lowest. Both  $\text{CaF}_2$  and spectrosil slides retained paraffin wax during the dewaxing procedure due to their surface roughness, whereas low-E slides did not. This study also found link between density of tissue type and dewaxing protocol. Dense cancerous tissue retained more wax compared to less dense normal tissue during the dewaxing protocol.

Mehrotra et al. (129) reported that SERS Raman spectroscopy could be used to explore DNA interactions with drugs in cancer therapeutic studies. Lomustine, an anticancer drug, is used to treat various types of cancers such as brain, small cell lung, and lymphomas. Calf thymus DNA was used to study conformational and structural interactions with the drug at physiological conditions. Major Raman peaks revealed stretching vibrations of nitrogenous bases, symmetric and asymmetric phosphate, and phosphate backbone. Raman spectra also revealed alkylation of major and minor grooves of double helical DNA, lomustine interacting sites on purines, pyrimidines, and sugar-phosphate backbone. This study showed that the SERS approach can be helpful in further understanding of DNA binding mechanisms in novel drug therapeutics.

### *The Characteristic Peak Frequencies*

It is believed that accurate peak definitions along with different multivariate approaches have a significant influence on the reliability of the results provided through different spectroscopic techniques. Most researchers rely on reported studies in the literature, which indicates that previously published work is very useful not only in understanding the chemical fingerprint of the biological molecules but also in distinguishing cancer from normal tissues. However, without a reliable and detailed database, which can cover most of the required peaks in the spectral range, it would be a time-consuming task to find the meanings of different unknown peak intensities. This updated article covers a wide range of supervised and unsupervised algorithms and how they have contributed toward diagnostic applications. In biological studies, for instance, where a wide range of chemical information related to functional groups can be attributed to every single peak, finding appropriate interpretations that can demonstrate the clinical importance of the technique and achieved results can be one of the most important steps in understanding spectroscopic research work. A wide range of the most frequently reported Raman peaks in biological tissues is presented in Table 1.

### **Summary**

Raman spectroscopy has become a powerful noninvasive tool to explore biochemical information of biological tissues, because each biological molecule possesses a unique pattern of vibration that can serve as a Raman marker. In recent years, Raman spectroscopy has been vividly used in cancer diagnostic studies and it has become a subject of great interest as an *in vivo* diagnostic tool to understand the chemical and morphological structure of tissue. The information presented in this work can result in significant savings, particularly in the time that scientists have to spend to define the peaks they find in their studies. We have tried to collect and present the data in such a way that can be referred to and used to make reliable definitions for spectral investigations.

The tabulated part, which is the main part of this article, provides the chemical fingerprint of each peak and its related study. It is suggested that, considering the type of samples being investigated and the chemical bands and functional groups that can possibly exist in the samples, the peak frequencies can be located in the table, and the appropriate interpretations could be chosen. Furthermore, having a detailed knowledge of the list of peaks that can be assigned to different biochemical compounds (such as lipids, proteins, or nucleic acids) would lead to a better correlation between the engineering and medical aspects of spectroscopy. The lipid content and the chemical structure of these compounds, for instance, can be evaluated using peaks frequencies of  $1754\text{ cm}^{-1}$  (C=O),  $1656\text{ cm}^{-1}$  (C=C),  $1440\text{ cm}^{-1}$  ( $\text{CH}_2$  bend), and  $1300\text{ cm}^{-1}$  ( $\text{CH}_2$  twist). Specification of the protein content of biological samples can also be understood from  $1656\text{ cm}^{-1}$  (amide I),  $1450\text{ cm}^{-1}$  ( $\text{CH}_2$  bend),  $1100\text{--}1375\text{ cm}^{-1}$  (amide III), and  $1004\text{ cm}^{-1}$  (phenylalanine) (70). Recent advances in Raman spectroscopy have revealed morphological changes associated with tissues such as nuclear enlargement, which became a Raman marker for cancer detection. On the other hand, Raman results have shown great correlation with pathological studies and have attracted attention from many clinical researchers to reduce the number of biopsies, patient trauma, and high medical costs. However, more articles and scientific backing can be collected to improve this work, to keep it updated, and to prepare a unique database that can be used for different methodologies. In addition, and along with the different research topics being covered by Raman spectroscopy, this article can be of crucial assistance for spectroscopists not only in the biological fields but also in areas related to materials and tissue engineering.

## References

1. Mahadevan-Jansen, A. and Richards-Kortum, R. (1997) Raman spectroscopy for cancer detection: A review. *International Conference of the IEEE Engineering in Medicine and Biology Society*, Chicago, IL, October 30–November 2.
2. Hanlon, E.B., Manoharan, R., Koo, T.W., Shafer, K.E., Motz, J.T., Fitzmaurice, M., Kramer, J.R., Itzkan, I., Dasari, R.R., and Feld, M.S. (2000) Prospects for in vivo Raman spectroscopy. *Phys. Med. Biol.*, 45 (2): R1–R59.
3. Dukor, R.K. (2002) Vibrational spectroscopy in the detection of cancer. *Biomedical Applications*, 5: 3335–3359.
4. Choo-Smith, L.P., Edwards, H.G.M., Endtz, H.P., Kros, J.M., Heule, F., Barr, H., Robinson, J.S., Bruining, H.A., and Puppels, G.J. (2002) Medical applications of Raman spectroscopy: From proof of principle to clinical implementation. *Biopolymers*, 67 (1): 1–9.
5. Swinson, B., Jerjes, W., El-Maaytah, M., Norris, P., and Hopper, C. (2006) Optical techniques in diagnosis of head and neck malignancy. *Oral Oncol.*, 42 (3): 221–228.
6. Shaw, R.A. and Mantsch, H.H. (1999) Vibrational biospectroscopy: From plants to animals to humans. A historical perspective. *J. Mol. Struct.*, 481: 1–13.
7. Petrich, W. (2006) Mid-infrared and Raman spectroscopy for medical diagnostics? *Shock*, 26.
8. Zeng, H., McWilliams, A., and Lam, S. (2004) Optical spectroscopy and imaging for early lung cancer detection: A review. *Photodiagnosis and Photodynamic Therapy*, 1 (2): 111–122.
9. Parker, M.F. (2005) Emerging technology in cervical cancer screening: Spectroscopy. *Clin. Obstet. Gynecol.*, 48 (1): 209–217.
10. Dekker, E. and Fockens, P. (2005) Advances in colonic imaging: New endoscopic imaging methods. *Eur. J. Gastroenterol. Hepatol.*, 17 (8): 209–217.
11. Demos, S.G., Vogel, A.J., and Gandjbakhche, A.H. (2006) Advances in optical spectroscopy and imaging of breast lesions. *J. Mammary Gland Biol. Neoplasia*, 11 (2): 165–181.

12. Pitt, G.D., Batchelder, D.N., Bennett, R., Bormett, R.W., Hayward, I.P., Smith, B.J.E., Williams, K.P.J., Yang, Y.Y., Baldwin, K.J., and Webster, S. (2005) Engineering aspects and applications of the new Raman instrumentation. *IEE Proc. Sci. Meas. Tech.*, 152 (6): 241–318.
13. Rehman, I.U., Movasaghi, Z., and Rehman, S. (2012) *Vibrational Spectroscopy for Tissue Analysis*. CRC Press: Boca Raton, FL.
14. Movasaghi, Z., Rehman, S., and Rehman, I.U. (2007) Raman spectroscopy of biological tissues. *Appl. Spectros. Rev.*, 42 (5).
15. Movasaghi, Z., Rehman, S., and Rehman, I.U. (2008) Fourier transform infrared (FTIR) spectroscopy of biological tissues. *Appl. Spectros. Rev.*, 43 (2): 134–179.
16. Short, M.A., Lui, H., McLean, D., Zeng, H., Alajlan, A., and Chen, X.K. (2006) Changes in nuclei and peritumoral collagen within nodular basal cell carcinomas via confocal micro-Raman spectroscopy. *J. Biomed. Optic.*, 11 (3): 34003–34013.
17. Sebag, J., Nie, S., Reiser, K., and Yu, N.T. (1993) Raman-spectroscopy characterization of diabetes effects on human vitreous in diabetic-retinopathy. *P. SPIE*, 1877: 284–288.
18. Singh, R. and Riess, F. (1998) C. V. Raman and the story of the Nobel Prize. *Curr. Sci.*, 75 (9): 965–971.
19. Conroy, J., Ryder, A.G., Leger, M.N., Hennessey, K., and Madden, M.G. (2005) Qualitative and quantitative analysis of chlorinated solvents using Raman spectroscopy and machine learning. *P. SPIE - The International Society for Optical Engineering*, 5826: 131–142.
20. Huang, Z.W., McWilliams, A., Lui, H., McLean, D.I., Lam, S., and Zeng, H.S. (2003) Near-infrared Raman spectroscopy for optical diagnosis of lung cancer. *Int. J. Canc.*, 107 (6): 1047–1052.
21. Shafer-Peltier, K.E., Haka, A.S., Fitzmaurice, M., Crowe, J., Myles, J., Dasari, R.R., and Feld, M.S. (2002) Raman microspectroscopic model of human breast tissue: Implications for breast cancer diagnosis in vivo. *J. Raman Spectros.*, 33 (7): 552–563.
22. Gazi, E., Dwyer, J., Gardner, P., Ghanbari-Siahkali, A., Wade, A.P., Miyan, J., Lockyer, N.P., Vickerman, J.C., Clarke, N.W., Shanks, J.H., Scott, L.J., Hart, C.A., and Brown, M. (2003) Applications of Fourier transform infrared microspectroscopy in studies of benign prostate and prostate cancer. A pilot study. *J. Pathol.*, 201 (1): 99–108.
23. Rehman, I., Smith, R., Hench, L.L., and Bonfield, W. (1995) Structural evaluation of human and sheep bone and comparison with synthetic hydroxyapatite by FT-Raman spectroscopy. *J. Biomed. Mater. Res.*, 29 (10): 1287–1294.
24. McManus, L.L., Bonnier, F., Burke, G.A., Meenan, B.J., Boyd, A.R., and Byrne, H.J. (2012) Assessment of an osteoblast-like cell line as a model for human primary osteoblasts using Raman spectroscopy. *Analyst*, 137 (7): 1559–1569.
25. Nyman, J.S., Makowski, A.J., Patil, C.A., Masui, T.P., O'Quinn, E.C., Bi, X., Guelcher, S.A., Nicollella, D.P., and Mahadevan-Jansen, A. (2011) Measuring differences in compositional properties of bone tissue by confocal Raman spectroscopy. *Calcif. Tissue Int.*, 89 (2): 111–122.
26. Kachi, S., Hirano, K., Takesue, Y., and Miura, M. (2000) Unusual corneal deposit after the topical use of cyclosporine as eyedrops. *Am. J. Ophthalmol.*, 130 (5): 667–669.
27. Utzinger, U., Heintzelman, D.L., Mahadevan-Jansen, A., Malpica, A., Follen, M., and Richards-Kortum, R. (2001) Near-infrared Raman spectroscopy for in vivo detection of cervical precancers. *Appl. Spectros.*, 55 (8): 955–959.
28. Kamemoto, L.E., Misra, A.K., Sharma, S.K., Goodman, M.T., Luk, H., Dykes, A.C., and Acosta, T. (2010) Near-infrared micro-Raman spectroscopy for in vitro detection of cervical cancer. *Appl. Spectros.*, 64 (3): 255–261.
29. Gonzalez-Solis, J.L., Rodriguez-Lopez, J., Martinez-Espinosa, J.C., Frausto-Reyes, C., Jaye-Suarez, L.F., Aguilar-Lemarroy, A.C., Vargas-Rodriguez, H., and Martinez-Cano, E. (2010) Detection of cervical cancer analyzing blood samples with Raman spectroscopy and multivariate analysis. *23rd International Congress on Laser Medicine/IALMS Courses/3rd Biannual Congress of the International Photo-Therapy Association*, Florence, Italy, November 6–7.

30. Stone, N., Kendall, C., Shepherd, N., Crow, P., and Barr, H. (2002) Near-infrared Raman spectroscopy for the classification of epithelial pre-cancers and cancers. *J. Raman Spectros.*, 33: 564–573.
31. Stone, N., Kendall, C., Smith, J., Crow, P., and Barr, H. (2004) Raman spectroscopy for identification of epithelial cancers. *Faraday Discuss.*, 126: 141–157.
32. Keller, M.D., Kanter, E.M., Lieber, C.A., Majumder, S.K., Hutchings, J., Ellis, D.L., Beaven, R.B., Stone, N., and Mahadevan-Jansen, A. (2008) Detecting temporal and spatial effects of epithelial cancers with Raman spectroscopy. *Dis. Markers*, 25 (6): 323–337.
33. Min, Y.K., Yamamoto, T., Kohda, E., Ito, T., and Hamaguchi, H. (2005) 1064 Nm near-infrared multichannel Raman spectroscopy of fresh human lung tissues. *J. Raman Spectros.*, 36: 73–76.
34. Kaminaka, S., Yamazaki, H., Ito, T., Kohda, E., and Hamaguchi, H.O. (2001) Near-infrared Raman spectroscopy of human lung tissues: Possibility of molecular-level cancer diagnosis. *J. Raman Spectros.*, 32: 139–141.
35. Huang, Z.W., McWilliams, A., Lam, S., English, J., McLean, D.I., Lui, H., and Zeng, H. (2003) Effect of formalin fixation on the near-infrared Raman spectroscopy of normal and cancerous human bronchial tissues. *Int. J. Oncol.*, 23: 649–655.
36. Oshima, Y., Shinzawa, H., Takenaka, T., Furihata, C., and Sato, H. (2010) Discrimination analysis of human lung cancer cells associated with histological type and malignancy using Raman spectroscopy. *J. Biomed. Optic.*, 15: 1.
37. Li, X., Yang, T., Li, S., and Yu, T. (2011) Surface-enhanced Raman spectroscopy differences of saliva between lung cancer patients and normal people. *Conference on Clinical and Biomedical Spectroscopy and Imaging II*, Munich, Germany, May 22.
38. Huang, N.Y., Short, M., Zhao, J.H., Wang, H.Q., Lui, H., Korbelik, M., and Zeng, H.S. (2011) Full range characterization of the Raman spectra of organs in a murine model. *Optic. Express*, 19 (23): 22892–22909.
39. Nawaz, H., Bonnier, F., Meade, A.D., Lyng, F.M., and Byrne, H.J. (2011) Comparison of subcellular responses for the evaluation and prediction of the chemotherapeutic response to cisplatin in lung adenocarcinoma using Raman spectroscopy. *Analyst*, 136 (12): 2450–2463.
40. Magee, N.D., Villaumie, J.S., Marple, E.T., Ennis, M., Elborn, J.S., and McGarvey, J.J. (2009) Ex vivo diagnosis of lung cancer using a Raman miniprobe. *J. Phys. Chem. B*, 113 (23): 8137–8141.
41. Redd, D.C.B., Feng, Z.C., Yue, K.T., and Gansler, T.S. (1993) Raman-spectroscopic characterization of human breast tissues—Implications for breast-cancer diagnosis. *Appl. Spectros.*, 47 (6).
42. Kline, N.J. and Treado, P.J. (1997) Raman chemical imaging of breast tissue. *J. Raman Spectros.*, 28: 2–3.
43. Tam, K., Armstrong, R.S., Carter, E.A., Lay, P.A., Mountford, C., Dowd, S., Himmerreich, U., and Russell, P. (2004) Raman spectroscopy for breast cancer detection: A sample processing study. *Proceedings of the XIX International Conference on Raman Spectroscopy*, Queensland, Australia, August 8–13.
44. Haka, A.S., Shafer-Peltier, K.E., Fitzmaurice, M., Crowe, J., Dasari, R.R., and Feld, M.S. (2005) Diagnosing breast cancer by using Raman spectroscopy. *Proc. Natl. Acad. Sci. Unit. States Am.*, 102 (35): 12371–12376.
45. Rehman, S., Movasaghi, Z., Tucker, A.T., Joel, S.P., Darr, J.A., Ruban, A.V., and Rehman, I.U. (2007) Raman spectroscopic analysis of breast cancer tissues: Identifying differences between normal, invasive ductal carcinoma and ductal carcinoma in situ of the breast tissue. *J. Raman Spectros.*, 38 (10): 1345–1351.
46. Haka, A.S., Volynskaya, Z., Gardecki, J.A., Nazemi, J., Shenk, R., Wang, N., Dasari, R.R., Fitzmaurice, M., and Feld, M.S. (2009) Diagnosing breast cancer using Raman spectroscopy: Prospective analysis. *J. Biomed. Optic.*, 14 (5).
47. Saha, A., Barman, I., Dingari, N.C., McGee, S., Volynskaya, Z., Galindo, L.H., Liu, W., Plecha, D., Klein, N., Dasari, R.R., and Fitzmaurice, M. (2011) Raman spectroscopy: A real-time

- tool for identifying microcalcifications during stereotactic breast core needle biopsies. *Biomed. Optic. Express*, 2 (10): 2792–2803.
48. Abramczyk, H., Brozek-Pluska, B., Surmacki, J., Jablonska, J., and Kordek, R. (2011) The label-free Raman imaging of human breast cancer. *J. Mol. Liq.*, 164 (1–2): 123–131.
  49. Abramczyk, H., Brozek-Pluska, B., Surmacki, J., Jablonska-Gajewicz, J., and Kordek, R. (2012) Raman “optical biopsy” of human breast cancer. *Progr. Biophys. Mol. Biol.*, 108 (1–2): 74–81.
  50. Cheng, W.T., Liu, M.T., Liu, H.N., and Lin, S.Y. (2005) Micro-Raman spectroscopy used to identify and grade human skin pilomatrixoma. *Microsc. Res. Tech.*, 68: 75–79.
  51. Kaminaka, S., Ito, T., Yamazaki, H., Kohda, E., and Hamaguchi, H. (2002) Near-infrared multichannel Raman spectroscopy toward real-time in vivo cancer diagnosis. *J. Raman Spectros.*, 33: 498–502.
  52. Sigurdsson, S., Philipsen, P.A., Hansen, L.K., Larsen, J., Gniadecka, M., and Wulf, H.C. (2004) Detection of skin cancer by classification of Raman spectra. *IEEE Trans. Biomed. Eng.*, 51: 10.
  53. Gniadecka, M., Wulf, H.C., Mortensen, N.N., Nielsen, O.F., and Christensen, D.H. (1997) Diagnosis of basal cell carcinoma by Raman spectroscopy. *J. Raman Spectros.*, 28: 125–129.
  54. Barry, B.W., Edwards, H.G.M., and Williams, A.C. (1992) Fourier-transform Raman and infrared vibrational study of human skin—Assignment of spectral bands. *J. Raman Spectros.*, 23 (11).
  55. Caspers, P.J., Lucassen, G.W., Carter, E.A., Bruining, H.A., and Puppels, G.J. (2001) In vivo confocal Raman microspectroscopy of the skin: Noninvasive determination of molecular concentration profiles. *J. Invest. Dermatol.*, 116 (3): 434–442.
  56. Larraona-Puy, M., Ghita, A., Zoladek, A., Perkins, W., Varma, S., Leach, I.H., Koloydenko, A.A., Williams, H., and Notingher, I. (2009) Development of Raman microspectroscopy for automated detection and imaging of basal cell carcinoma. *J. Biomed. Optic.*, 14: 5.
  57. Cartaxo, S.B., de Abranches Oliveira Santos, I.D., Bitar, R., Oliveira, A.F., Ferreira, L.M., Martinho, H.S., and Martin, A.A. (2010) FT-Raman spectroscopy for the differentiation between cutaneous melanoma and pigmented nevus. *Acta Cirurgica Brasileira*, 25 (4): 351–356.
  58. Larraona-Puy, M., Ghita, A., Zoladek, A., Perkins, W., Varma, S., Leach, I.H., Koloydenko, A.A., Williams, H., and Notingher, I. (2011) Discrimination between basal cell carcinoma and hair follicles in skin tissue sections by Raman micro-spectroscopy. *J. Mol. Struct.*, 993 (1–3): 57–61.
  59. Wang, H., Huang, N., Zhao, J., Lui, H., Korbelik, M., and Zeng, H. (2011) Depth-resolved in vivo micro-Raman spectroscopy of a murine skin tumor model reveals cancer-specific spectral biomarkers. *J. Raman Spectros.*, 42 (2): 160–166.
  60. König, K., Breunig, H.G., Buckle, R., Kellner-Hofer, M., Weinigel, M., Buttner, E., Sterry, W., and Lademann, J. (2011) Optical skin biopsies by clinical cars and multiphoton fluorescence/SHG tomography. *Laser Phys. Lett.*, 8 (6): 465–468.
  61. de Oliveira, A.F., Santos, I., Cartaxo, S.B., Bitar, R.A., Enokihara, M., Martinho, H.D., Martin, A.A., and Ferreira, L.M. (2010) Differential diagnosis in primary and metastatic cutaneous melanoma by FT-Raman spectroscopy. *Acta Cirurgica Brasileira*, 25 (5): 434–439.
  62. Tan, Y.Y., Shen, A.G., Zhang, J.W., Wu, N., Feng, L., Wu, Q.F., Ye, Y., and Hu, J.M. (2003) Design of auto-classifying system and its application in Raman spectroscopy diagnosis of gastric carcinoma. *2003 International Conference on Machine Learning and Cybernetics*, China, November 2–5.
  63. Weng, S.F., Ling, X.F., Song, Y.Y., Xu, Y.Z., Li, W.H., Zhang, X., Yang, L., Sun, W., Zhou, X., and Wu, J. (2000) FTIR fiber optics and FT-Raman spectroscopic studies for the diagnosis of cancer. *Am. Clin. Lab.*, 19 (7): 20.
  64. Shetty, G., Kendall, C., Shepherd, N., Stone, N., and Barr, H. (2006) Raman spectroscopy: Elucidation of biochemical changes in carcinogenesis of oesophagus. *Br. J. Canc.*, 94: 1460–1464.
  65. Feng, S., Pan, J., Wu, Y., Lin, D., Chen, Y., Xi, G., Lin, J., and Chen, R. (2011) Study on gastric cancer blood plasma based on surface-enhanced Raman spectroscopy combined with multivariate analysis. *Sci. China C Life Sci.*, 54 (9): 828–834.

66. Kawabata, T., Kikuchi, H., Okazaki, S., Yamamoto, M., Hiramatsu, Y., Yang, J., Baba, M., Ohta, M., Kamiya, K., Tanaka, T., and Konno, H. (2011) Near-infrared multichannel Raman spectroscopy with a 1064 nm excitation wavelength for ex vivo diagnosis of gastric cancer. *J. Surg. Res.*, 169 (2): E137–E143.
67. Su, L., Sun, Y.F., Chen, Y., Chen, P., Shen, A.G., Wang, X.H., Jia, J., Zhao, Y.F., Zhou, X.D., and Hu, J.M. (2012) Raman spectral properties of squamous cell carcinoma of oral tissues and cells. *Laser Phys.*, 22 (1): 311–316.
68. Shim, M.G., Song, L., Marcon, N.E., and Wilson, B.C. (2000) In vivo near-infrared Raman spectroscopy: Demonstration of feasibility during clinical gastrointestinal endoscopy. *Photochem. Photobiol.*, 72 (1): 146–150.
69. Kendall, C., Day, J., Hutchings, J., Smith, B., Shepherd, N., Barr, H., and Stone, N. (2010) Evaluation of Raman probe for oesophageal cancer diagnostics. *Analyst*, 135 (12): 3038–3041.
70. Lakshmi, R.J., Kartha, V.B., Krishna, C.M., Solomon, J.G.R., Ullas, G., and Devi, P.U. (2002) Tissue Raman spectroscopy for the study of radiation damage: Brain irradiation of mice. *Radiat. Res.*, 157 (2): 175–182.
71. Krafft, C., Neudert, L., Simat, T., and Salzer, R. (2005) Near infrared Raman spectra of human brain lipids. *Spectrochim. Acta Mol. Biomol. Spectros.*, 61: 1529–1535.
72. Sato, H., Yamamoto, Y.S., Maruyama, A., Katagiri, T., Matsuura, Y., and Ozaki, Y. (2009) Raman study of brain functions in live mice and rats: A pilot study. *Vib. Spectros.*, 50 (1): 125–130.
73. Kohler, M., Machill, S., Salzer, R., and Krafft, C. (2009) Characterization of lipid extracts from brain tissue and tumors using Raman spectroscopy and mass spectrometry. *Anal. Bioanal. Chem.*, 393 (5): 1513–1520.
74. Kirsch, M., Schackert, G., Salzer, R., and Krafft, C. (2010) Raman spectroscopic imaging for in vivo detection of cerebral brain metastases. *Anal. Bioanal. Chem.*, 398 (4): 1707–1713.
75. Tay, L.-L., Tremblay, R.G., Hulse, J., Zurakowski, B., Thompson, M., and Bani-Yaghoub, M. (2011) Detection of acute brain injury by Raman spectral signature. *Analyst*, 136 (8): 1620–1626.
76. Malini, R., Venkatakrishna, K., Kurien, J., Pai, K.M., Rao, L., Kartha, V.B., and Krishna, C.M. (2006) Discrimination of normal, inflammatory, premalignant, and malignant oral tissue: A Raman spectroscopy study. *Biopolymers*, 81 (3): 179–193.
77. Wu, J.G., Xu, Y.Z., Sun, C.W., Soloway, R.D., Xu, D.F., Wu, Q.G., Sun, K.H., Weng, S.F., and Xu, G.X. (2001) Distinguishing malignant from normal oral tissues using FTIR fiber-optic techniques. *Biopolymers*, 62: 185–192.
78. Lau, D.P., Huang, Z.W., Lui, H., Anderson, D.W., Berean, K., Morrison, M.D., Shen, L., and Zeng, H.S. (2005) Raman spectroscopy for optical diagnosis in the larynx: Preliminary findings. *Laser. Surg. Med.*, 32: 210–214.
79. Li, Y., Wen, Z.-N., Li, L.-J., Li, M.-L., Gao, N., and Guo, Y.-Z. (2010) Research on the Raman spectral character and diagnostic value of squamous cell carcinoma of oral mucosa. *J. Raman Spectros.*, 41 (2): 142–147.
80. Bergholt, M.S., Zheng, W., Lin, K., Ho, K.Y., Teh, M., Yeoh, K.G., So, J.B.Y., and Huang, Z. (2011) Characterizing variability in in vivo Raman spectra of different anatomical locations in the upper gastrointestinal tract toward cancer detection. *J. Biomed. Optic.*, 16 (3): 037003.
81. Lau, D.P., Huang, Z.W., Lui, H., Man, C.S., Berean, K., Morrison, M.D., and Zeng, H.S. (2003) Raman spectroscopy for optical diagnosis in normal and cancerous tissue of the nasopharynx—Preliminary findings. *Laser. Surg. Med.*, 32: 210–214.
82. Lo, W.-L., Lai, J.-Y., Feinberg, S.E., Izumi, K., Kao, S.-Y., Chang, C.-S., Lin, A., and Chiang, H.K. (2011) Raman spectroscopy monitoring of the cellular activities of a tissue-engineered ex vivo produced oral mucosal equivalent. *J. Raman Spectros.*, 42 (2): 174–178.
83. Li, X., Lin, J., Ding, J., Wang, S., Liu, Q., and Qing, S. (2004) Raman spectroscopy and fluorescence for the detection of liver cancer and abnormal liver tissue. *Annual International Conference of the IEEE Engineering in Medicine and Biology Society*, San Francisco, CA, September 1–5.

84. Guo, J., Du, B., Qian, M., Cai, W., Wang, Z., and Sun, Z. (2009) Raman spectroscopic identification of normal and malignant hepatocytes. *Chin. Optic. Lett.*, 7 (1): 60–63.
85. Schie, I.W., Wu, J., Weeks, T., Zern, M.A., Rutledge, J.C., and Huser, T. (2011) Label-free imaging and analysis of the effects of lipolysis products on primary hepatocytes. *J. Biophoton.*, 4 (6): 425–434.
86. Movasaghi, Z., Rehman, S., and Rehman, I.U. (2012) Raman spectroscopy can detect and monitor cancer at cellular level: Analysis of resistant and sensitive subtypes of testicular cancer cell lines. *Appl. Spectros. Rev.*, 47 (7).
87. Chiang, H.P., Song, R., Mou, B., Li, K.P., Chiang, P., Wang, D., Tse, W.S., and Ho, L.T. (1999) Fourier transform Raman spectroscopy of carcinogenic polycyclic aromatic hydrocarbons in biological systems: Binding to heme proteins. *J. Raman Spectros.*, 30: 551–555.
88. van de Poll, S.W.E., Romer, T.J., Volger, O.L., Delsing, D.J.M., Schut, T.C.B., Princen, H.M.G., Havekes, L.M., Jukema, J.W., van der Laarse, A., and Puppels, G.J. (2001) Raman spectroscopic evaluation of the effects of diet and lipid-lowering therapy on atherosclerotic plaque development in mice. *Arterioscler. Thromb. Vasc. Biol.*, 21: 1630–1635.
89. Duarte, J., Pacheco, M.T.T., Machado, R.Z., Silveira, L., Zangaro, R.A., and Villaverde, A.B. (2002) Use of near-infrared Raman spectroscopy to detect IgG and IgM antibodies against *Toxoplasma gondii* in serum samples of domestic cats. *Cell. Mol. Biol.*, 48 (5): 585–589.
90. Li, X.Z. and Jin, H.Q. (2001) Raman spectroscopy of serum for cancer detection. *23rd Annual International Conference of the IEEE Engineering in Medicine and Biology Society*, Istanbul, Turkey, October 25–28.
91. Rohleder, D., Kiefer, W., and Petrich, W. (2004) Quantitative analysis of serum and serum ultrafiltrate by means of Raman spectroscopy. *Analyst*, 129: 906–911.
92. Neugebauer, U., Clement, J.H., Bocklitz, T., Krafft, C., and Popp, J. (2010) Identification and differentiation of single cells from peripheral blood by Raman spectroscopic imaging. *J. Biophoton.*, 3 (8–9): 579–587.
93. Neugebauer, U., Bocklitz, T., Clement, J.H., Krafft, C., and Popp, J. (2010) Towards detection and identification of circulating tumour cells using Raman spectroscopy. *Analyst*, 135 (12): 3178–3182.
94. Silveira, L., Sathaiah, S., Zangaro, R.A., Pacheco, M.T.T., Chavantes, M.C., and Pasqualucci, C.A.G. (2002) Correlation between near-infrared Raman spectroscopy and the histopathological analysis of atherosclerosis in human coronary arteries. *Laser. Surg. Med.*, 30: 290–297.
95. Puppels, G.J., Garritsen, H.S.P., Kummer, J.A., and Greve, J. (1993) Carotenoids located in human lymphocyte subpopulations and natural-killer-cells by Raman microspectroscopy. *Cytometry*, 14: 251–256.
96. Dochow, S., Krafft, C., Neugebauer, U., Bocklitz, T., Henkel, T., Mayer, G., Albert, J., and Popp, J. (2011) Tumour cell identification by means of Raman spectroscopy in combination with optical traps and microfluidic environments. *Lab on a Chip*, 11 (8): 1484–1490.
97. Lin, D., Lin, J., Wu, Y., Feng, S., Li, Y., Yu, Y., Xi, G., Zeng, H., and Chen, R. (2011) Investigation on the interactions of lymphoma cells with paclitaxel by Raman spectroscopy. *Spectroscopy*, 25 (1): 23–32.
98. Deng, J.L., Wei, Q., Zhang, M.H., Wang, Y.Z., and Li, Y.Q. (2005) Study of the effect of alcohol on single human red blood cells using near-infrared laser tweezers Raman spectroscopy. *J. Raman Spectros.*, 36: 257–261.
99. Liu, F.-T., Agrawal, S.G., Movasaghi, Z., Wyatt, P.B., Rehman, I.U., Gribben, J.G., Newland, A.C., and Jia, L. (2008) Dietary flavonoids inhibit the anticancer effects of the proteasome inhibitor bortezomib. *Blood*, 112: 9.
100. Krishna, C.M., Sockalingum, G.D., Kegelaer, G., Rubin, S., Kartha, V.B., and Manfait, M. (2005) Micro-Raman spectroscopy of mixed cancer cell populations. *Vib. Spectros.*, 38: 95–100.
101. Kuhnert, N. and Thumser, A. (2004) An investigation into the use of Raman microscopy for the detection of labelled compounds in living human cells. *J. Labelled Comp. Rad.*, 47: 493–500.
102. Naumann, D. (1998) Infrared and NIR Raman spectroscopy in medical microbiology. *Conference on Infrared Spectroscopy—New Tool in Medicine*, San Jose, CA, April 24.

103. Chan, J.W., Taylor, D.S., Zwerdling, T., Lane, S.M., Ihara, K., and Huser, T. (2006) Micro-Raman spectroscopy detects individual neoplastic and normal hematopoietic cells. *Biophys. J.*, 90: 648–656.
104. Farquharson, S., Shende, C., Inscore, F.E., Maksymiuk, P., and Gift, A. (2005) Analysis of 5-fluorouracil in saliva using surface-enhanced Raman spectroscopy. *J. Raman Spectros.*, 36: 208–212.
105. Barhoumi, A. and Halas, N.J. (2011) Detecting chemically modified DNA bases using surface-enhanced Raman spectroscopy. *J. Phys. Chem. Lett.*, 2 (24): 3118–3123.
106. Ruiz-Chica, A.J., Medina, M.A., Sanchez-Jimenez, F., and Ramirez, F.J. (2004) Characterization by Raman spectroscopy of conformational changes on guanine–cytosine and adenine–thymine oligonucleotides induced by aminooxy analogues of spermidine. *J. Raman Spectros.*, 35: 93–100.
107. Jalkanen, K.J., Jurgensen, V.W., Claussen, A., Rahim, A., Jensen, G.M., Wade, R.C., Nardi, F., Jung, C., Degtyarenko, I.M., Nieminen, R.M., Herrmann, F., Knapp-Mohammady, M., Niehaus, T.A., Frimand, K., and Suhai, S. (2006) Use of vibrational spectroscopy to study protein and DNA structure, hydration, and binding of biomolecules: A combined theoretical and experimental approach. *Int. J. Quant. Chem.*, 106: 1160–1198.
108. Zhang, X., Roeyfaers, M.B.J., Basu, S., Daniele, J.R., Fu, D., Freudiger, C.W., Holtom, G.R., and Xie, X.S. (2012) Label-free live-cell imaging of nucleic acids using stimulated Raman scattering microscopy. *ChemPhysChem*, 13 (4): 1054–1059.
109. Vo-Dinh, T., Allain, L.R., and Stokes, D.L. (2002) Cancer gene detection using surface-enhanced Raman scattering (SERS). *J. Raman Spectros.*, 33: 511–516.
110. Binoy, J., Abraham, J.P., Joe, I.H., Jayakumar, V.S., Pettit, G.R., and Nielsen, O.F. (2004) NIR-FT Raman and FT-IR spectral studies and ab initio calculations of the anti-cancer drug combretastatin-A4. *J. Raman Spectros.*, 35: 939–946.
111. O Faolain, E., Hunter, M.B., Byrne, J.M., Kelehan, P., McNamara, M., Byrne, H.J., and Lyng, F.M. (2005) A study examining the effects of tissue processing on human tissue sections using vibrational spectroscopy. *Vib. Spectros.*, 38: 121–127.
112. Viehoveer, A.R., Anderson, D., Jansen, D., and Mahadevan-Jansen, A. (2003) Organotypic raft cultures as an effective in vitro tool for understanding Raman spectral analysis of tissue. *Photochem. Photobiol.*, 78: 517–524.
113. Koljenovic, S., Schut, T.B., Vincent, A., Kros, J.M., and Puppels, G.J. (2005) Detection of meningioma in dura mater by Raman spectroscopy. *Anal. Chem.*, 77 (24): 7958–7965.
114. Lieber, C.A., Nethercott, H.E., and Kabeer, M.H. (2010) Cancer field effects in normal tissues revealed by Raman spectroscopy. *Biomed. Optic. Express*, 1 (3): 975–982.
115. Silva, M.A.S.R., Lopes, R.M., Aimbire, F., Leite, K.R.M., Pasqualucci, C.A., Pacheco, M.T.T., and Silveira, L., Jr. (2010) Diagnostic model for differentiating human malignant prostate lesion from normal tissue in vitro by Raman spectroscopy. *22nd International Conference on Raman Spectroscopy*, Boston, MA, August 8–13.
116. Rabah, R., Weber, R., Serhatkulu, G.K., Cao, A., Dai, H., Pandya, A., Naik, R., Auner, G., Poulik, J., and Klein, M. (2008) Diagnosis of neuroblastoma and ganglioneuroma using Raman spectroscopy. *J. Pediatr. Surg.*, 43 (1): 171–176.
117. Kim, J.H., Kim, J.S., Choi, H., Lee, S.M., Jim, B.H., Yu, K.N., Kuk, E., Kim, Y.K., Jeong, D.H., Cho, M.H., and Lee, Y.S. (2006) Nanoparticle probes with surface enhanced Raman spectroscopic tags (SERS dots) for cellular cancer targeting. *Nanomedicine: Nanotechnology Biology and Medicine*, 78 (19): 6967–6973.
118. Short, K.W., Carpenter, S., Freyer, J.P., and Mourant, J.R. (2005) Raman spectroscopy detects biochemical changes due to proliferation in mammalian cell cultures. *Biophys. J.*, 88: 4274–4288.
119. Chen, B., Li, S., Li, J., Guo, Z., Chen, Q., and Mai, H. (2013) Optimal multivariate method for Raman spectroscopy based diagnosis of nasopharyngeal carcinoma. *J. Appl. Phys.*, 114: 24.

120. Lloyd, G.R., Almond, L.M., Stone, N., Shepherd, N., Sanders, S., Hutchings, J., Barr, H., and Kendall, C. (2014) Utilising non-consensus pathology measurements to improve the diagnosis of oesophageal cancer using a Raman spectroscopic probe. *Analyst*, 139 (2): 381–388.
121. Almond, L.M., Hutchings, J., Lloyd, G., Barr, H., Shepherd, N., Day, J., Stevens, O., Sanders, S., Wadley, M., Stone, N., and Kendall, C. (2014) Endoscopic Raman spectroscopy enables objective diagnosis of dysplasia in Barrett's esophagus. *Gastrointest. Endosc.*, 79 (1): 37–45.
122. Liu, Z., Davis, C., Cai, W., He, L., Chen, X., and Dai, H. (2008) Circulation and long-term fate of functionalized, biocompatible single-walled carbon nanotubes in mice probed by Raman spectroscopy. *Proc. Natl. Acad. Sci. Unit. States Am.*, 105 (5): 1410–1415.
123. Bonnier, F. and Byrne, H.J. (2012) Understanding the molecular information contained in principal component analysis of vibrational spectra of biological systems. *Analyst*, 137: 2.
124. Shapiro, A., Gofrit, O.N., Pizov, G., Cohen, J.K., and Maier, J. (2011) Raman molecular imaging: A novel spectroscopic technique for diagnosis of bladder cancer in urine specimens. *Eur. Urol.*, 59 (1): 106–112.
125. Zong, S., Wang, Z., Chen, H., and Cui, Y. (2013) Ultrasensitive telomerase activity detection by telomeric elongation controlled surface enhanced Raman scattering. *Small*, 9 (24): 4215–4220.
126. Bhattacharjee, T., Kumar, P., Maru, G., Ingle, A., and Krishna, C.M. (2014) Swiss bare mice: A suitable model for transcutaneous in vivo Raman spectroscopic studies of breast cancer. *Laser. Med. Sci.*, 29 (1): 325–333.
127. Sahu, A., Dalal, K., Naglot, S., Aggarwal, P., and Krishna, C.M. (2013) Serum based diagnosis of asthma using Raman spectroscopy: An early phase pilot study. *PLoS One*, 8: 11.
128. Fullwood, L.M., Griffiths, D., Ashton, K., Dawson, T., Lea, R.W., Davis, C., Bonnier, F., Byrne, H.J., and Baker, M.J. (2014) Effect of substrate choice and tissue type on tissue preparation for spectral histopathology by Raman microspectroscopy. *Analyst*, 139 (2): 446–454.
129. Mehrotra, R., Jangir, D.K., Agarwal, S., Ray, B., Singh, P., and Srivastava, A.K. (2013) Interaction studies of anticancer drug lomustine with calf thymus DNA using surface enhanced Raman spectroscopy. *MAPAN-Journal of Metrology Society of India*, 28 (4): 273–277.
130. Schulz, H. and Baranska, M. (2007) Identification and quantification of valuable plant substances by IR and Raman spectroscopy. *Vib. Spectros.*, 43: 13–25.
131. Notingher, I., Green, C., Dyer, C., Perkins, E., Hopkins, N., Lindsay, C., and Hench, L.L. (2004) Discrimination between ricin and sulphur mustard toxicity in vitro using Raman spectroscopy. *J. R. Soc. Interface*, 1: 79–90.
132. Frank, C.J., McCreery, R.L., and Redd, D.C.B. (1995) Raman-spectroscopy of normal and diseased human breast tissues. *Anal. Chem.*, 67 (5): 777–783.
133. Laska, J. and Widlarz, J. (2005) Spectroscopic and structural characterization of low molecular weight fractions of polyaniline. *Polymer*, 46: 1485–1495.
134. Katainen, E., Elomaa, M., Laakkonen, U.-M., Sippola, E., Niemela, P., Suhonen, J., and Jarvinen, K. (2007) Quantification of the amphetamine content in seized street samples by Raman spectroscopy. *J. Forensic Sci.*, 52 (1): 88–92.
135. Huang, Z.W., Lui, H., McLean, D.I., Korbek, M., and Zeng, H.S. (2005) Raman spectroscopy in combination with background near-infrared autofluorescence enhances the in vivo assessment of malignant tissues. *Photochem. Photobiol.*, 81: 1219–1226.
136. Seballos, L., Zhang, J.Z., and Sutphen, R. (2005) Surface-enhanced Raman scattering detection of lysophosphatidic acid. *Anal. Bioanal. Chem.*, 383: 763–767.
137. Dovbeshko, G.I., Gridina, N.Y., Kruglova, E.B., and Pashchuk, O.P. (2000) FTIR spectroscopy studies of nucleic acid damage. *Talanta*, 53: 233–246.
138. Andrus, P.G.L. and Strickland, R.D. (1998) Cancer grading by Fourier transform infrared spectroscopy. *Biospectroscopy*, 4: 37–46.
139. Mordechai, S., Sahu, R.K., Hammody, Z., Mark, S., Kantarovich, K., Guterman, H., Podshyvalov, A., Goldstein, J., and Argov, S. (2004) Possible common biomarkers from FTIR microspectroscopy of cervical cancer and melanoma. *J. Microsc.*, 215: 86–91.

140. Chiriboga, L., Xie, P., Yee, H., Vigorita, V., Zarou, D., Zakim, D., and Diem, M. (1998) Infrared spectroscopy of human tissue. I. Differentiation and maturation of epithelial cells in the human cervix. *Biospectroscopy*, 4: 47–53.
141. Ronen, S.M., Stier, A., and Degani, H. (1990) NMR-studies of the lipid-metabolism of T47d human breast-cancer spheroids. *FEBS Lett.*, 266: 147–149.
142. Wood, B.R., Quinn, M.A., Tait, B., Ashdown, M., Hislop, T., Romeo, M., and McNaughton, D. (1998) FTIR microspectroscopic study of cell types and potential confounding variables in screening for cervical malignancies. *Biospectroscopy*, 4: 75–91.
143. Kachrimanis, K., Braun, D.E., and Griesser, U.J. (2007) Quantitative analysis of paracetamol polymorphs in powder mixtures by FT-Raman spectroscopy and PLS regression. *J. Pharmaceut. Biomed. Anal.*, 43: 407–412.
144. Singh, A., Ghosh, A., Roy, A., and Ray, N.R. (2006) Quantitative analysis of hydrogenated diamondlike carbon films by visible Raman spectroscopy. *J. Appl. Phys.*, 100: 1–8.
145. Fung, M.F.K., Senterman, M.K., Mikhael, N.Z., Lacelle, S., and Wong, P.T.T. (1996) Pressure-tuning Fourier transform infrared spectroscopic study of carcinogenesis in human endometrium. *Biospectroscopy*, 2: 155–165.
146. Barr, H., Dix, T., and Stone, N. (1998) Optical spectroscopy for the early diagnosis of gastrointestinal malignancy. *Laser Med. Sci.*, 13: 3–13.
147. Lucassen, G.W., van Veen, G.N., and Jansen, J.A. (1998) Band analysis of hydrated human skin stratum corneum attenuated total reflectance Fourier transform infrared spectra in vivo. *J. Biomed. Optic.*, 3: 267–280.
148. Mazurek, S. and Szostak, R. (2006) Quantitative determination of captopril and prednisolone in tablets by FT-Raman spectroscopy. *J. Pharmaceut. Biomed. Anal.*, 40: 1225–1230.
149. Quintas, G., Garrigues, S., Pastor, A., and de la Guardia, M. (2004) FT-Raman determination of mepiquat chloride in agrochemical products. *Vib. Spectros.*, 36: 41–46.
150. Agarwal, R., Tandon, P., and Gupta, V.D. (2006) Phonon dispersion in poly(dimethylsilane). *J. Organomet. Chem.*, 691: 2902–2908.
151. Ortiz, C., Zhang, D.M., Xie, Y., Ribbe, A.E., and Ben-Amotz, D. (2006) Validation of the drop coating deposition Raman method for protein analysis. *Anal. Biochem.*, 353: 157–166.
152. Behrens, H., Roux, J., Neuville, D.R., and Siemann, M. (2006) Quantification of dissolved H<sub>2</sub>O in silicate glasses using confocal micro-Raman spectroscopy. *Chem. Geol.*, 229: 96–112.